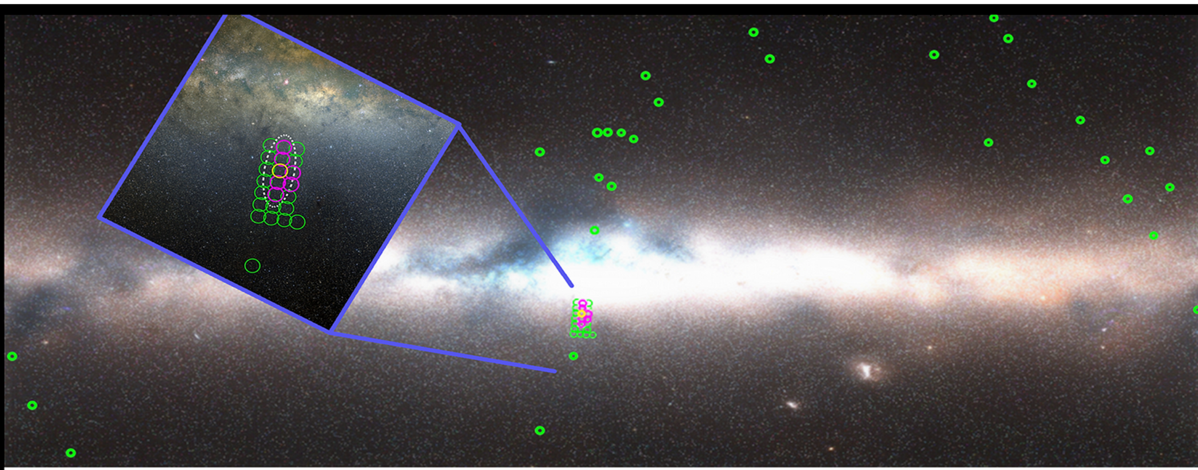

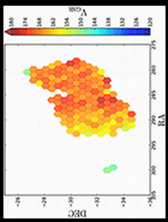

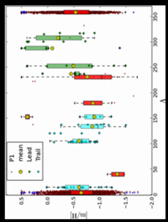

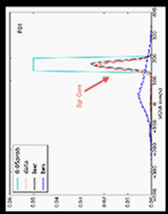

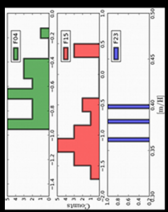

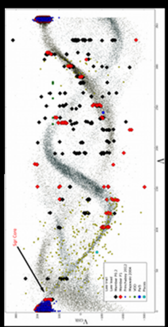

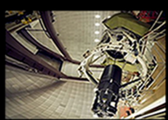

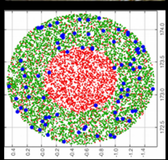

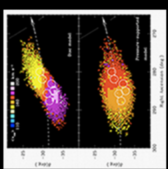

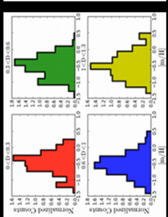

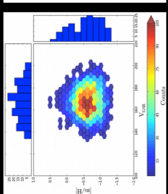

Selecting Sagittarius: A Study in Kinematics and Metallicities

By

Elaina A. Hyde

A thesis submitted to Macquarie University

for the degree of

Doctor of Philosophy

Department of Physics and Astronomy

July 2014

MACQUARIE UNIVERSITY

FACULTY OF SCIENCE

Typeset in $\LaTeX\,2_{\varepsilon}$.

Except where acknowledged in the customary manner, the material presented in this thesis is, to the best of my knowledge, original and has not been submitted in whole or part for a degree in any university.

Elaina A. Hyde

Acknowledgements

I would like to thank Dennis van Welie for extended conversations about logic, statistics, and general physics. For playing math games and for listening to all of my plans for a base on Mars, even though you have heard them before. To all of my family, thank you for understanding when I ran away to do science!

This project has spanned 3.5 years, at least three continents, and many different universities. Of the numerous people working in various areas of Galactic Archaeology I will here attempt to name a few of the people who were most influential to me and to my work on this thesis. It has been an amazing journey, using the tools of spectroscopy, investigating Sagittarius dwarf stars as they peek out from their hidden positions around our Milky Way.

I would like to thank Andreas Koch and my colleagues at Macquarie for many discussions about template fitting, the calcium triplet and all sorts of coding discussions. Additionally I would like thank Rob Sharp (who has since moved on from the AAO) and everyone else at the AAO who answered my questions about *2dfdr*, fortran and helped me get started during my first year of research.

For her general science discussions and amazing insights on telescope proposal strategies, I would like to thank Sarah Martell. Sarah, it has been really wonderful working with you, and I look forward to attending more GALAH meetings, and helping with the observing of course! Of course science discussions being a main part of this work, I also must give thanks to Vasily Belokurov and Sergey Koposov for recommending the Orphan Stream as a field of interest, and of course, for helping to set up the observation of our field.

Thanks to Rodrigo Ibata and Arnaud Siebert for contributing the Sgr stream data and running the modified RAVE pipeline, allowing me to form one giant dataset covering both the stream and core. Thank you to all of my colleagues who showed me such great hospitality on my trips to your institutes (Zeljko Ivezic, Mike Irwin, Rodrigo Ibata, and everyone else!). Our research discussions were some of the most productive I've had. I would like to thank you not only for inviting me over, but also for showing me around and making me feel so welcome.

Thanks to Stefan Keller for encouraging me to pursue the core region, assistance in developing the selection technique, and letting me come and hide out in the Mt Stromlo lodge in Canberra to figure out the fiddly programming bits. It was wonderful to work on the AEGIS project with you, and I especially enjoyed the extra observing trip at the AAT. Our science conversations have been a highlight of my research project and your approach to the research process has been an inspiration to me personally and professionally.

Finally thanks to my primary supervisor Daniel Zucker who made all this possible. For convincing me to move to Australia, for introducing me to the world of Galactic Archaeology and the Sagittarius dwarf, for all of the fun memories I have from this project, and for the breakthroughs and all the nice people I have met working in this area. I have learned a lot and enjoyed attending the meetings for the GALAH/HERMES group. I would also like to thank you for your work in writing the observing proposals which allowed me to spend several wonderful weeks obtaining this beautiful data set, and most of all, thank you for believing me when I said that I thought I could do something with it. This has been a intriguing and challenging project, but, well worth the time spent and I look forward to our future collaborations.

To all of my colleagues, friends, and family who have seen this project expand from a small six field observational analysis to an investigation wrapping around our Galaxy, thank you.

- Elaina Ann Hyde, PhD

List of Publications

Some of the work presented in this thesis was also presented during the course of the project in other forms. This includes scientific talks, peer-reviewed papers, and scientific conference posters as listed below:

Publications

- Peñarrubia, J., Zucker, D. B., Irwin, M. J., Hyde, E. A., Lane, R. R., Lewis, G. F., Gilmore, G., Wyn Evans, N., and Belokurov, V. *No Evidence for Internal Rotation in the Remnant Core of the Sagittarius Dwarf.* ApJ **727**, L2 (2011)
  −This was the paper that began my research program; the results are discussed in Chapters 2, 3 and 6. I performed 100% of the data reduction and roughly 80% of the data processing for this paper.

- Hyde, E. A., Zucker, D. B., Irwin, M., Peñarrubia, J., and Koch, A. *Hermes and the Sagittarius Dwarf: A Low Metallicity Goldmine?* Astronomical Society of the Pacific Conference Series **458**, 325 (2012)
  − These conference proceedings combined my Sagittarius dwarf core data with the stream observations of Rodrigo Ibata to explore the possibility of low metallicity objects in our data, which is discussed in Chapter 6.

Posters and Official Presentations

- Hyde, E. A., Zucker, D. B., Penarrubia, J., Irwin, M., Lane, R., Lewis, G. F., Gilmore, G., and Koch, A. *Was the Progenitor of the Sagittarius Stream a Disc Galaxy? Recent Results and Observations.* American Astronomical Society Meeting Abstracts #217 **43**, 152.28 (2011)
  − This poster illustrated the reduction and processing of the data that I performed for the 2011 Penarrubia et al. paper. It presented a combination of various techniques discussed in Chapter 2 and involved work with several collaborators, in particular A. Koch.

- Hyde, E. A., Zucker, D. B., Keller, S., Siebert, A., Ibata, R., Peñarrubia, J., Martell, S. L., Lewis, G., Irwin, M., and Koch, A. *Selecting Sagittarius: A Study Of Sagittarius Dwarf Members Throughout The Milky Way Galactic Halo.* American Astronomical Society Meeting Abstracts **221**, 425.03 (2013)
  − This AAS thesis talk presented an overview of my entire research project, including the stream and core selection, potentially interesting datasets and a discussion of the data reduction. The science incorporated contributions by collaborators on the project, including stream data from R. Ibata and abundances from A. Siebert.

Abstract

The Sagittarius dwarf galaxy obtained its name from the constellation of the Archer, in which it lies. The dwarf spheroidal itself is part of a much larger system, the parent to a stream of stars which gracefully arches around the entirety of the Milky Way. This system of the Sagittarius dwarf and stream can help us probe how galaxies like the Milky Way formed, and what the dark matter halo of our Galaxy looks like. The current hierarchical scenario for galaxy development holds that many smaller mergers eventually built up into larger galaxies, such as the one we reside in now. The left over building blocks from the process of galaxy assembly should remain identifiable today as distinct structures in the smooth Milky Way halo. The Sagittarius dwarf and stream provide us with the best studied, and most complete, example of such a structure.

We investigate the Sagittarius system in detail, obtaining and analysing new spectroscopic data from the Anglo-Australian Telescope. This research project entailed the selection of candidate Sagittarius members from existing photometric data, followed by detailed spectroscopic observations of over 24,110 stars in regions of the Sagittarius dwarf and stream, a sample roughly an order of magnitude larger than previous studies. For each of these stars, we measure kinematics and metallicities. The project is primarily observational, examining the properties of the Sagittarius system, with a comparison to existing models in order to constrain the mass profile of the Milky Ways dark matter halo, through which Sagittarius falls.

We find that the distribution of stellar radial velocities in the core corresponds to the predictions of a pressure-supported model for the progenitor to the Sagittarius dwarf galaxy and stream system. We also note that the average metallicity appears to rise in the innermost two degrees of the Sagittarius dwarf core, a property that has been observed in other Local Group dwarf galaxies. We develop a new selection technique to distinguish Sagittarius stream members from a model of the smooth Galactic halo, and find reasonable agreement between our data and the predictions of a simulation in which Sagittarius orbits a Milky Way with a triaxial dark matter halo. This selection technique also yields a surprise detection of the Sextans dwarf in the region of the Sagittarius stream. We additionally apply our methodology to observations of a single field in the Orphan Stream, with promising results.

The results of this thesis, both methods and data, have a number of important applications for future research. The technique developed here for distinguishing likely members of stellar overdensities from the smooth Galactic halo can be applied to other datasets covering other areas of the sky. The stellar velocities and metallicities obtained for the Sagittarius core and stream can be used to refine new models for the interaction of Sagittarius and the Milky Way, thereby constraining the properties of the progenitor and of the Galaxy's dark matter halo. Finally, follow-up observations of our targets (such as with high resolution spectroscopy) will allow more detailed analysis of the properties of Sagittarius as well as the other stellar structures identified in this work.

Contents

List of Figures

List of Tables

"No, no, you're not thinking; you're just being logical"

Niels Bohr

1

Introduction

The first galaxies were discovered by ancient astronomers. Visible to the naked eye, the Milky Way and the Andromeda galaxy have a rich history both in mythology and science. With the first basic telescopes that were pointed at the sky people could see that the Milky Way was not a single entity but was in fact made up of individual stars. However, it wasn't until after the Great Debate of the 1920s, between Harlow Shapley and Heber Curtis, that Andromeda was accepted as a external galaxy to our own Milky Way. Our pursuit of understanding galaxies has widened substantially as we have begun to be able to see more and more distant galaxies, from earlier and earlier epochs in time. To explain the existence and evolution of these galaxies a model of formation is needed.

The standard cosmological model used to describe how our Universe was formed is the Big Bang model. In its simplest form, this model states that the Universe was once very hot and dense, and expanded from that initial hot dense state. The predictions from the Big Bang model have so far been in a general agreement with observed phenomena in our Universe. The relative abundances of light elements indicate a hot Big Bang with low baryon density. The COBE satellite mapping of the cosmic microwave background (CMB) showed uniformity indicating large scale isotropy/homogeneity and the CMB Planckian spectrum indicates a hot, dense early Universe. Notably, the Big Bang model provides an explanation for the observed expansion of the Universe, the large scale structure seen in the Universe, and the CMB.

The evidence for dark matter in the Universe can be seen by looking at the rotation curves of galaxies and the gravitational lensing of light by galaxy clusters. The amount of dark matter currently seems to make up about 23% of the mass-energy density in the Universe, and dark energy about 72-75%. Notably, it is the remaining $\sim 5\%$ of mass-energy density in the Universe that comprises the baryonic matter and electromagnetic radiation that make up the stars, planets, and all of us. The level of structure formation seen in galaxies today suggests the cold dark matter (CDM) formulation.

The cosmological principle that our Universe can be treated as both homogeneous and isotropic on large scales means that, on average, properties are the same everywhere and in every direction. The geometry of the Universe is considered to be flat, and given current estimates of mass the Universe appears to be expanding fast enough that it will never collapse back in on itself. Observations have shown that distant supernovae are fainter than expected from a constant expansion rate, which indicates an accelerating expansion. This acceleration of expansion is interpreted as an indication of dark energy (Λ), or vacuum energy, which causes empty space to expand on very large scales of the Universe. The Λ represents the cosmological constant, which is an expression of the dark energy of the Universe.

Together, CDM and Λ dark energy provide the ΛCDM formulation, the physical description of the Big Bang model. ΛCDM is the current leading paradigm for our understanding of the Universe, predicting how the Universe should behave as determined by the laws of physics as we know them today.

1.1 Predictions of the hierarchical model: current views of galaxy formation

The growth of structure in a ΛCDM Universe can be modelled in numerical simulations, and so far there has been correspondence between these models and observations of the Universe on the largest scales. Unfortunately there are still many problems matching models to observations at the scale of the Local Group galaxies. The currently dominant scenario is one of 'hierarchical' galaxy formation. In this theory smaller galaxies build up to form the larger ones we see today in a bottom-up process. This process was first introduced by Searle & Zinn (1978) when they proposed that smaller object mergers could build up into larger galaxies.

In ΛCDM, galaxies form within dark matter halos. These halos form in the early universe when the matter in '*an overdense region suffers gravitational retardation, decouples from the Hubble flow, collapses, and in due course virializes*' (Williams et al. 2004). The theoretical framework of this process was laid by Gunn & Gott (1972); Gott (1975); Gunn (1977) and Fillmore & Goldreich (1984); Hoffman & Shaham (1985). These studies predicted power-law density profiles, where the average dark matter density of a dark halo depends on distance from the halo centre. This work led the way for higher resolution simulations like those of Navarro et al. (1996, 1997).

The work of Navarro et al. (1996, 1997) and many others showed that the spherically averaged density profiles of dark matter halos behave in a very similar way in halos of all masses at all times. This is described by the universal profile shape:

$$\rho(r)/\rho_{crit} = \frac{\sigma_c}{(r/r_s)(1+r/r_s)^2} \tag{1.1}$$

as discussed by Navarro et al. (1996). In this case r_s is the characteristic radius or 'scale radius' and $\rho_{crit} = 3H^2/8\pi G$ is the critical density. The parameter σ_c is used to describe the characteristic over-density of the halo. Navarro et al. (1996) find that the halo concentration decreases systematically with increasing mass. What this means is that less massive halos and halos that form earlier have higher densities (larger σ). The basic profile from Navarro et al. can be scaled to match observations of most halos.

Three main problems have been identified in the ΛCDM hierarchical galaxy formation scenario. The first is the core/cusp problem (Dalcanton & Hogan 2001). That is, according to the ΛCDM models, the density profile of galaxies should have a central cusp. This cusp takes the form of a density profile which varies as $\rho \propto r^{\alpha}$ where α is not the same for the inner and outer regions of the galaxy in question. Unfortunately this density profile feature has not seen in the observations. In particular among low mass dwarf galaxies this seems to be a fundamental problem. The second problem is known as the angular momentum problem. This conflict is created when the size and angular momentum of simulated galaxies are compared to real observations. The simulated galaxies appear to be 'too small', i.e. having too little angular momentum (Navarro et al. 1995; Navarro & White 1994; Navarro & Benz 1991). Finally there is the so-called problem of the missing satellites (Moore et al. 1999). Simulated dark matter halos have a great deal of substructure, orders of magnitude larger than has been seen around galaxies such as our Milky Way (Klypin et al. 1999; Kravtsov 2010). This last problem may be due to ultrafaint satellites which have yet to be identified, and it may also be due to a significant fraction of dark matter substructure which is star-free or even fully baryon free.

We will concentrate in particular on this last problem of the missing satellites. The dynamical timescales in the outer halo of the Milky Way are quite long and we expect structures like stellar streams to persist up to the present day. By identifying further structure in the Milky Way halo and disk we may be able to find evidence of some of these 'missing' objects, although we note that we would not expect them in the Milky Ways' inner halo as there the dynamical mixing timescales will be quite short and most evidence for past interactions would be erased. To look for surviving structures we need to be able to sample a large number of stars over a large portion of the smooth halo. The large and bright structures have long obscured our view of small streams and clusters in the halo (especially near the Galactic plane) and the true number of streams and satellites in our halo remains unknown.

Looking locally we can hope to address some of the main problems today in Galactic Archaeology, in particular the problem that, although the ΛCDM halos agree well with the observed structure of galaxy halos (from lensing and satellite motions) and cluster halos (observed from lensing and X-ray data), there appear to be disagreements within the inner part of galaxies between models and observations. In addition the evolution and formation of the dark matter halos of galaxies are still not well understood. We do not yet know if all of the dark matter in our Galaxy is part of the halo, and if so, if it has always been there or if it has migrated there somehow. The growth, accretion, and mergers of dark matter halos are a problem since it is unclear what dark matter is made of, and as of yet, we do not even have a good picture of the dark matter distribution in our own Milky Way.

1.2 The importance of streams and remnants

From observations of streams and remnants of dwarf galaxies in the Milky Way we can address the missing satellite problem of the hierarchical model as well as probe the halo potential that they sit in. By finding fainter and more diffuse streams and remnants we will get a more accurate count of the amount of debris around our Galaxy and see if there remains a shortage of small satellites. A stream in the halo should be closely aligned with the orbit of the disrupting satellite from which it originates, for example a small dwarf galaxy. By tracing the movement of those satellites through their streams we can use the profile shape described in Equation 1.1 to investigate the structure of dark matter halos.

We know that we can probe the structure of dark matter in the Galaxy by looking at the way streams and satellites in the Milky Way halo behave. For example, Ibata et al. (2001) discovered a stream of stars between the present location of the Sagittarius dwarf and a distant carbon star, at ~ 60 kpc (this stream is discussed in detail in Chapter 4). The stream was found to have an orbit that was inconsistent with either a polar or a Galactic plane orbit and its discovery provided one of the best examples of Galactic cannibalism in the Milky Way. Its large range in both Galactic longitude, latitude and distance puts it in a class of its own and, the fact that it was observed as a great circle indicates that '*the Galaxy does not exert a significant torque on the stream, so the*

Galactic potential must be nearly spherical in the regions probed by the stream' (Ibata et al. 2001). This restriction on the Galactic potential is also a restriction on the dark matter halo itself since the majority of the mass in the Milky Way is dark matter.

The number of small dark matter sub-halos predicted in ΛCDM (Moore et al. 1999; Klypin et al. 1999) is much larger than the number of known Milky Way satellite galaxies; hence looking at the Milky Way satellites and getting a more accurate distribution may resolve some of these differences (Peñarrubia et al. 2005). In particular the discovery of additional tidally stripped satellite galaxies in the Milky Way (Ibata et al. 1994; Newberg et al. 2002; Jurić et al. 2008), Andromeda (Ferguson et al. 2005; Ibata et al. 2007) as well as the recent Local Group compilation of McConnachie (2012) increased the number of known satellite galaxies. Though other explanations for the relative lack of visible satellite galaxies are possible, as of yet we cannot distinguish between them. While probing the structure of dark matter halos we can address the reason why we do not see stars tracing these sub-halos. The lack of visible stars could be because dark matter sub-halos were unable to create stars, or alternatively, the dark matter sub-halos with stars could just be more massive than those without stars.

Walker et al. (2009) find that the main body of Sgr has a half-light radius that is slightly larger than the scale radius of the best-fitting universal Navarro et al. (1996) halo (as described in Equation 1.1). Otherwise the scaling relations show that Sgr falls neatly onto the best-fitting power-law profile. Walker et al. (2009) suggest that a common dSph mass profile, this profile emerges from masses which relate directly to dynamical properties like tracer density and velocity dispersion and do not require any extrapolation to radii beyond the optical extent of the galaxy in question. However it was found that although a universal mass profile does appear to unite Milky Way dSph galaxies, M31 satellite masses are systematically smaller than their MW counterparts (Walker et al. 2010). For any dSph galaxy we expect that it will be dominated by dark matter even at its centre, but a truly universal mass profile may depend on more rigorous formulations that can take into account the details that shaped the different populations involved.

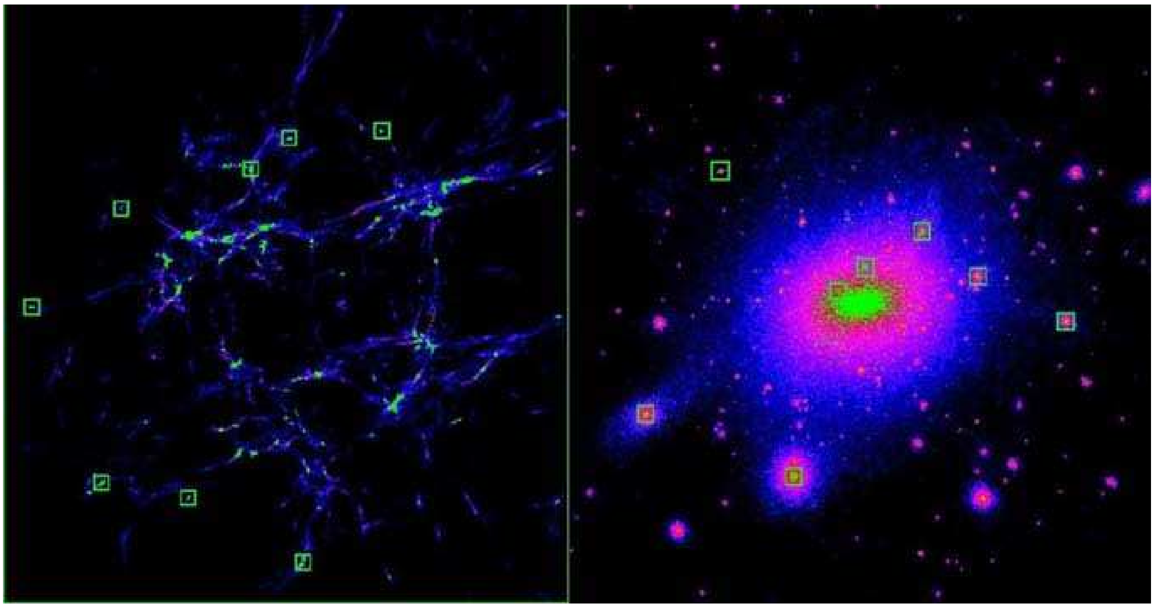

Figure 1.1: Simulated distribution of galaxies for $z = 10$ (left) and $z = 0$ (right) reproduced from Fig.1 of Moore et al. (2006).

The relationship between dark matter halos and host galaxies has often been a subject of modelling, in particular investigating the spatial distribution of satellites in our Milky Way. Figure 1.1 shows the difference in the expected distribution of satellites at distant galaxies (i.e. those far in the past) versus nearby ones. Surviving Galaxy satellites at redshift $z = 0$ would have been the most distant sub-halos at $z = 10$, i.e. the last to fall into the Milky Way. Looking at the Galaxy, Moore et al. (2006) point out that we have several distinct old stellar components. These different pieces provide a sort of 'fossil record' for the formation of our Galaxy. The earliest infall would have come from matter that was the closest; these stars would now be spread out among the debris of the stars and star clusters of the halo. The dispersed nature and advanced age (and thus faint visual magnitude) of the early infall objects makes them hard to observe. The different orbital shapes and correlations should tell us how the infall of stars proceeded at each epoch, and the kinematics of the early and the late infall should be different. The simulations of Moore et al. (2006) may help explain some of the details of this process. They use hierarchical structure formation simulations to try to predict what the distribution of these structures that made up the 'earliest infall' would be today. Since the observed radial velocity dispersion of galaxies appears to match the modelled results this may be one potential solution to the 'missing satellites' problem (Moore et al. 2006).

Looking at models for dark matter halos, Peñarrubia et al. (2008) examine the dynamics of stellar systems which are embedded within CDM halos to provide constraints on the dark matter content of Local Group dwarf spheroidals (dSphs). They investigate the distribution of stars in dSph galaxies using N-body simulations to confirm that the total mass and 'luminosity radius' (size) is independent of the luminosity of the dwarf. The total mass of less luminous (smaller) dwarfs was shown to be similar to larger, more luminous dwarfs. Peñarrubia et al. (2008) show that the average density of dark matter is higher in physically small systems, i.e. small dwarf galaxies have a higher density of dark matter than larger galaxies.

1.3 Streams and remnants in the Milky Way

Although several streams have recently been discovered around our neighbor galaxy M31 (Martin et al. 2014), the Milky Way halo is still the primary region of study for streams and remnants. Our Galaxy is known to host several streams, and, as we become more able to discern these objects, both with larger surveys and with superior statistical methods, more and more streams and remnants of streams are being detected. Large area photometric surveys have shown that the Milky Way is embedded in a veritable '*field of streams*' (Belokurov et al. 2006b), including the Sagittarius dwarf galaxy (e.g., Majewski et al. 2003; Belokurov et al. 2006b), as well as narrow, delicately-shaped streams such as those from the disrupting globular clusters DG-1 (Grillmair & Dionatos 2006), Pal 5 (Odenkirchen et al. 2003) and NGC 5466 (Belokurov et al. 2006a).

The elliptical overdensity in Canis Major was found to be coincident with a grouping of globular clusters (NGC 1851, 1904, 2298 and 2808) from Martin et al. (2004). It has been suggested that this set of objects may be the remnants of the dwarf galaxy progenitor of the Monoceros stream although models have shown that the distances of the stream and Canis Major show some discrepancies (Peñarrubia et al. 2005). The Monoceros stream is a ring-like structure seen as a overdensity of M-giants. This system is thought to have been a building block to the galactic thick disk and is representative of the type of disrupted system that can occur when a dwarf galaxy is absorbed by the Milky Way.

These systems tend to cover extended areas. The Virgo overdensity (VOD) (Keller 2010) for example includes three halo substructures; two overdense regions with radii of 1.3 and 1.5 kpc and an extended feature that covers at least 162 $\deg^2$ (also known as the Virgo Equatorial Stream), but the entire structure may yet be hidden (Newberg et al. 2007). Likewise, the 'Orphan Stream', so named for its lack of an obvious progenitor (Belokurov et al. 2006b; Grillmair & Dionatos 2006) is in excess of 500 pc (>1 degree on the sky) and has a noticeable heliocentric distance gradient (Belokurov et al. 2007a). Dwarf spheroidals with extended substructure such as the Sculptor dwarf spheroidal galaxy (Westfall et al. 2006), and globular clusters with identified tidal tails such as Palomar 5 (Odenkirchen et al. 2001) and NGC5466 (Belokurov et al. 2006a) add to this picture of disrupting dwarfs creating streams and donating globular clusters to our own Galaxy.

We discuss the Virgo overdensity, the Palomar 5 globular cluster (Harris 1996) and the Sextans dwarf (Irwin et al. 1990; Irwin & Hatzidimitriou 1995) in Section 4.3.2 in the context of overdensities in the Milky Way smooth halo. We additionally investigate the Orphan Stream spectroscopically in Chapter 5. There is, however, one stellar stream structure that is more complete and wider ranging than all of the rest, the system of the Sagittarius dwarf and its stellar stream, which wraps around the entirety of the Milky Way.

1.4 The Sagittarius dwarf and stream

The dwarf spheroidal galaxy in the constellation of Sagittarius (also known as the Sagittarius dSph) is located at a Right Ascension of 18:55.1 (h:m) and a Declination of -30:29 (deg:m). It is at a heliocentric distance of D$= 26.30 \pm 1.8$ kpc and spans an apparent dimension of 190 by 490 arc minutes on the sky (Monaco et al. 2004; Ibata et al. 1994). This small galaxy was detected in 1994 by R. Ibata, M. Irwin, and G.

Gilmore using stellar brightness density investigations (Ibata et al. 1994). At the time of its discovery the Sagittarius dSph galaxy was found to be the new 'nearest neighbour' to our Milky Way, being much closer than the Large Magellanic Cloud (considered to be our closest companion until then). In 1994 this dwarf galaxy was described as a '*large, extended group of co-moving stars in the direction of the Galactic Centre*' (Ibata et al. 1994). The Sagittarius (Sgr) dwarf still holds the title of our nearest intergalactic neighbour, although it might lose its place to the still debated Canis Major stellar overdensity if the latter can be conclusively shown to be a dwarf galaxy.

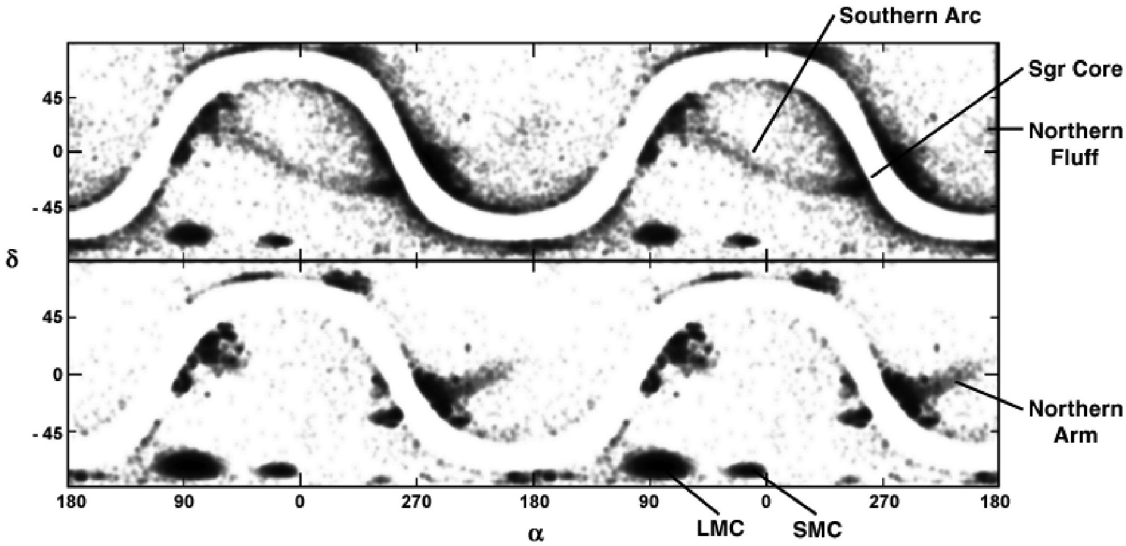

FIGURE 1.2: Reproduced from Figure 3 of Majewski et al. (2003) showing the Sgr stream from the 2MASS point source catalog. The top window shows the southern arm and the bottom window the northern arm for two cycles around the sky. The colour cuts used are: $11 \leq K_S \leq 12$ and $1.00 < J - K_S < 1.05$ for the top panel and $12 \leq K_S \leq 13$ and $1.05 < J - K_S < 1.15$ for the bottom panel.

To investigate further we should first clarify what we mean by Sgr dwarf galaxy. The nomenclature of Sgr dwarf does not refer to the same galaxy as SagDIG (Sagittarius Dwarf Irregular galaxy), a different object altogether. Furthermore, the 'Sagittarius I Dwarf' or similarly ambiguous names occasionally occur in websites, databases, articles and papers, but for the sake of clarity we define all references to the Sgr dwarf in this thesis to mean the Sagittarius dSph discovered by Ibata et al. (1994).

Unlike the dwarf irregular galaxy with a similar name, the Sgr dwarf has a dominant old stellar population. The age of the Sgr dwarf is thought to be about 10-12 Gyr Sarajedini & Layden (1995); Mateo et al. (1995, 1996); Fahlman et al. (1996); Siegel et al. (2007). Its star formation so far indicates that the star formation in the Sgr dwarf began quite early on but peaked and then abruptly decreased about $8-10$ Gyr ago (Bellazzini et al. 1999c,b,a, 2006a). The time needed for M giants within the main body of the Sgr dwarf to diffuse and reach the extent seen in the tidal tails of Sgr is estimated as $\simeq 3-4$ Gyr, which is well within the time they would have since their birth, i.e., $\simeq 5.5-9.5$ Gyrs (Bellazzini et al. 2006a).

The main population in the Sgr dwarf is a predominantly old one (referred to as Pop A) with an extended red giant branch. This Pop A group was found to have a large spread of metallicity, 0.7 to 0.8 dex, i.e. from $-1.3 \leq$[Fe/H]≤ -0.7 (Bellazzini et al. 1999a,b). This spread indicates a range of ages of about 8-10 Gyrs (Bellazzini et al. 1999b,a) although Siegel et al. (2007) found a three population set of ages of 4.5, 6 and 13 Gyrs stretching from intermediate to old ages. There is a small younger population, but it will play only a minor role in our investigations. The star formation episodes are thought to have been brought on by the initial interaction between the Milky Way and the Sgr dwarf progenitor. The large metallicity spread seen by Siegel et al. (2007), Bellazzini et al. (1999a) and others indicates that the episodes of star formation occurred on large scales, scales comparable with the dimensions of the Sgr dwarf. Since the two body relaxation time for the Sgr dwarf and Milky Way system is much greater than a Hubble time efficient star mixing is unlikely, adding support to the idea that stars in the Sgr dwarf formed everywhere at the same epoch (Bellazzini et al. 1999a). These stars now form the dim and diffuse structure we see today as the Sgr dwarf and its associated stream.

The low surface brightness of the Sgr dwarf and stream are one of the key features that helped it to remain hidden for so long, as pointed out by Ibata et al. (1994). The Sgr dwarf is also viewed in projection near the bulge of the Milky Way, so foreground stars and extinction are obstacles to its study. A final feature that hindered early observations is that the Sgr dwarf is, in fact, not all there: it is in the process of being disrupted by its massive neighbour, our Milky Way. This disruption was first noticed as an elongation towards the plane of the Milky Way, and has since then been found to be a truly significant structure, known as a stellar stream, made of stars from the Sgr dwarf, which wraps around the entire Milky Way.

We note that the globular cluster M54 is also at about the same distance as the Sgr dwarf and is thought to be related to the Sgr dwarf. This would make it the first 'extragalactic' globular cluster discovered (first noted in 1778 by Charles Messier). When the Sgr dwarf is finally completely disrupted, the M54 cluster and several others will survive as 'remnants' while the other stars are spread over the Galactic halo (or in some cases escape after dynamical ejection). A few other globular clusters are suspected to be related to Sgr, but because M54 is much brighter than the others, and located in the centre of Sgr, it has been proposed that it might be the remnant of a nucleus for the Sgr dwarf. This possibility is discussed in Section 3.4.

Given that it is currently thought that the Sgr dwarf orbits the Milky Way in less than one billion years, it is a bit surprising that it is not more disrupted. The longevity of the Sgr dwarf was pointed out several times, including by Martínez-Delgado et al. (2001) and Martínez-Delgado et al. (2004), when they modelled the Sgr dwarf. We believe that it must have passed the dense central region of our Galaxy at least ten times, given current age estimates. That the Sgr dwarf still exists after so many orbits suggests the presence of significant amounts of dark matter within this small galaxy, which would help keep its stars bound together.

One analysis of the Sgr dSph was performed in Ibata et al. (1997), illustrating the usefulness of streams as probes for dark matter in the Milky Way halo dwarf galaxies. The Sgr galaxy that they model is one of the closest satellites to the Milky Way and is thought to have survived for many orbits around the Galaxy. Ibata et al. (1997) use numerical calculations to model the Sgr dwarf as '*a system with a centrally-concentrated mass profile*'. They found that it should lose more than one-half of its mass every 2-4 orbits and be completely disrupted long before now, which is obviously a problem for the model since we still see it today. However, as they mention in the paper, this implies that Sgr (and therefore other dwarf galaxies) do not have a centrally-concentrated profile for their dark matter. Ibata et al. (1997) then show that a model in which the stars of the Sgr dwarf are embedded in a constant-density dark matter halo is consistent with its survival. Using the stream they were able to predict a dark matter content for the Sgr dwarf that would allow it to survive till the present day.

The first all-sky view of the Sagittarius dwarf galaxy was presented by Majewski et al. (2003) as shown in Figure 1.2. The 2MASS survey detection of the M-giant stars which trace the Sgr dwarf galaxy by Majewski et al. (2003) provided a very clear view of the centre of Sgr. This data they use is selected from the photometry as shown in the colour-magnitude diagram (CMD) of Figure 1.3, where the Sgr red giant branch is separated out. The Sgr radial profile closely resembles that of dwarf spheroidal satellites (dSph) of the Milky Way.

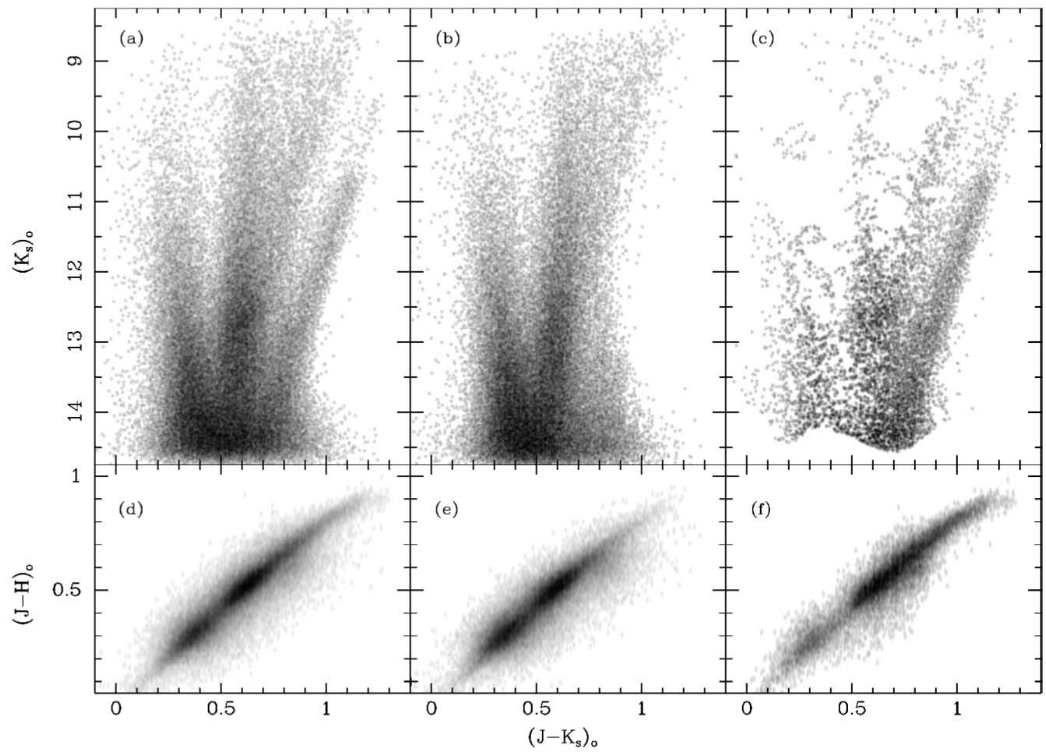

Figure 1.3: Near-infrared (J-Ks, Ks) Colour-Magnitude-Diagrams from Fig. 1 of Majewski et al. (2003). The panels are (a) the Sgr centre, (b) a control field of identical area and Galactic coordinates reflected about $I = 0°$, and (c) a star by star subtraction of (b) from (a). Panels (d)-(f) show the corresponding (J-Ks, J-H) two-colour diagrams for the samples shown in (a)-(c).

Majewski et al. (2003) fit the main body of Sgr with a King profile (King 1962, 1966) using a limiting major-axis radius of 30° (substantially larger than previously found or assumed). This fit to Sgr allowed Majewski et al. (2003) to make a cut, beyond which they find a break in the density profile from stars in the Sgr tidal tails. The break in the density profile means that the Sgr radial profile is quite similar to that of other Galactic dwarf spheroidal satellites.

The distribution of M-giant stars mapped out in Majewski et al. (2003) shows the 'leading arm' of Sgr debris (the Sgr stellar stream) in Figure 1.2. The distribution is used as support for a 'nearly' spherical Galactic potential, and to determine dark matter distribution in the Galaxy. It is suggested that the Sgr core may have experienced a recent and catastrophic mass loss, which shows that it is still very much in the process of being destroyed by our Galaxy. This picture of the Sgr dwarf and its 'tidal arms' is a key piece in the puzzle of how the accretion of dwarf galaxies works. Despite extensive efforts, current models (e.g., Law et al. 2005; Law & Majewski 2010) of the Sgr dwarf system are unable to explain all the observed features.

1.5 Thesis overview

Understanding the properties of the stellar streams and surviving satellites around large galaxies is critical for understanding the process of galaxy assembly and for probing the role of dark matter in bringing about the Universe we see today. In particular, the Milky Way and its nearest neighbours provide an invaluable testbed for models, as here, detailed observations are possible. The existing accounts of streams in the Milky Way fail to resolve the missing satellite problem completely although more streams are being found as observations improve. Wrapping around the Milky Way, the Sagittarius (Sgr) stream is one of the most dramatic examples of a stellar tidal stream currently known. Although extensive research has been carried out on streams in the Milky Way and the Sagittarius stream in particular, no single study exists which adequately covers the formation and properties of the Sgr dwarf and stream. The progenitor for the Sgr dwarf and stream system has been assumed to be a non-rotating, pressure-supported dwarf spheroidal galaxy. However, to date, *no* such model for the interaction of Sgr with the Milky Way has been able to reproduce all of the observational features of the stream (Peñarrubia et al. 2011). Recent theoretical models proposing that the progenitor was a rotating disk galaxy (Peñarrubia et al. 2010) predict that the core should still show residual internal rotation with a measurable amplitude (~ 20 km s^{-1}).

This project began as a test of the origin of the Sgr dwarf. We used the initial fields to show that there was no rotation in the core of Sgr (Peñarrubia et al. 2011) as had been postulated by Peñarrubia et al. (2010). Although the observational data did not support the rotating disk hypothesis, the potential of such data for testing models was clearly illustrated. This then led to an expansion of the project, encompassing a full mapping of the Sgr dwarf core region as well as a sampling of observations across the entire Sgr stream. Tracing out the Sgr dwarf and its stream with spectroscopic measurements allows us to determine the properties of this structure, and by extension, constraints on others. We discuss the data reduction in Chapter 2, and use the initial observations of the core to illustrate the reduction process. The initial observations of the core region as well as our expanded Sgr core dataset are fully analysed in Chapter 3, where we discuss the kinematics and chemical properties (i.e., the metallicity) of the Sgr core. The full Sgr dataset, focusing on the properties of the stream, is described in Chapter 4, where we develop and apply a new technique to separate out Sgr stream stars from the halo. This method is then tested on data from a single observation of the Orphan Stream in Chapter 5. The final results are summarised in Chapter 6.

"A mere matter of detail, a bagatelle"

On going to the Moon, Jules Verne - Earth to the Moon

2 Description of Data and Data Reduction Techniques

2.1 Introduction

As mentioned in Chapter 1, our investigation into the Sgr system began as a test of the rotating disk galaxy hypothesis of Peñarrubia et al. (2010). If true, this hypothesis would provide a new origin scenario for the Sgr dwarf and stream in the form of a rotating disk galaxy. That rotation would still be visible today in the remnant core with a measurable amplitude, predicted to be ~ 20 km s^{-1}. To investigate this possibility, and check for rotation, we initially obtained spectra of over 7000 stars near the core of Sgr (the central region in Figure 2.1) with the AAOmega spectrograph on the Anglo-Australian Telescope (AAT) described in Section 2.3. We present here our preliminary results from that data set (the Core 1 region) and our data reduction methods.

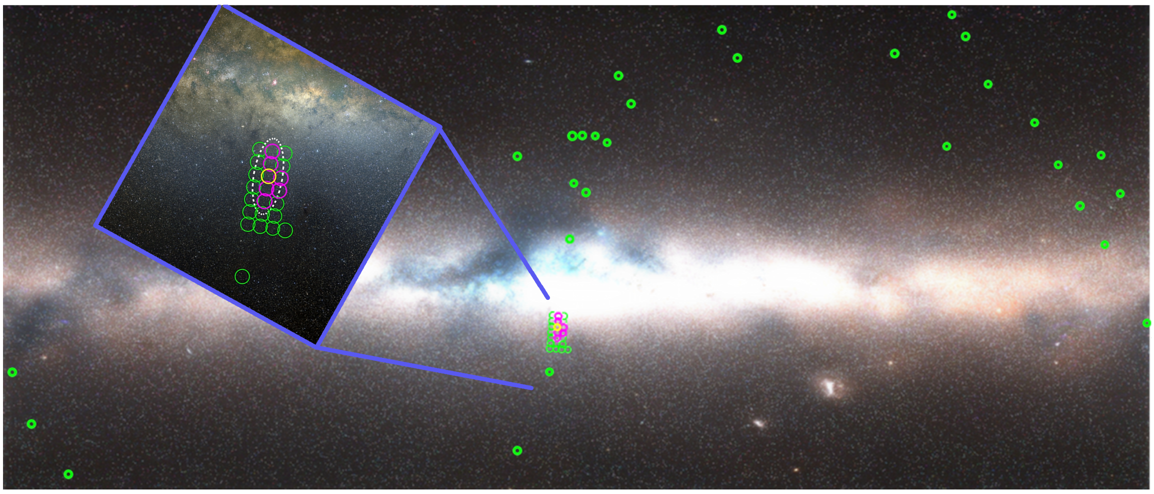

FIGURE 2.1: Our Sgr dwarf and stream observations. Each field is two degrees in diameter. The Sgr dwarf core is located in the centre yellow circle and the central rectangular block of pointings makes up the 'central region' R01. The red circles are the first set of observations taken (Peñarrubia et al. 2011). Background image from Mellinger (2009).

2.1.1 Obtaining stellar parameters with spectra

From the data reduction, the main stellar parameters that we want to obtain are the radial velocity and metallicity. We can use the shift in the wavelength of lines in the stellar spectrum of the star to give us a radial velocity measurement for the object. Its velocity can help us determine if it is part of our Galaxy's smooth halo, a member of Sagittarius, or from somewhere else altogether.

The members of the Sgr dwarf form a metallicity distribution with an average value of [Fe/H] ~ -0.5 dex (Cacciari et al. 2002; Bonifacio et al. 2004; Monaco et al. 2005). The metallicities of stars in galaxies as they develop with time is key to understanding and characterising the evolution of the galaxy as a whole. In the case of the Sgr dwarf the distribution of metallicities in the core region has a width of ≥ 2 dex (as shown in Chapter 3). This wide distribution of metallicities precludes us from using it as a selection criterion, although if we can find a gradient in the metallicity with distance from the Sgr core we may be able to tell something about the progenitor object for the Sgr dwarf and stream (as discussed in Chapter 4). For any investigation we must first find an accurate representation of the metallicity in our stars. The first step in this investigation is the infrared calcium absorption triplet, which can be used to find an estimate of metallicity. These spectral lines have rest wavelengths of 8498, 8542, and 8662 Å, respectively. These three lines are sufficiently strong and broad that they can be measured with reasonable accuracy even in medium to low resolution spectra, providing both velocity and metallicity estimates. The calcium triplet has been used to characterise the metallicity of stars in faint dwarf galaxies and dwarf spheroidal galaxies, as well as individual stars (e.g., Da Costa et al. 1991; Suntzeff et al. 1993; Helmi et al. 2006; Norris et al. 2010b).

The metallicities we might expect to find in dwarf spheroidal galaxies have changed over time. It was noted by Helmi et al. (2006), using a traditional calcium triplet calibration, that the dSph galaxies Sculptor, Fornax, Carina and Sextans were lacking in stars with metallicities [Fe/H] ≤ -3, but with alternative measurement techniques dwarf galaxies have since been found to host lower metallicity and even extremely metal poor (EMP) stars. In particular Norris et al. (2008) use the re-calibrated calcium K line strength index (from Beers et al. 1999), while Kirby et al. (2008b) and Koch & McWilliam (2010) directly measure iron lines. The potential bias due to the calcium triplet is addressed in Koch et al. (2008a) and Starkenburg et al. (2010, 2011), who note that linear calibrations of the triplet (Rutledge et al. 1997a) start to break down below [Fe/H]$= -2$. A new calibration for the calcium triplet is provided by Starkenburg et al. (2010, 2011) which is valid for the metallicity range $-0.5 \geq$[Fe/H]≥ -4 dex. In this thesis we will primarily look at two methods for the calcium triplet. The first involves using our own template to fit the data to a Gaussian equivalent width and create a linear calibration with metallicity as mentioned above. Our second method is explored in Section 2.6, in which we compare to an independent pipeline which has an extended template library.

2.2 Target selection

Our initial selection of targets was designed to look for M and K-giants in the predicted location of the Sgr dwarf. The selection of stars we observed at the AAT was carried out in three different stages, yielding the overall spatial distribution shown in Figure 2.1. The Core 1, R01 and stream sets are analysed in different parts of this thesis as discussed in Chapter 1. All stars observed near the core (Core 1 and R01) were selected from the Two Micron All Sky Survey (2MASS) (Skrutskie et al. 2006) catalog. The colour and magnitude cuts for R01 are $9 < K < 13$ and $J - K > (20.0 - K)/90.0$ from Majewski et al. (2004). This selection does limit the data to a region where we expect the most Sgr member stars to be, i.e. an intermediate to older population of 8-10 Gyrs (Bellazzini et al. 1999b,a) and a metallicity range of $-1.3 \leq$[Fe/H]≤ -0.7 (Bellazzini et al. 1999a,b) as discussed in Section 1.4. This selection in turn gives us a range in visual magnitude of $V \sim 10 - 13$ for the R01 stars. The first Core 1 pointings we observed are shown in magenta in Figure 2.1 (shown in more detail in Figure 3.4). These data were taken throughout several observing runs on the AAT from 2009-2011 as discussed in Section 2.3. The R01 stars are discussed later in Chapter 3.

The target stars in the stream were selected with photometry from the Canada France Hawaii Telescope (CFHT) where possible and 2MASS photometry where CFHT data were not available. Stream stars were selected similarly to core stars if they had 2MASS photometry, and CFHT objects were selected in pointings which went to slightly fainter magnitudes to increase the number of stars available in some of the sparsely populated stream observations. Stream stars with 2MASS photometry were selected using a polygonal box of $J - K$ = (0.95, 1.35, 1.10, 0.95), K = (13.0, 10.0, 10.0, 11.125). Objects with CFHT photometry were selected in boxes corresponding to the 2MASS polygonal box which included blue horizontal branch, main sequence, red clump and red giant branch stars. The stream boxes were shifted in magnitude from observation to observation to maximise the number of possible Sgr targets observed. These slightly fainter magnitudes increased the number of stars available in some of the sparsely populated stream observations. As a result, the range of visual magnitudes is increased to $V \sim 12 - 18$ for the stream (corresponding to a g=20 limit). The slightly fainter stars in the stream result in fewer low error candidates from the modified RAVE pipeline when selecting Sgr members in Chapter 4. As mentioned previously, the stream and core regions together yield a total of ~24,110 spectroscopic observations for candidates associated with the Sgr dwarf and its stream.

2.2.1 Stellar populations

The Sgr dwarf was found to have a mean metallicity for the main stellar population of about [Fe/H]$= -0.5 \pm 0.2$ (Cole 2001) to [Fe/H]$= -0.4 \pm 0.2$ (Chou et al. 2007). As mentioned in Chapter 1, there is a wide spread in this main stellar population as well, $-1.3 \leq$[Fe/H]≤ -0.7 (Bellazzini et al. 1999a,b), and our new measurements discussed in Chapter 3 can help to improve the average estimates. The overlap between the red giant branch (RGB) of the Sgr dwarf and the foreground Milky Way giant branch suggests that about one-third of the RGB is more metal-poor than [Fe/H] $\simeq -1$ (Cole 2001). This indicates that we should expect metallicity values of around [Fe/H]$\simeq -0.5$ for our observations. Many of these selected stars are M and K-giants. The 2MASS JHK photometry permits a selection of M and K-giants from foreground stars.

From Dinescu et al. (2005) Sagittarius stars can be selected in terms of their colour. One method used previously in the literature for the Sgr dwarf is shown in Figure 2.2, where Dinescu et al. (2005) show an example using 2MASS photometry. The two boxes with solid lines in Figure 2.2 indicate Sgr's giant and asymptotic giant branches and the dashed box defines the locus of giants in the Galactic bulge. Dinescu et al. (2005) shift the box defined by Sgr's giant branch approximately 2.5 magnitudes brighter to correspond to the distance difference between Sgr and the bulge (the distance to Sgr is known to be approximately 25 kpc (Ibata et al. 1997) whereas the bulge is at about 8 kpc). The middle panel shows the 2MASS CMD, where stars within the areas defined above give the primary targets of Dinescu et al. (2005). At the bottom of Figure 2.2 they show the $[V_0, (J-K)_0]$ CMD and their selected candidates, Sgr candidates are filled triangles and AGB candidates

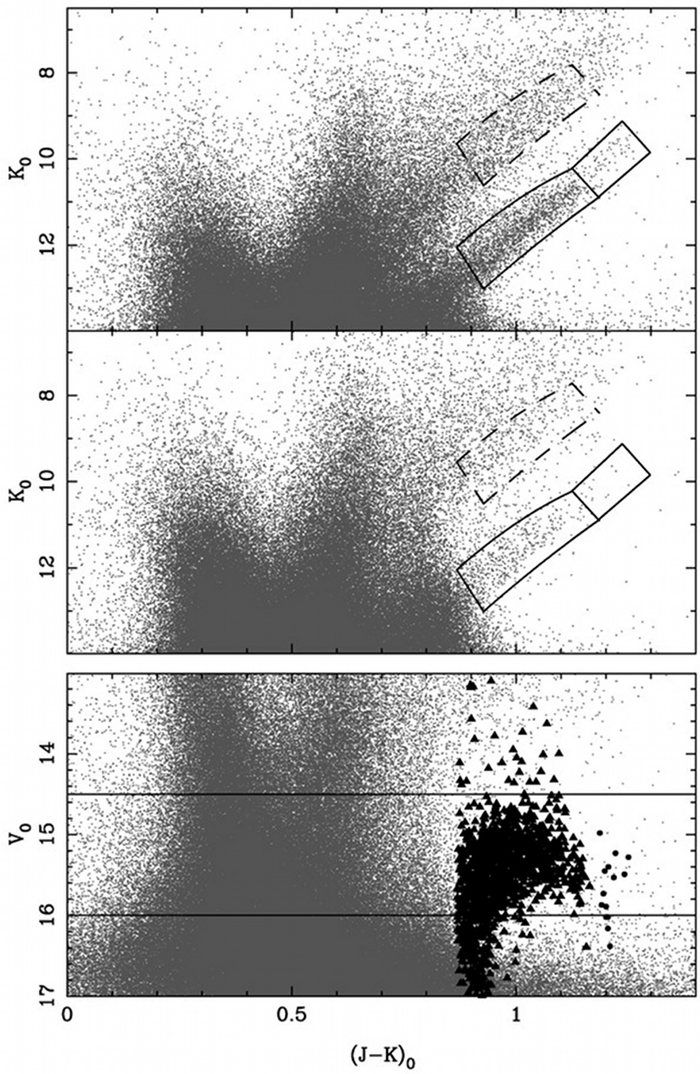

FIGURE 2.2: Shown above is a reproduction of Figure 1 of Dinescu et al. (2005). The top panel is a 2MASS CMD of Sgr's central region, defining the Sgr giant branch and AGB. The middle panel shows the 2MASS CMD of the area selected from the SPM 3 catalog to determine Sgr's proper motion. The bottom panel shows the $[V_0,\ (J-K)_0]$ CMD of the same area, with the 2MASS-selected Sgr giants highlighted (filled triangles). Filled circles are Sgr AGB candidates.

are filled circles. They propose a faint V-magnitude cut at $V_0 = 16$ and elimination of stars brighter than $V_0 = 14.5$ as foreground contaminants. This type of selection should be possible for our data as well. Figure 2.2 gives a general idea of what we can expect for our Sgr data (allowing for our individual colour cuts as shown in Figure 2.3).

Metal-poor main-sequence stars in the smooth Milky Way halo lie below the main-sequence for nearby disk dwarfs. Metal-line blanketing shifts the stars spectra, depleting the blue flux. Metals in stars can absorb some of the stars' radiant energy and re-emit it at a longer wavelength. This re-emission results in the stars with the highest metal content being pushed towards a redder colour as the metal lines (proportion of metals in the star) increase. A metal-poor star of a given mass is then found to the left side of the RGB.

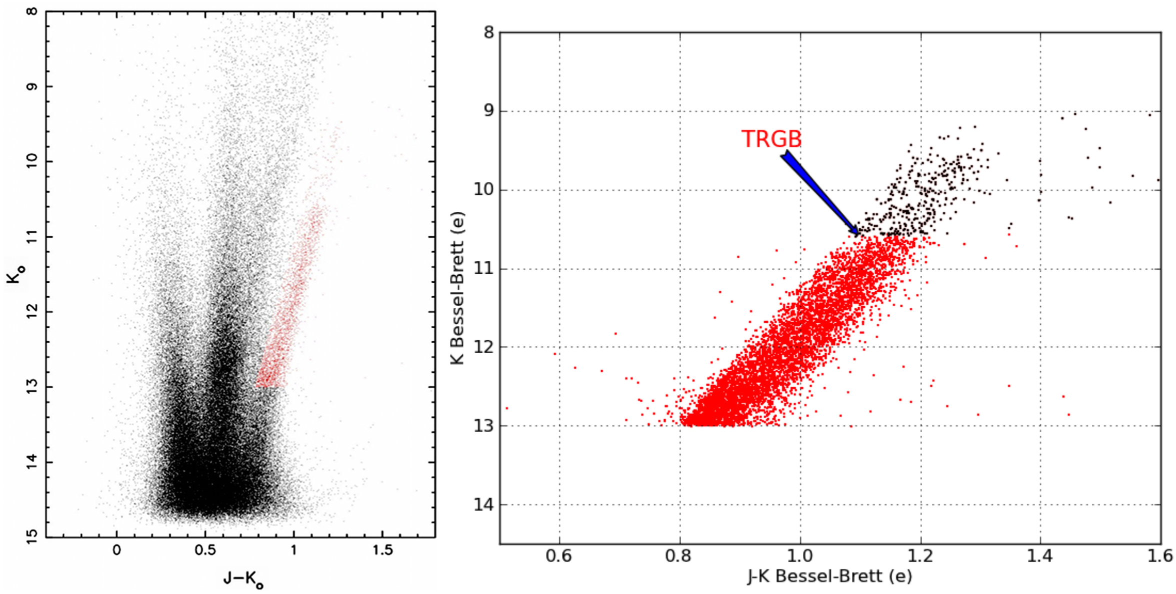

FIGURE 2.3: The extinction-corrected J,(J-K) CMD (left) of the central 4 square degrees of the core of the Sagittarius dwarf, with candidate RGB and AGB stars indicated in red (rightmost plume in the left panel with 10.5 ≤ K0 ≤ 13). The parallel plume of stars at ∼ 2 magnitudes brighter than the Sgr giants is part of the outer Galactic Bulge. There is a clear separation between Sgr giants and other contaminating foreground Galactic dwarf stars. The equivalent optical magnitudes of the Sgr giants we are targeting lie in the range 15 <V < 18. The selected giants are shown to the right with the AGB black in red and the RGB region in red.

We define a box of colour-colour space corresponding to asymptotic giant branch (AGB) stars to coincide with $9 < K_o < 11$ and $1.1 < (J - K)_o < 1.3$ (see Figure 2.3), which is roughly consistent with a cut at $K_o < 10.6$ for a plot of K versus $(J-K)_o$. These colours were de-reddened with the Schlegel dust map (Schlegel et al. 1998), as described by Equations 2.3 and 2.5. We can additionally see that the RGB blue tail does overlap with the foreground Milky Way giant branch stars. This overlap was used to show that about one third of the RGB is more metal poor than [Fe/H]< -1 and, indicated a metal-rich nature for the bulk of the Sgr population (Cole 2001).

In Figure 2.3 we show 2MASS stars within 1° of the centre of Sgr (the contamination from M54 is minimal as discussed in Chapter 3). The foreground F and G dwarf stars form a locus at $(J-K)_o < 0.5$ and come from thin and thick disk halo populations (at distances of a few kpc). The disk K and M stars form a locus around $\sim 0.5 < (J-K)_o < 0.75$. These main-sequence turn-off stars are in the foreground disk. We also have red clump stars which are found in the Galactic bulge and foreground disk, and RGB stars found in the bulge. The bulge giants form the brighter of the 2 diagonal plumes from $K \sim 13-18$. The Sgr giants that we select are highlighted in red on the left of Figure 2.3; above $K_o = 10.6$ we have M and K-giants and some C stars. We note that the C star frequency is quite low, which is expected for our colour cuts. Furthermore the Sagittarius dwarf is expected to have a much lower fraction of C stars than, for example, the Magellanic Clouds (Majewski et al. 2003). Our selection is then dominated by the RGB and some AGB stars in the M and K-giant range.

Our targets can be separated into AGB and RGB stars by using the tip of the RGB (TRGB) as shown on the right of Figure 2.3. The TRGB location shows where the onset of helium fusion begins in the degenerate cores of low mass stars. The TRGB is defined by a sudden drop in the density of stars when plotting the luminosity function N (or $\log$ N) vs $\mathrm{M_K}$ (the absolute K magnitude). It was noted by Valenti et al. (2004) the TRGB can be defined in the I band and a distance modulus can be obtained; the I band has a weaker dependence on metallicity and the TRGB can be used as a standard candle. This was done by Monaco et al. (2004) (see Table 3.1 for a full list of properties of the Sgr dwarf) who estimated $I^{TRGB} = 13.44 \pm 0.06$ mag. They showed that this selection limited the K magnitude at about 10.6 and quote an average error of 0.15 mag. Valenti et al. (2004) note that this selection does prefer stars at a metallicity of

$-1.0 \leq$[Fe/H]≤ 0.0, which is reasonable for the Sgr dwarf at about [Fe/H]$\simeq -0.4$ dex. This selection is also used by Cole (2001), McConnachie et al. (2005) and others who have a similar selection and a cuttoff of $K_o \simeq 10.6$. Following this work we define TRGB cutoff at $K_o = 10.6$ following the selection box used by McConnachie et al. (2005) and Majewski et al. (2004). If there is not a clean break in the luminosity function (e.g., if there is a cool AGB component) a sharp enough drop for TRGB detection should still be present.

We use the limits found here to do a cut at TRGB to exclude AGB stars when considering stellar metallicities. It has previously been noted that among stars of constant age and metallicity, the Ca II equivalent width measured for an RGB star can be larger than an AGB star at the same magnitude (Cole et al. 2000). We avoid this issue, as well as potential false low metallicity detections by excluding the AGB stars in our sample.

2.2.2 Bessell-Brett colours

Several different calibrations for the JHK colours are used. We use the 2MASS JHK as our standard and convert to Bessell-Brett JHK (Bessell & Brett 1988)[1]. This conversion will allow us to convert to absolute magnitudes to test our metallicity measurements later in this chapter. To convert to a standard Bessell-Brett colour we need to take into account extinction as well as the colour difference.

Our V magnitude is calculated from the given 2MASS colours for the star, which, using the conversion formula of Gaspar Bakos[2] is:

$$V = -0.0053 + 3.5326 * J + 1.3141 * H - 3.8331 * K \tag{2.1}$$

where J,H,K are the 2MASS colours.

To define the extinction correction we start with the extinction in the V magnitude:

$$A_V = Rv * E(B - V). \tag{2.2}$$

[1]The conversion is executed via the 2MASS website transformation equations at: `http:///www.astro.caltech.edu/ jmc/2mass/v3/transformations/`.

[2]Richard Lane, private communication

Assuming an extinction factor of $R_V = 3.1$ from Cardelli et al. (1989) we can then estimate the extinction correction. From Schlegel et al. (1998) the 2MASS colours can be similarly corrected for extinction by using:

$$A_J = (0.902) * E(B - V) \tag{2.3}$$

$$A_H = (0.576) * E(B - V) \tag{2.4}$$

$$A_K = (0.367) * E(B - V) \tag{2.5}$$

where A_J, A_H, and A_K are the extinctions in J, H, and K respectively[3]. Mateo (1998) previously measured a reddening of about $E(B - V) = 0.15 \pm 0.03$ toward the core of Sgr. This agrees with our $E(B - V) \sim 0.15$ for stars within 20 degrees of the centre of the Sagittarius Dwarf.[4]

First we use the translation to Bessell-Brett colours and then perform the extinction correction. Using the 2MASS translation, the Bessell-Brett colours are then:

$$(H - K)_{bb} = ((H - K_o) - 0.034)/0.971 \tag{2.6}$$

$$(J - H)_{bb} = ((J - H_o) + 0.049)/0.990 \tag{2.7}$$

$$K_{bb} = K_{2MASS} + 0.039 - (0.001)(J - K)_{bb} \tag{2.8}$$

To turn K_{bb} into an extinction-corrected magnitude, we then combine Equation 2.5 and Equation 2.8:

$$K_{bbe} = K_{bb} - A_k \tag{2.9}$$

We apply the distance modulus formula:

$$(m - M) = 5 * \log \frac{r}{10pc} \tag{2.10}$$

$$M_k = K_{bbe} - (m - M) \tag{2.11}$$

[3]The Schlegel dust map is queried via the python module '**astropysics.obstools.get_SFD_dust**' for each star position to give the $E(B - V)$ values for the star in question

[4]Our extinctions are calculated for individual stars. Following McConnachie (2012) we note that, while the Schlegel et al. (1998) maps are accurate to 16% for nearby galaxies, the resulting values are not observed directly but rather have a most likely value assigned to them; this means that smaller scale variations on the scale of our core observations will not be traced.

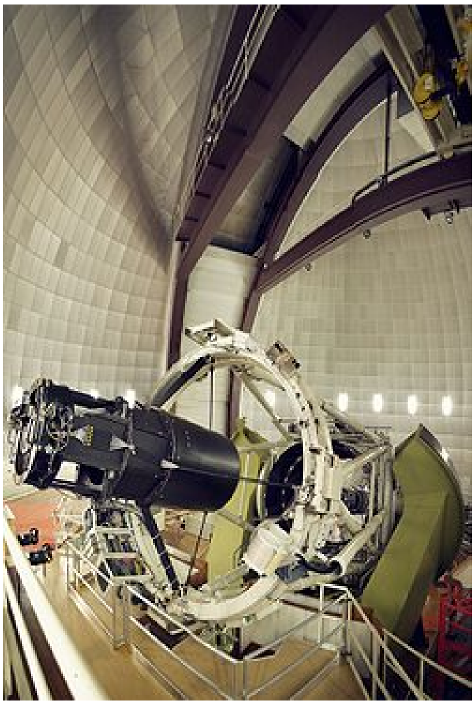

Figure 2.4: The Anglo-Australian Telescope (AAT), mounted with the AAOmega instrument used to obtain the spectra for this thesis. The telescope is operated by the Australian Astronomical Observatory (AAO) at Siding Spring Observatory, Coonabarabran NSW.

where (m-M) is the literature value of the distance modulus, which finally gives us our absolute magnitude, M_k.

This conversion is valid for all of our core stars and all of our calibration clusters. The distances to most objects in the stream (discussed in detail in Chapter 4) are not known, and so an absolute magnitude estimate for stream stars was not included. We note that it is possible to derive distance estimates from the stellar luminosity of the spectra and recommend that as a future expansion to this project.

2.3 The AAT and AAOmega

We used the multi-object spectrograph AAOmega (Sharp et al. 2006) on the Anglo-Australian Telescope (AAT) to observe candidate stars in the Sgr dwarf and stream. By obtaining spectra we extract velocity and metallicity information for all the stars observed. To characterise the kinematics of the Sgr dwarf and stream we will need to analyse the radial velocities of a large number of stars over the entire sky (Ural et al. 2010). These areas are divided into two degree diameter fields, matched to the field of view of the *2dF* robotic fibre positioner on the AAT (shown in Figure 2.4).

The blue and red arms of the AAOmega instrument cover the wavelength range 370nm to 880nm at low resolution and are tuneable over this entire range at higher resolutions (Spolaor 2010). Our observations use a blue arm grating at 1500V and a red grating of 1700D (corresponding to a wavelength range of 4250-6000Å in the blue and 8450-9000Å in the red). The resolutions are R$\sim$ 8000 in the blue and R$\sim$ 10000 in the red. The spectral regions covered by the instrument include the magnesium (MgI 5170) and calcium (Ca II 8500) Å triplets. The AAOmega instrument can observe approximately 360 science targets in each field (from 392 assigned fibres). Instrument uncertainties limit the errors in velocity to be less than 5 km s^{-1}.

The fields to be observed need to be set up to target likely Sgr candidate stars. We used 2MASS photometry for this purpose. Once we know which 2MASS targets are desirable, we then optimise the list of potential targets for the AAOmega instrument on the AAT. The *2dF* positioning robot which feeds AAOmega is a 400 fibre instrument which can observe 392 positions within a single pointing of the two degree diameter field of view on the sky. The visibility of the object depends on the seeing, the altitude of the centre of the field above the horizon, and the proximity of the field in question to the light of the moon[5]. For all observations the position of the moon is kept at least ten degrees away.

In order to observe our stars, we also need some fibres pointed at guide objects to keep the light directed down the fibres, and the telescope on course. These eight guide fibres are referred to as '*fiducials*'. We additionally need to have several fibres pointed at sky positions, or locations where no luminous object is thought to be, in order to do an optimised subtraction of the sky background for our data. These '*sky*' fibres are found via searching the input catalog for unoccupied positions. The algorithm to search for empty places in the sky was written and implemented by project collaborator

[5]All visibility charts are calculated from: `http://catserver.ing.iac.es/staralt/`

Mike Irwin[6] for all Sagittarius data using the 2MASS input catalog.

The '*configure*' routine, developed by the AAO, attempts to place fibres optimally, based on the set of object, fiducial, and sky positions that are given by the user. To be able to select the required number of sky positions and fiducials, it is a good idea to give the program more than 300 listed positions. Occasionally some fibres may break or have conflicting crossing angles and the distribution of stars must fit within the abilities of the instrument to place fibres, which might make some objects unobservable. If the fibre is unable to be placed by the routine it is '*parked*' on the instrument and returns no data.

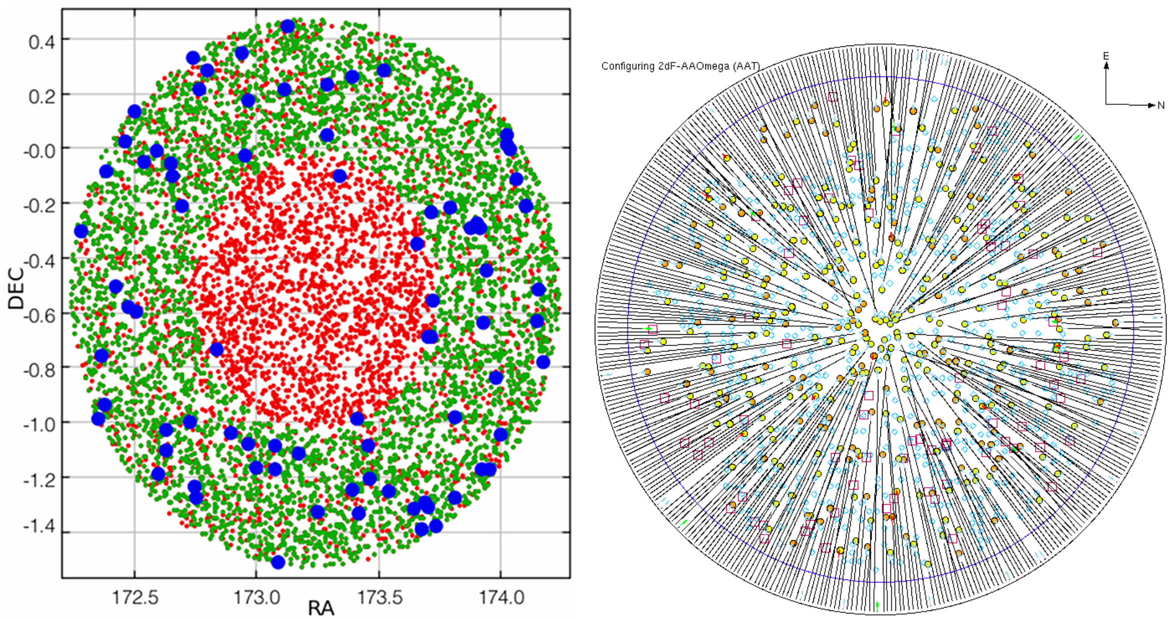

Figure 2.5: On the left, an example field object assignment. Potential target positions are shown in red, potential fiducials in green and selected (low proper motion) fiducials in blue. The *configure* window for this field is shown on the right.

The fibres can be positioned to within 30 arc-seconds of each other, but are limited in the angle they can cross on the instrument. For densely populated areas this can lead to problems selecting objects in the centre if observing throughout the two degree field of view. For fields that are even moderately crowded, it is worthwhile to limit the fiducial stars to an outer annulus as shown in Figure 2.5. When selecting stars,

[6] M. Irwin, private communication

a priority is assigned in *configure* that determines which stars the program will try to fit first. Since fiducial (guide) stars must be found in order to observe at all, it is recommended to set them to the highest priority. The guide stars must be within a tight magnitude range, approximately $14 < V < 14.5$ mag during dark skies (although up to 12th magnitude is permissible during a bright moon). It is recommended that these be low proper motion objects. Our selection was carried out by comparing 2MASS objects that had been observed in the *ppmxl* catalog to match the lowest proper motion objects with the fields we wanted to observe. To limit the amount of proper motion present in any fiducial we require that:

$$25 \text{ mas/yr} > \sqrt{(\text{pmRA})^2 + (\text{pmDEC})^2} \tag{2.12}$$

where pmRA and pmDEC are the *ppmxl* proper motions of a star in RA and DEC respectively. This limits the motion of any fiducial star to less than 25 mas per year. As all of our fields had widely distributed target stars, we generally had both targets and sky positions covering the entire two degree area available. Figure 2.5 shows an example of the resulting AAOmega *configure* field.

The first six Core 1 pointings for this project were taken during May-June 2010 and 9 pointings in the region of Sgr were targeted. We successfully observed pointings F1, F2, F4, F5, F6, F8 listed in Table 2.2.

When planning our observations we mapped a grid pattern of pointings for the core region as shown in the zoomed in box of Figure 2.1 (the core region is discussed in greater detail later in Chapter 3). We initially observed only the six magenta Core 1 pointings in Figure 2.1 and then expanded our project. We expanded to cover the central region 'R01', and then later to cover the stream region, giving all of the pointings shown in the Figure 2.1. The stream pointings were obtained through collaboration with Rodrigo Ibata[7], although all data were reduced and analysed for this thesis.

During our second observing run covering R01, we were able to view the majority of the block of core observations shown in Figure 2.1. The final fields of R01 we achieved with a service run. The single offset field shows the closest observing field incorporated

[7] R. Ibata, private communication

from Rodrigo Ibata's observations of the Sgr stream. These runs were observed in the same way as our own core runs. By combining the datasets we were able to generate the comprehensive mapping shown in Figure 2.1. Since the first data reduction was carried out on the Core 1 fields we will concentrate on those spectra for the discussion of the data reduction process.

We used our six Core 1 (magenta) pointings to test the rotating core hypothesis, and to analyse their metallicity and velocity distributions. To perform the basic reduction of the data, we first needed to extract the 1-dimensional spectra from the multi-object image produced by the AAOmega instrument. The initial reduction was achieved with the *2dfdr* data reduction program of the Australian Astronomical Observatory (AAO) (Heald 2007).[8]

2.4 Reduction of the data: *2dfdr* and IRAF

We set out to measure metallicities of stars in the Sgr dwarf with the aim of studying its overall metallicity distribution function (MDF) and finding if that MDF changes over the body of the Sgr dwarf (see Chapter 3) as well as the Sgr stream (see Chapter 4). Our wavelength regions include both the magnesium and calcium lines. In this work we use the calcium region alone for metallicity and velocity determination due to partial contamination of the magnesium triplet region by titanium oxide bands. Different errors for different measured parameters (the velocity and the metallicity) as well as different physical scales of examination (the core versus the stream) have led us to consider different subsets of the data in this thesis. The spatial subsets correspond to several regions of the Sgr dwarf. These are the 'Core 1' set, the 'R01' set, and a 'stream' set, defined as:

- Core 1: The initial 6 pointings around the core of Sgr, referred to as 'Core 1'. These stars are used in this chapter to illustrate the data reduction process and are discussed in detail in Chapter 3.

[8]We used the 32 bit mac osx release, and the standard aaomega.idx system to reduce all data.

- R01: A broader core region, as shown in Figure 2.1, including 23 pointings around the centre of the Sgr dwarf (Core 1 plus all follow-up observations). We designate this region 'R01', it is discussed in detail in Chapter 3. This region is treated as a single data point when discussing the stream in Chapter 4.

- Stream: This data set includes all Sgr stream observations from Figure 2.1. R01 is the first of the 30 stream regions spanning the sky. The distribution and selection of Sgr members from the data is discussed in Chapter 4.

These three subsets encompass a total of ∼24,110 spectroscopic observations of candidates associated with the Sgr dwarf and its stream.

Depending on the selection that we make on our data, different numbers of spectra will be returned to work with. Shown in Table 2.1 we have a list of the primary groups used in this work for the Sgr dwarf and stream. The top group in the table labeled '*all*' is literally every spectrum produced by the basic reduction. As this included even observations of the sky and other non-stars (these are the *sky* and *parked* fibres respectively, discussed further in Section 2.3), to manipulate the data it makes sense to divide the data into several sub-groups. The '*npskyfid*' group is all of the stellar spectra with fiducial objects, parked fibres, and sky fibres removed from the set. These 24,110 spectra represent all of the Sgr candidate members observed for this project.

Group	all	R01	stream
all	32,000	10,695	21,305
npskyfid	24,110	9,086	15,024
$V_{err} < 5$	19,707	···	···
Rcoeff$\geq$ 15	16,926	···	···
V_{err}+Rcoeff	15,461	···	···
loggTcut	7,036	6,227	809
P1	5,619	5,513	106

TABLE 2.1: Table of groups for sorted spectra. The 'npskyfid' group excludes parked, sky and fiducial observations, the '$V_{err} < 5$' group excludes measurements with high velocity errors, the 'Rcoeff $\geq$ 15' group excludes measurements with high modified RAVE pipeline errors, the 'loggTcut' group corresponds to the M and K-giant selection cuts in Chapter 4 and the P1 group corresponds to the probability calculation in Chapter 4.

In Section 2.6 and 2.7 we will discuss the 'Rcoeff $\geq$ 15' group shown inTable 2.1 and the modified RAVE data reduction pipeline errors. The $V_{err} < 5$ group is larger than the RAVE Rcoeff $\geq$ 15 group, so we will have more measurements of velocity than metallicity in this thesis. The $V_{err} < 5$ group contains 19,707 stars with a velocity error estimated at less than 5 km s^{-1}. This error is calculated in the IRAF task *fxcor* for each individual star as discussed in Section 2.4.2 (the general measurement error was $\sim$ 7.3 km s^{-1} for all stars). In Chapter 4 we will discuss the subset '*loggTcut*', which corresponds to the spectra selected after quality cuts from RAVE and the log(g) and T_{eff} cuts outlined for the stream. The '*P1*' group corresponds to the probability selection for the stream discussed in Chapter 4.

2.4.1 First data analysis

The origin of this research was to help to test for rotation in the core of the Sagittarius dwarf galaxy (Peñarrubia et al. 2011). The initial research is outlined in Chapter 3, but we discuss the details of the data reduction here to illustrate our procedure. As an example of the data reduction procedure, we describe here the reduction of the data for the initial six core observations or pointings (the Core 1 region as discussed previously).

Using the images from the blue and red data respectively we tailor our data reduction to each arm, running the *2dfdr* program with settings optimised to the respective data properties. In both cases we set the polynomial for sky fitting to '1' (rather than the default value, which is a higher order) to provide a reasonable fit and to avoid introducing higher polynomial error effects. Additionally all data need to have a single pointing per directory, and one flat and one arc exposure per group. For observations with more than one individual flat or arc, we chose the corresponding images with the best signal-to-noise to use in the reduction. The selected files are listed in Table 2.2. These images are then imported into the *2dfdr* window, as shown in Figure 2.6.

For both red and blue data sets, it is important that the option to '*adjust continuum*

Pointing	Date	UT at start	Instrument	Instrument Mode	Optical Path	Flat	Arc
F2	2010:06:03	12:17:14	AAOmega	1500V	BLUE	03jun0013	03jun0011
"	"	"	AAOmega	1700D	RED	"	"
F2	2010:06:04	12:10:00	AAOmega	1500V	BLUE	04jun0016	04jun0019
"	"	"	AAOmega	1700D	RED	"	"
F2	2010:06:04	17:34:15	AAOmega	1500V	BLUE	04jun0022	04jun0021
"	"	"	AAOmega	1700D	RED	"	"
F4	2010:06:04	18:41:42	AAOmega	1500V	BLUE	04jun0030	04jun0029
"	"	"	AAOmega	1700D	RED	"	"
F1	2010:06:06	15:56:31	AAOmega	1500V	BLUE	06jun0028	06jun0032
"	"	"	AAOmega	1700D	RED	"	"
F5	2010:06:06	14:39:26	AAOmega	1500V	BLUE	06jun0022	06jun0026
"	"	"	AAOmega	1700D	RED	"	"
F6	2010:06:06	18:31:20	AAOmega	1500V	BLUE	06jun0040	06jun0039
"	"	"	AAOmega	1700D	RED	"	"
F8	2010:06:06	17:13:41	AAOmega	1500V	BLUE	06jun0034	06jun0033
"	"	"	AAOmega	1700D	RED	"	"

TABLE 2.2: The data files reduced for Core 1 pointings F1,F2,F4,F5,F6 and F8.

levels' is turned off as this can cause problems when extracting our (relatively bright) objects. As shown in Figure 2.6 the control panel has several customisable options in *2dfdr*. One can select the flux weighting for brighter or dimmer sources, and include sky and bias subtraction to name a few. We specified a flux weighting, continuum subtraction, sky subtraction, and, in the case of the blue data, we also used a bias subtraction frame. Sometimes the arc solutions in blue can fail in corner areas of the CCD, so for this routine to extract the spectra it must have a valid solution throughout the entire region. Visual inspection of the results showed that the settings given here resolved this issue. The electronics involved in the blue arm of the spectrograph together with the low counts from our object in the blue mean that we require a bias frame for the blue arm reduction (note that the red arm reduction is optimal without bias subtraction, so no average bias frame was used for that data).

Once an averaged bias is created, the bias subtraction is performed inside the *2dfdr* program. The Table 2.2 Core 1 pointings F1, F5, F6 and F8 were all observed on June 6th with optimal results but F2 was observed 3 times, on the 4th and the 3rd, and out of those the observations on the 4th were under cloudier conditions. The bias frames for these observations were taken from a block of observations on the 6th of

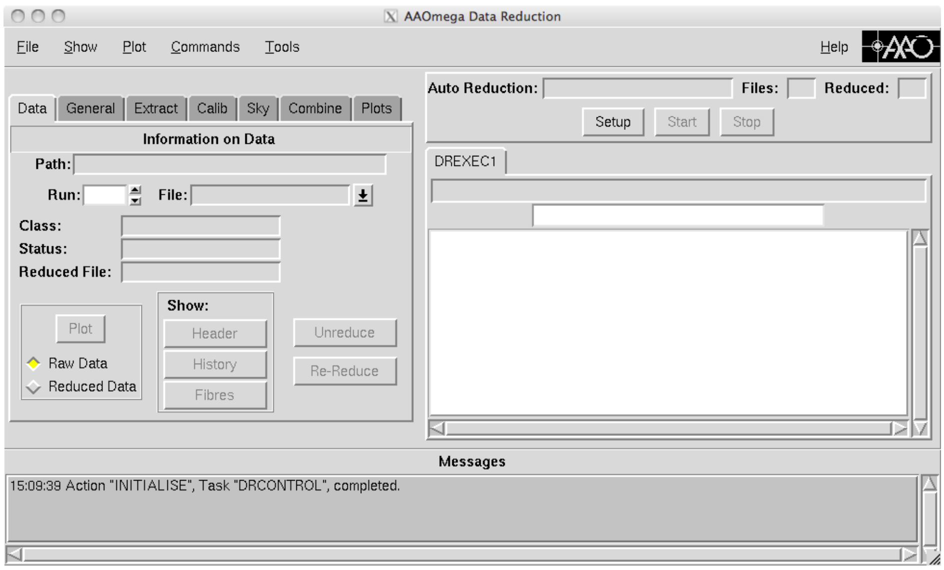

Figure 2.6: The *2dfdr* data reduction window.

June 2010 (near the end of the run). Pointing F4 was observed on the 4th and there was unfortunately not time to get observations of all the remaining fields at that time. The full set of all runs are discussed in Chapter 3 and 4.

A full reduction of red and blue data both with and without sky subtraction was performed. Over several night sky spectral emission lines in both the red and blue arm the ratio of flux after sky subtraction (F_a) to flux before sky subtraction (F_b) is approximately $F_a/F_b \sim 0.1 \pm 0.07$. For the faintest lines this ratio is even better. For example, lines starting at an integrated flux of ~ 500 counts$\times$Å generally do not have a measurable component after sky subtraction. We conclude that the *2dfdr* sky subtraction is able to remove sky lines to within 10% for all sky lines observed and we use the sky-subtracted version for all of our data. The full wavelength range and reduction for a typical Sagittarius dwarf member spectrum is shown in Appendix A.2.

2.4.2 Initial velocities

We used the IRAF[9] task *fxcor* to extract radial velocity information for all of our objects. For our initial six fields we expect the velocities obtained to lie near that predicted for the centre of the Sgr dwarf ($V_h = 139.4 \pm 0.6$ km s^{-1}; Bellazzini et al. 2008). To determine the radial velocities we started with a basic template fit to the calcium triplet lines in our red arm spectrum.

Template fitting

The velocities were measured automatically by use of template spectrum fitted to the calcium triplet. This template file[10] was produced with a simple Gaussian representation of the calcium triplet lines in air. We then compared the template to our spectrum with the IRAF task *fxcor*.

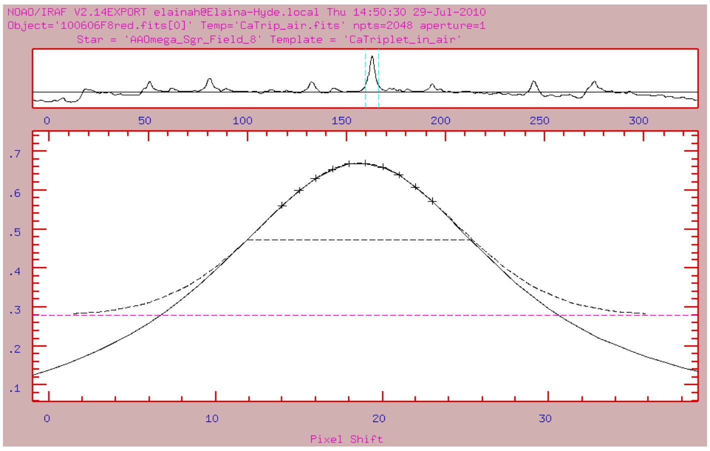

FIGURE 2.7: Image of the cross correlation window from the IRAF *fxcor* reduction.

In *fxcor* we used a Gaussian to find the centre of the correlation peak shown in Figure 2.7. This is a Fourier cross-correlation on the list of input spectra with relation

[9]The IRAF software package is distributed by the National Optical Astronomy Observatories, which are operated by the Association of Universities for Research in Astronomy, Inc., under cooperative agreement with the National Science Foundation.

[10]The template used was created by Andreas Koch (private communication)

Pointing	UT date	UT at start	RA	DEC	V_{helio} (km/s)
F2	2010:06:03	12:17:14	18:47:30.84	-29:52:7.27	13.67
F2	2010:06:04	12:10:00	18:47:30.68	-29:52:07.48	13.24
F2	2010:06:04	17:34:15	18:47:30.75	-29:52:15.01	12.82
F4	2010:06:04	18:41:42	19:02:46.38	-31:04:02.08	14.18
F1	2010:06:06	15:56:31	18:40:02.35	-29:14:00.16	11.28
F5	2010:06:06	14:39:26	19:10:31.87	-31:37:19.68	14.20
F6	2010:06:06	18:31:20	18:52:16:13	-32:07:27.37	12.24
F8	2010:06:06	17:13:41	19:00:04.05	-32:43:06.54	12.96

Table 2.3: Heliocentric corrections from the year, UT date, RA and DEC positions for our six original Core 1 fields.

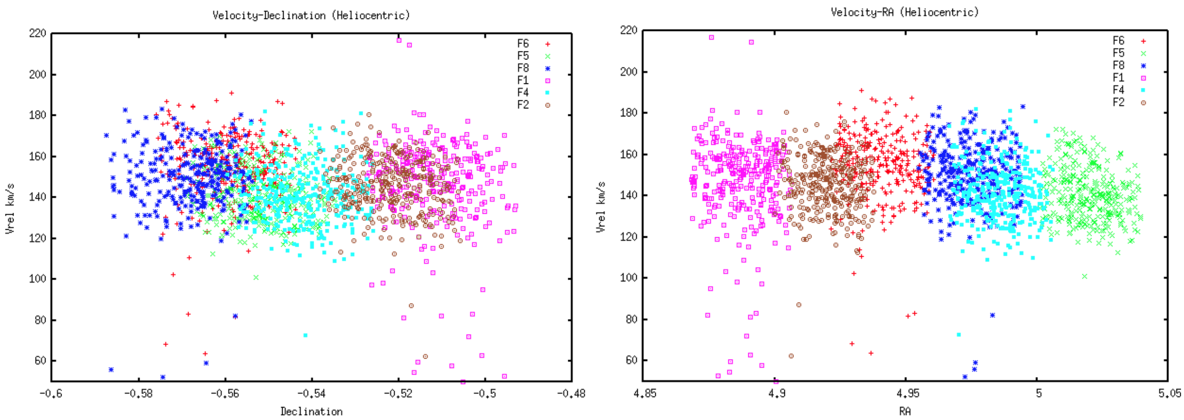

Figure 2.8: Heliocentric radial velocity versus Declination (left) and Right Ascension (right) for Core 1 observations. The heliocentric velocity corrections for each pointing are shown in Table 2.3.

to the template. It measures the similarity of the two waveforms as a function of an offset applied to one of them and returns the relative velocity between the object and template spectra. Since the template is already in the 'rest-frame' we now have our velocity values. These velocity values have an associated error and this is computed based on the fitted peak height and the antisymmetric noise, as described in Tonry & Davis (1979). This associated uncertainty can be used as an extra criterion for individual measurement quality.

The heliocentric velocity was calculated within IRAF's *rvcorrect* task for each day and each pointing observed. A subset of these calculations for our first set of six pointings is shown in Table 2.3.

Due to the fact that most of our objects have very weak magnesium triplet lines

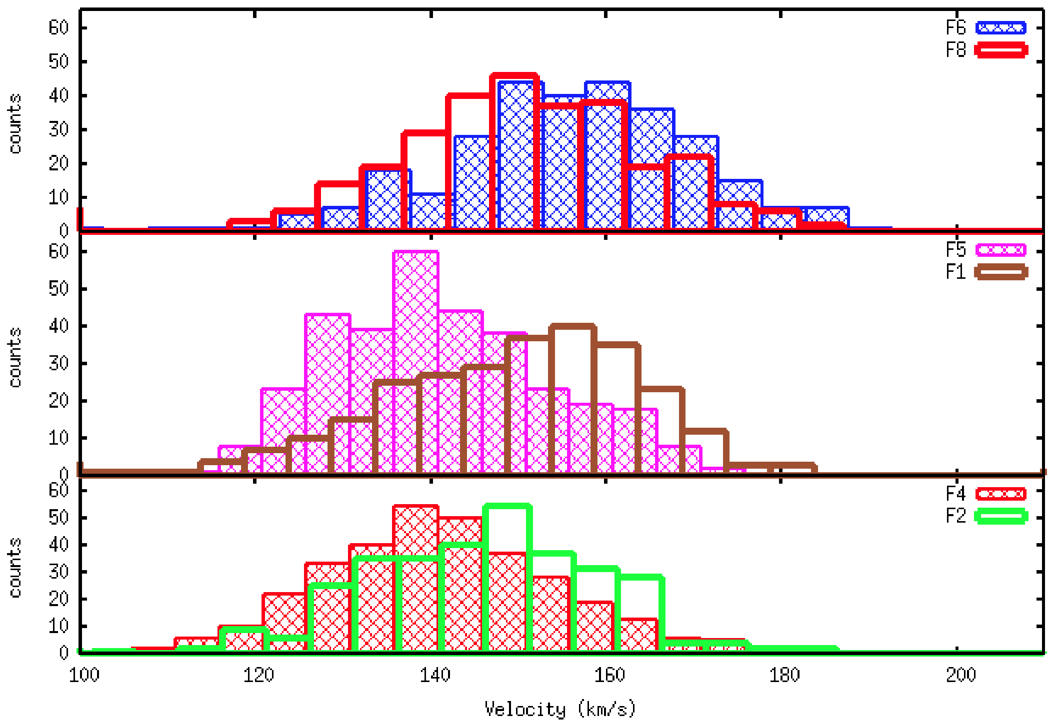

FIGURE 2.9: Histogram of velocity distribution for pointings in Table 2.3. In the case of F2 the multiple pointings are combined to form one F1 histogram. In all cases the shift in velocity corresponds to the effect due to the Sgr dwarf core orbiting the Milky Way.

we did not repeat the reduction and measurement of velocities using the magnesium triplet. It was attempted, but as the lines were measurable in less than 40% of our spectra, we restrict ourselves to the velocity measurements from the calcium triplet lines. The velocity results are shown in Figure 2.8. We see that the stars form a group in velocity space (near 139 km s^{-1}) in both Declination and Right Ascension, respectively. The majority of selected stars appear to be travelling at a similar velocity, confirming their likely membership in the Sgr dwarf.

To generate a histogram of the data in different pointings we take our initial set of 6 pointings observed and use the IRAF task *phist* with a bin size of approximately 5 km s^{-1}. Comparing different pointings, we can see in Figure 2.9 that there does appear to be a difference in the velocity peak between fields. This is what we would expect due to the fact that the fields are part of an extended core in orbit around the Milky Way. This local gradient will have to be taken into account when considering internal velocity differences in the core. The gradient for the full R01 region is investigated in more detail in Chapter 3.

The uncertainties for velocity measurements are known to be on the order of 3 to 5 km s^{-1} due to the spectral resolution of the 1700D AAOmega grating. To check the robustness of the velocities, and obtain a more precise error estimate, we compare the velocities of 21 different stars which were observed 3-4 times. We adopt the average error $\sigma/n \simeq 2.7$ km s^{-1} as the error for the velocity measurements, $\mathrm{V_{err}} = 2.7$ km s^{-1}. We additionally have velocity error measurements as predicted by our IRAF reduction and the RAVE reduction techniques which are used to limit individual measurement error values. The $\mathrm{V_{err}} = 2.7$ km s^{-1} value is a direct comparison between our measurements and gives us a generic error which we use for comparison with models in Chapter 4.

$\mathbf{V_{GSR}}$ calculation

The heliocentric rest frame takes the barycentre (the centre of mass) of the Solar System as its centre point. We can also use a Local Standard of Rest (LSR) frame, in which the peculiar motion of the Sun with respect to the rotation of the Galaxy is taken into account. As a further coordinate transform we can also translate into a Galactic Standard of Rest (GSR) frame where the rotation of our Milky Way (at 220 km s^{-1}) is accounted for. We will primarily use the GSR or heliocentric frames for velocities in this thesis. Starting with the previously discussed heliocentric velocities, we transform the spatial coordinates into Galactic longitude and latitude, (l, b) and convert the radial velocity into a GSR velocity ($\mathrm{V_{GSR}}$).

The conversion to $\mathrm{V_{GSR}}$ can be performed several ways. One commonly used conversion comes from Braun & Burton (1999). We adopt the LSR velocity at the Sun as 220 km s^{-1} (Kerr & Lynden-Bell 1986) and account for peculiar velocity by using 16.5 km s^{-1} toward $lp = 53°$, $bp = 25°$ (Mihalas & Binney 1981). We then convert to $\mathrm{V_{GSR}}$ using:

$$\mathrm{V_{GSR1}} = \mathrm{V_{hel}} + 220\sin(\mathrm{l})\cos(\mathrm{b}) + 16.5 \times [\sin(\mathrm{b})\sin(\mathrm{bp}) + \cos(\mathrm{b})\cos(\mathrm{bp})\cos(\mathrm{l}-\mathrm{lb})] \tag{2.13}$$

as shown in Casey et al. (2012a). However we can also simply just use:

$$\mathrm{V_{GSR2}} = \mathrm{V_{hel}} + 9\cos(\mathrm{l})\cos(\mathrm{b}) + 232\sin(\mathrm{l})\cos(\mathrm{b}) + 7\sin(\mathrm{b}) \tag{2.14}$$

to find $\mathrm{V_{GSR}}$ (Paturel et al. 1997). The two conversions $\mathrm{V_{GSR1}}$ and $\mathrm{V_{GSR2}}$ have a mean difference of 0.0012 km s^{-1} for our data. As this is much smaller than our velocity errors we can treat them as equivalent. We adopt the $\mathrm{V_{GSR2}}$ version found in Equation 2.14 for calculating Sgr velocity values in the remainder of this thesis.

2.5 Initial metallicities

An initial metallicity estimate was calculated via the calcium triplet lines; the equivalent widths of the lines were measured and combined with the V magnitudes as estimated from 2MASS data (see Section 2.2.2). Our process is based on the approach of Koch et al. (2008b) to obtain estimates of [Fe/H] metallicity using the calibration of Rutledge et al. (1997a,b).[11]

The range of metallicities we obtain from this method is discussed in the following sections. We will show agreement with the average of about [Fe/H] ~ -0.4 to -0.5 dex that we expect for the Sagittarius dwarf M and K-giants that we have observed but the Rutledge et al. (1997a,b) calibration is known to be less accurate at metallicities outside of the range from $-2.5 <$[Fe/H]< -0.5 Battaglia et al. (2008).

With our wide distribution of metallicities in Sgr we expect to find some stars with a metal rich ([Fe/H]$\geq$ 0.0 dex) population. Many metallicity calibrations of the calcium triplet range up to +0.0 to +0.2 dex (Rutledge et al. 1997b,a; Olszewski et al. 1991) although most note that it is optimal for metallicities at or below -0.5 dex (Armandroff & Da Costa 1991; Suntzeff et al. 1992). For metal-rich stars (Jones et al. 1984) or young stars (Bica & Alloin 1987) a strong correlation with log(g) gravities

[11]To measure these interactively we use the calcium triplet template, the fortran code '`ew_ascii.f`' (compiled re: private correspondence with A. Koch) and an input list of acceptable values for the lines in question. After we split the multi-object spectra into 1-dimensional files, this returns us equivalent width estimates for the calcium lines of every spectrum in every image that we reduce.

and the calcium triplet was found but the metallicity had a preferentially weaker correspondence. The equivalent width dependance of the calcium triplet with respect to log(g) can become nonlinear above metallicities of [Ca/H]$= -0.3$ Diaz et al. (1989). In particular it is noted by Jorgensen et al. (1992); Cole et al. (2000) that this effect becomes very important for intermediate age and young stars. Fortunately the Sgr dwarf has an older (10-12 Gyr Sarajedini & Layden (1995); Mateo et al. (1995, 1996), et. al.) population than the 1-3 Gyr stars surveyed by Cole et al. (2000) and should be minimally affected. Furthermore, it was shown that, within the primary range we are interested in, metallicity is the controlling parameter in the equivalent widths for the calcium triplet (Armandroff & Zinn 1988). In particular we expect that in a mixed dwarf spheroidal population, such as the Sagittarius dwarf, we should roughly be able to apply this calibration as the sensitivity to age is likely to be small.

Although we do not expect a large number of extremely metal poor stars, it is possible that some of our objects will fall below a metallicity of [Fe/H]$= -2.5$ dex. In the literature both Cole et al. (2000) and Casey et al. (2012a) find that a re-calibration of the Rutledge relation is needed for low metallicity ([Fe/H]≤ -2.5) objects. From Starkenburg et al. (2010) and Starkenburg et al. (2013) we know that the calcium triplet can be used down to a value of [Fe/H]$\simeq -3.0$ to -4.0 dex. We find approximately 30 low metallicity stars in our R01 data (see Chapter 3), which while notable is only a small fraction of the over 6000 stars present. We conclude that analysis of the calcium triplet equivalent width will return valid metallicities for the bulk of our stars and look for a method that can use it with high accuracy and in as automated a fashion as possible.

2.6 RAVE pipeline

We perform a full analysis of our spectra with a modified version of the Radial Velocity Experiment (RAVE) (Siebert et al. 2011; Zwitter et al. 2008; Steinmetz et al. 2006) pipeline[12]. This analysis provides values for log(g), $T_{\rm eff}$, [m/H] (total metallicity) and

[12] A. Siebert, private communication.

[α/Fe] abundances. The RAVE pipeline relies on a library of synthetic spectra to fit sky-subtracted data in a wavelength range of $8448.77 < \lambda < 8746.84$ Å (the red arm in our spectra). Once an input heliocentric correction is given for the observation in question the RAVE pipeline derives a temperature estimate and then iteratively determines the best spectral template match. The weights of the best match are determined by a χ^2 routine described in Zwitter et al. (2008). The resolution of the template library means that the stellar parameter estimates are incremented and conservative estimates of errors for a spectrum with an average signal-to-noise ratio (S/N $\sim$ 40) are 400 K in temperature, 0.5 dex in gravity, and 0.2 dex in metallicity (Zwitter et al. 2008). We note that our RAVE pipeline reduction is realised using a modified 'DR3' version. The template library in this version does not fit to carbon stars, so although they are present in our data, they are excluded from consideration here.

As mentioned in Section 2.4, our initial results return a total of 24,110 spectra produced by the *2dfdr* reduction (see Table 2.1). Of these, the number of stars returned with a velocity error estimated at less than 5 km s^{-1} is greater than the number returned with low RAVE errors. When we use the modified RAVE results (for any measurement of [m/H]) we must consider the RAVE error parameters; in particular the measurement accuracy is constrained by the 'R coefficient', or Rcoeff (used for stream star selection in Section 4.1). We require that Rcoeff ≥ 15, which returns the 16,926 stars discussed in Section 2.4. Of these we have 15,461 which are also low velocity error objects ($\sigma_{rv} \leq 5$ km s^{-1}). Depending on whether we are working with velocity and/or metallicity a different number of low error measurements will be present.

When initially examining our data plus the RAVE results for the stars, it was evident that two possibilities were present for metallicity calibration: [Fe/H] estimates from the calcium triplet measurement, and the [m/H] of RAVE. Since our data are not RAVE data and we are using a modified RAVE pipeline we opted to use calibration star clusters to achieve a more independent estimate of how our metallicity measurements corresponded to other work and what type of calibration would be best suited to our purposes. In the following sections we will compare our initial measurements to the results obtained with the modified RAVE pipeline.

2.7 The reduction of calibration clusters

To investigate whether we want to use our measured equivalent widths or the modified RAVE pipeline metallicity results we will test how both of these methods perform when given data from known star clusters. To test the RAVE [m/H] values and the equivalent widths (EW) in a robust way we can use star clusters which have a well-determined metallicity in the literature. The [m/H] values from RAVE are tested against several standard star clusters: 47 Tucanae, NGC 288, M30, M2, Melotte 66, and NGC 1904. These clusters were observed with the AAT using the same instrument settings as the main program. These standard star clusters were observed by a collaborator for a unrelated research project; we obtained the raw data from the AAT Data Archive[13] and all instrument settings for these observations were confirmed through private communication (S. Keller, email correspondence, 2011). We reduced these star clusters in the same way as our primary science data, and we ran the resulting spectra through the modified RAVE pipeline. The literature metallicities of these clusters (shown in the $[Fe/H]_{lit}$ column of Table 2.4) allow us to compare the metallicities we measure to those compiled by Harris (1996) and the WEBDA online database[14].

The method we chose to use to assess our results for the calibration clusters was to inspect the calibration of the absolute K magnitude with the metallicity [m/H] as measured by RAVE, and with several possible combinations of the equivalent widths of the individual calcium triplet lines. It was noted by Olszewski et al. (1991) that the metallicity sensitivity of the calcium triplet line index is improved by plotting it as a function of the absolute magnitude. By using the absolute magnitude we additionally minimize any error on the derived metallicities due to uncertainties in the horizontal branch position (although for Sgr these should be small, for some of the comparison objects we use it is more important). We therefore investigate a wide range of metallicity estimates with respect to an absolute magnitude, in our case the absolute K band magnitude. This method is similar but not identical to those outlined in the literature previously (Pont et al. 2004; Carrera et al. 2007; Starkenburg et al.

[13] http://site.aao.gov.au/arc-bin/wdb/aat_database/observation_log/make

[14] http://www.univie.ac.at/webda//webda.html

2010, 2013); and others.

To see if the RAVE [m/H] value is an accurate proxy for metallicity we compare its value to several combinations of equivalent width. To estimate metallicity from the calcium triplet one can use the equivalent widths of the first, first and second, or first, second and third, lines as part of the calibration. That is, EW1, or EW1 plus EW2, or EW1 plus EW2 plus EW3, where EW3 is the equivalent width of the first calcium triplet line at 8498 Å and likewise EW2 and EW1 correspond to the calcium lines at 8542 and 8662 Å, respectively. These values are then subjected to a linear fit.

To carry out this comparison we first need to define an M_K, or absolute K magnitude. Following Section 2.2.2, to estimate the absolute K magnitude we first translate to Bessell-Brett colours[15] and then use the extinction corrected Bessell-Brett K magnitude plus the defined distance modulus for the cluster, that is:

$$M_{Kcl} = Kbb(a)_{cl} - (m - M)_{cl} \tag{2.15}$$

where $Kbb(a)_{cl}$ is the extinction-corrected Kbb magnitude of the cluster from above. The absolute magnitude is then $M_K = Kbbe - (m - M)$ as shown in Equation 2.11 where the distance modulus is $(m - M)$ (Harris 1996).

The fits for all clusters using RAVE [m/H] and our measured EW1, EW12, EW123 are shown in Figure 2.10. These four plots clearly show a linear trend in metallicity but there is some variation in the slopes of the lines, particularly in EW12 for NGC 1904 and M2 (which both have metallicity of about -1.6).

Using a combination of the equivalent widths of calcium triplet lines in Figure 2.10 we see that both EW12, or EW123 show a range of slopes. Ideally a perfect calibration would have a set of parallel lines with the same slope (fit). None of our line combinations in Figure 2.10 show completely parallel lines but the calibration appears quite flat for the RAVE [m/H] values. Historically the two equivalent widths at 8542 and 8662 Å have been used to calibrate the index for the calcium triplet (Armandroff & Da

[15]Schlegel et al. (1998) use the UKIRT photometric system and so some extra conversion must be carried out. The 2MASS extinction correction may be affected so to avoid ambiguity we do not use the 2MASS correction but rather the Bessell-Brett values.

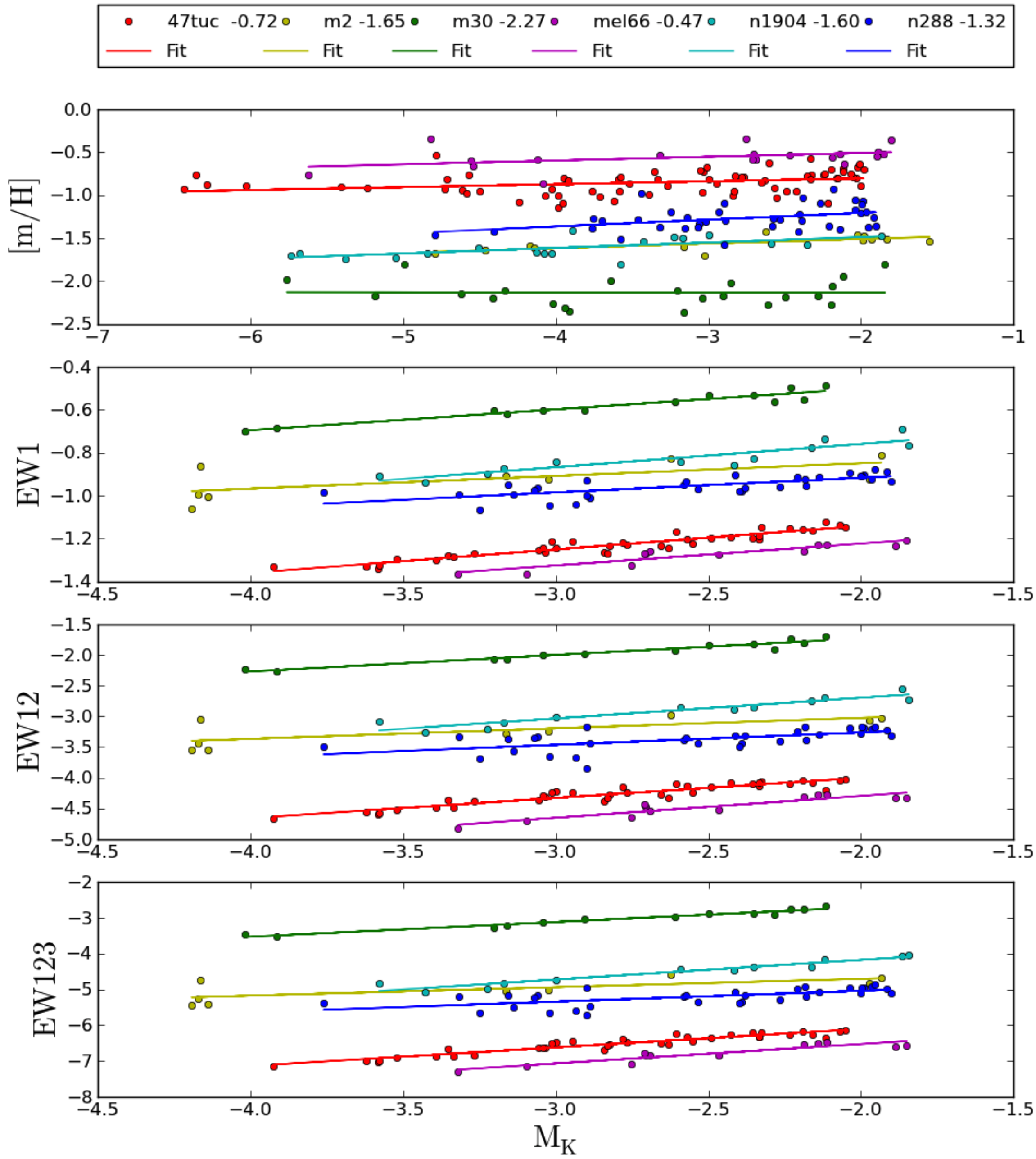

Figure 2.10: Calibration of metallicity [m/H] from RAVE (top) and equivalent line widths (EW1, EW12, and EW123) versus absolute K magnitude, M_K.

Costa 1991). More recently it was used by Starkenburg et al. (2010) and Starkenburg et al. (2013) to show a valid calibration down to low ($\simeq -4$ dex) metallicities. This corresponds to our EW12 calibration in Figure 2.10 and although it does show similar slopes the RAVE [m/H] calibration is the only one to correctly calibrate the M2 cluster and NGC 1904. In the top plot of Figure 2.10 the two lines are directly on top of each other.

The RAVE [m/H] values behave quite well for the metallicity range given by our standard clusters, better than the historical EW12 line combination and better than either EW1 or EW123. We choose to use RAVE for the rest of this thesis and for consistency we will not use any of the EW values beyond this section of the thesis. We note that because we have fewer valid measurements of the third line equivalent width, our data set is slightly more restricted in metallicity space, i.e., we have valid metallicities for fewer stars. The RAVE [m/H] values do appear to be an acceptable proxy for metallicity; we investigate this [m/H] parameter further in the next section.

2.8 Comparisons of RAVE metallicities to the literature

Each of the clusters observed has a measured reference metallicity in the literature. We test how well the modified RAVE pipeline reproduces the literature results for each cluster. The equivalent widths EW1, EW12, EW123 from Figure 2.10 show a correlation with metallicity, but the fit (slope of the line) varies between calibration clusters. This means variation in fitting across the metallicity range spanned by the clusters. The relatively low variation in the RAVE [m/H] values led us to choose it as our proxy for metallicity. By using [m/H] we also have the advantage of taking the other parameters (log(g) and $\mathrm{T_{eff}}$ for example) calculated by the RAVE pipeline. We additionally check the [m/H] results from RAVE against a few notable calibrations.

We can calibrate [m/H] using existing RAVE literature. It has been noted in RAVE documentation that the best calibration for metallicity is given by combining the [m/H] and [α/Fe] values. From Siebert et al. (2011):

$$\begin{aligned}[\mathrm{M/H}] = \mathrm{c_o} + \mathrm{c_1} * [\mathrm{m/H}] + \mathrm{c_2} * [\alpha/\mathrm{Fe}] + \\ \mathrm{c_3} * \frac{\mathrm{T_{eff}}}{5040} + \mathrm{c_4} * \log \mathrm{g} + \mathrm{c_5} * \mathrm{STN}\end{aligned} \tag{2.16}$$

where the $\mathrm{c_o}$, $\mathrm{c_1}$, $\mathrm{c_2}$, $\mathrm{c_3}$, and $\mathrm{c_4}$ parameters are used to fit the data. Following the latest

RAVE recommendations, we discard the log g and signal-to-noise (STN) parameters.

The best total metal content is given by the parameters in Table 7 from RAVE DR3 (Siebert et al. 2011). We examine three calibration cases, starting with the calibration based on a full sample, which gives:

$$\begin{aligned} c_o &= 0.578 \pm 0.098 \\ c_1 &= 1.095 \pm 0.022 \\ c_2 &= 1.246 \pm 0.143 \\ c_3 &= -0.520 \pm 0.089 \end{aligned} \tag{2.17}$$

for the above Equation 2.16. This is listed as $[M/H]_1$, our first calibration.

The calibration of Equation 2.16 for giant stars is given by:

$$\begin{aligned} c_o &= 0.763 \pm 0.197 \\ c_1 &= 1.094 \pm 0.027 \\ c_2 &= 1.210 \pm 0.193 \\ c_3 &= -0.711 \pm 0.207 \end{aligned} \tag{2.18}$$

where this is listed as $[M/H]_2$, our second calibration. Our third option is to use the raw RAVE calculated value of [m/H] with no adjustments. These three options for metallicity are tested against the clusters mentioned previously (47 Tucanae, NGC 288, M30, M2, Melotte 66, and NGC 1904).

For the first and second calibrations, the difference between the median metallicity per cluster is less than 0.20 dex (see Table 2.4) whether we use the general calibration based on a full sample, $[M/H]_1$, or the specific calibration for giant stars, $[M/H]_2$. From Figure 2.11 we see that the top and middle plots (for $[M/H]_1$ and $[M/H]_2$) are quite similar. The whisker distribution shown gives the median value as the red line in each box and that median is listed as $[M/H]_{1med}$ and $[M/H]_{2med}$ in Table 2.4.

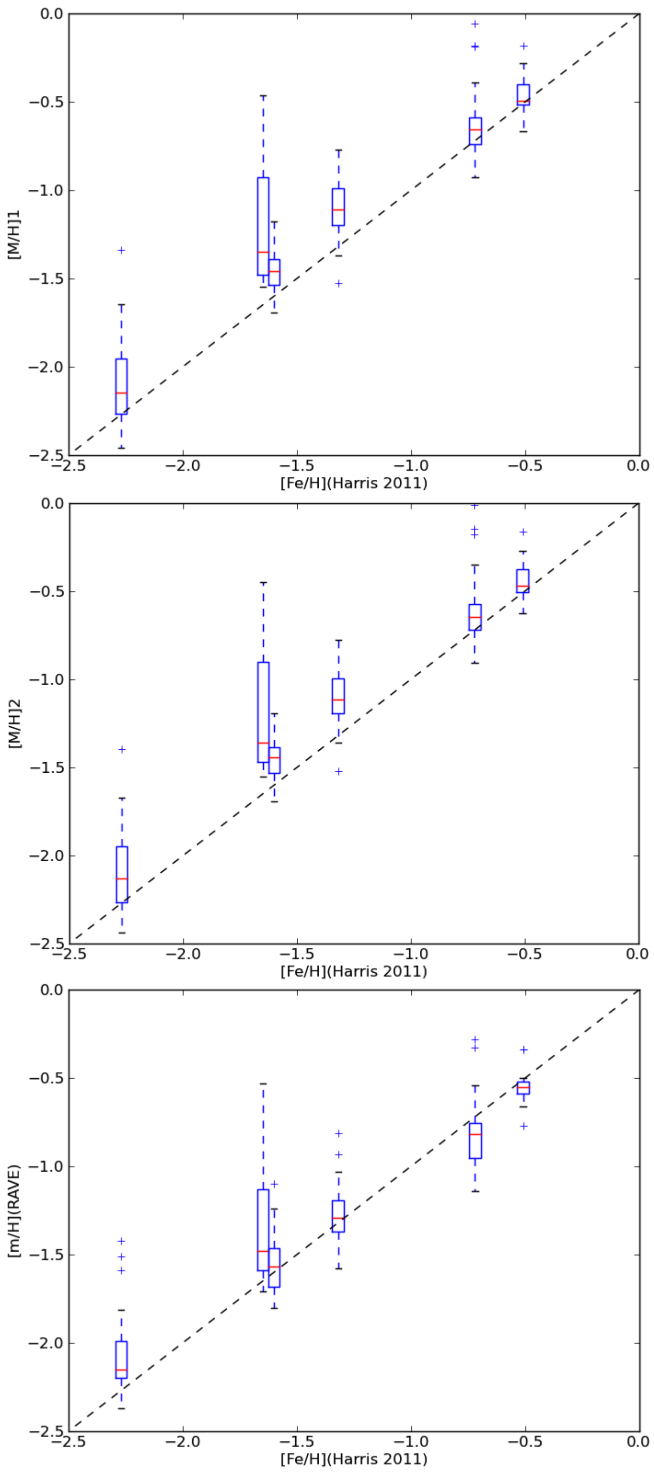

FIGURE 2.11: The $[M/H]_1$, $[M/H]_2$ and the [m/H] metallicity calibrations using the six reference calibration clusters. The black dashed line shows a one to one correspondence. Each point corresponds to one of the clusters given in Table 2.4. The red line is the median for that cluster, the 25th percentile is given by the upper edge of the box, the 75th percentile is given by the lower edge of the box and the maximum and minimum are at the ends of the whiskers.

Cluster	Num	Center		wt	$[Fe/H]_{lit}$	$[M/H]_{1med}$	$[M/H]_{2med}$	$[m/H]_{med}$	Δ_m
		RA	DEC		dex	dex	dex	dex	dex
47 Tucanae	67	00:24:05.67	-72:04:52.6	10	-0.72	-0.66	-0.65	-0.82	0.10
NGC 288	39	00:52:45.24	-26:34:57.4	3	-1.32	-1.11	-1.11	-1.29	0.03
M 30	25	21:40:22.12	-23:10:47.5	4	-2.27	-2.15	-2.13	-2.15	0.12
M 2	17	21:33:27.02	-00:49:23.7	5	-1.65	-1.35	-1.36	-1.48	0.17
Melotte 66	17	07:26:23	-47:40:00	-	-0.51 ± 0.11*	-0.49	-0.47	-0.55	0.04
NGC 1904	22	05:24:11.09	-24:31:29.0	6	-1.60	-1.46	-1.44	-1.57	0.03

* The WEBDA metallicity listed is from Friel & Janes (1993)

TABLE 2.4: Calibration clusters used from Harris Catalogue (2010 edition) (Harris 1996) for globular clusters and from WEBDA for the open cluster Melotte 66. The wt parameter gives the Harris catalogue weight of the cluster (approximately the number of independent measurements). $[Fe/H]_{lit}$ gives the literature values for the cluster and Δ_m is the difference between $[Fe/H]_{lit}$ and $[m/H]_{med}$ shown in Figure 2.11. The Num column gives the stars observed for each cluster.

Our third calibration is [m/H], the modified RAVE pipeline output with no adjustment. Although, as noted above, several calibrations for RAVE are available (Siebert et al. 2011), we find the best match to observed clusters using the standard [m/H] for RAVE as shown in Figure 2.11. The median values for these clusters as measured against reference literature values are shown in Table 2.4.

The absolute value of the difference between the calculated median shown in Figure 2.11 and the literature value of metallicity for the cluster is given by $\Delta_m = |[Fe/H]_{lit} - [m/H]_{med}|$ shown in Table 2.4. The maximum difference $\Delta_m = 0.17 \simeq 0.2$ dex. In all cases the difference $\Delta_m < 0.2$ dex. This leads us to adopt an error in [m/H] of $\pm$ 0.2 dex.

We treat [m/H] as equivalent to [Fe/H]. As the RAVE results for metallicity in this case show a nearly linear calibration (see Figure 2.11) we use the [m/H] metallicities exclusively in the remainder of this work. An example of typical M and K-giant spectra (selected from the Core 1 region discussed in more detail in Chapter 3) resulting from a RAVE analysis of Sgr stars is shown in Figure 2.12.

The RAVE metallicities are derived from fits to the red arm spectra, using the region around the calcium triplet, rather than the magnesium triplet. Due to the

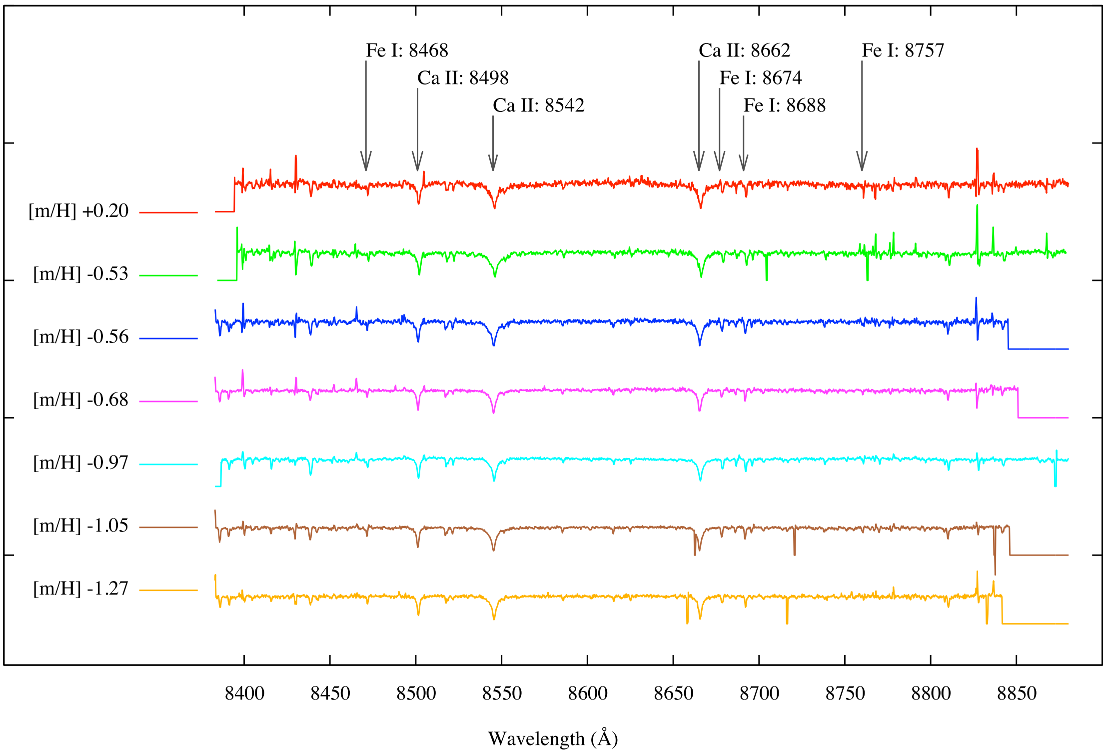

FIGURE 2.12: Several typical M and K-giant Sgr spectra from the Core 1 data set. A range of low error [m/H] metallicities from the modified RAVE pipeline is shown, each metallicity value is given a different colour.

strong contribution of titanium oxide bands and low resolution in the blue arm, over 38% of the spectra have contaminated magnesium triplet lines, hence we do not repeat the reduction and measurement of velocities using the magnesium triplet.

We note that RAVE quality cuts limit the number of objects that we are able to select, as described in Section 2.4 and 2.6. By excluding any noisy or non-optimal measurements we exclude low signal-to-noise stars or objects with unusual spectral features (all extremely metal-poor (EMP) stars, carbon stars and spectroscopic binaries) as their spectra produce high noise residuals. We are left with the typical M and K-giant spectra shown in Figure 2.12. These are fit with the spectrum synthesis routine mentioned previously, and all fits fulfil the Rcoeff $\geq$ 15 criterion.

Our combination of reduction techniques is able to provide a robust velocity estimate as well as reliable colours and metallicity. From our initial reduction we have 24,110 stellar spectra with velocity and colour information. This comes from our measurements of the calcium triplet (to obtain velocities) and the existing 2MASS photometry. To expand our parameter space we use the modified RAVE pipeline, creating a subset of data which has reliable metallicity, velocity, log(g), $T_{\rm eff}$ and a proxy estimate for $[\alpha/Fe]$ (Zwitter et al. 2008). The modified RAVE pipeline metallicities were shown to be well calibrated against absolute magnitude and outperformed our equivalent width measurements with respect to the variation in the slopes required to fit Figure 2.10. We found that the standard uncalibrated [m/H] also did better than literature calibrations when compared to standard clusters in Figure 2.11. Using this [m/H] as our primary metallicity measurement we have the valid (low error) RAVE reductions as a separate dataset. This subset is 7,036 stars (see Table 2.1). We note that from RAVE documentation, for $T_{\rm eff} \leq 8000$ K, there is little dependence of the recovered values of [m/H] or log(g) on $T_{\rm eff}$. Fortunately all of our data fall within $T_{\rm eff} \leq 5000$ K, which is well under this limit.

To separate only the M and K-giants from the data we will use colour cuts on log(g) and $T_{\rm eff}$ as discussed in Section 4.1, where we use the M and K-giant population to help us separate out Sgr stream stars from the smooth halo population of the Milky Way. In the next chapters we will describe our expanded data set for the core and stream of Sgr, as well as the process used to select the highest probability members of the Sgr dwarf from our data and what that implies for our knowledge of the dwarf and its associated stream.

"Reality is merely an illusion, albeit a very persistent one."

Albert Einstein

3

Observations and Analysis of the Sagittarius Core

3.1 Introduction

The core was the first part of the Sagittarius dwarf galaxy that was discovered (Ibata et al. 1994, 1995). As mentioned in Chapter 1, it is the closest known satellite galaxy of the Milky Way, and is in the process of strong tidal disruption. Since its discovery, the properties of the Sgr dwarf core have been studied extensively. A summary of observed core parameters from the literature and this work is shown in Table 3.1.[1]

[1]Positional, structural, and dynamical parameters for over 100 nearby galaxies are kept updated in tables by McConnachie (2012), and we checked our values for Table 3.1 with McConnachie (2012) and all relevant original sources.

Property	Value	Source
Hubble type	dSph	(McConnachie 2012)
R.A., DEC	18:55:19.5, −30:32:43	(McConnachie 2012)
Age	10-12 Gyr	(Sarajedini & Layden 1995; Mateo et al. 1995, 1996)
(m-M)o	17.10 ± 0.15	(Monaco et al. 2004)
Brightness	$\mathrm{M_V} = -13.27$	(Majewski et al. 2003)
Apparent magnitude	$V = 3.6 \pm 0.3$	(McConnachie 2012)
Heliocentric distance	$\mathrm{D}_\odot = 26.30 \pm 1.8$ kpc	(Monaco et al. 2004)
Half light radius	$\mathrm{r_h} = 0.42 \pm 0.08$ arcmin	(Bellazzini et al. 2008)
[Fe/H]	-0.4 ± 0.2 dex	(Chou et al. 2007)
[m/H], $\sigma_{m/H}$	-0.59,0.34 dex	(this work)
$\mathrm{V_{GSR}}$, $\mathrm{V_{helio}}$	168.4, 139.4 km s^{-1}	(Bellazzini et al. 2008)
Velocity dispersion	11.4 ± 0.7 km s^{-1}	(Ibata et al. 1997)
$\mathrm{V_{GSR}}$	168.76 km s^{-1}	(this work)
$\sigma^{\mathrm{all}}_{\mathrm{VGSR}}$	12.2 km s^{-1}	(this work)
$\sigma^{\mathrm{typ}}_{\mathrm{VGSR}}$	12.7 km s^{-1}	(this work)
Orbital parameters		As used by (Peñarrubia et al. 2011)
(D,l,b)	25 kpc,5°.6,−14°.2	(Ibata et al. 1995)
v_{los}	137 km s^{-1}	(Ibata et al. 1997)
$(\mu_l \cos(b),\mu_b)$	$(-2.35 \pm 0.20,-2.07 \pm 0.20)$ mas/yr	(Dinescu et al. 2005)
(u,v,w)	(221,−74,203) km s^{-1}	(Peñarrubia et al. 2010)
$(\Pi,\Theta,W)_{Sgr}$	$\simeq$(110,−37,264) km s^{-1}	(Peñarrubia et al. 2011)

TABLE 3.1: Properties of the core of the Sagittarius Dwarf Spheroidal from the literature as well as this work. The V magnitude is extinction corrected, $\mathrm{M_V}$ is absolute visual magnitude, σ^* is the observed velocity dispersion of the stellar component and its uncertainty is based on multiple velocity measurements of individual (giant) stars, and therefore may not be directly comparable to our larger area of observations. The $\sigma^{\mathrm{all}}_{\mathrm{VGSR}}$ is the overall scatter from Section 3.6 and $\sigma^{\mathrm{typ}}_{\mathrm{VGSR}}$ is the typical standard deviation from Section 3.5. The orbital parameters are given by its position (D,l,b), the line of sight velocity v_{los}, the proper motion $(\mu_l \cos(b),\mu_b)$, and space motion (u,v,w).

As mentioned in Chapter 2 the core area consists of two main regions as defined by our two observing runs:

- Core 1, the region containing the initial six measurements. This region was used to determine that the core does not show signs of internal rotation, and for illustrating the data reduction process in Chapter 2.

- R01, the expanded region around the core, including Core 1. This region is discussed in detail in the following sections.

Although a great many observations were obtained for this project, by far the most complete coverage that we have attained is that of the R01 region covering the Sagittarius core. The R01 area spans a width of roughly 8 to 10 degrees and a height of about 6 degrees on the sky; centred on the Sgr core. As noted previously, this represents the largest sample of M and K-giant spectra in the Sgr core region to date (Hyde et al. 2011). We note that this does not include extended stream fields as those are discussed in Chapter 4.

Using the colour cuts and criteria described in Chapter 2, we might expect to find a comparatively metal-rich stellar population for the bulk of the core population based on the results of Cole (2001). We use this information with our own observations to characterise the metallicity and velocity distributions in the core in more detail.

3.1.1 Initial Core 1 data set

In reproducing the features of the Sagittarius stream two effects have proven challenging to model. Firstly there is a bifurcation in the leading stream, showing similar ages, metallicities, velocities and distances (Yanny et al. 2009; Niederste-Ostholt et al. 2010). Secondly the position of the stream on the sky suggests that the dark matter halo for the Milky Way (interior to the stream) may have an oblate or spherical shape (Johnston et al. 2005; Fellhauer et al. 2006). This was additionally examined by Law et al. (2005), who looked at spherical, prolate and oblate model halos. Although a simple spheroidal dwarf galaxy encountering the gravitational potential of the Milky Way is an attractive idea, when simulated numerically, this scenario does not reproduce several features seen in the stream of the Sgr dwarf. Recently a triaxial model of the dark matter halo was introduced by Law & Majewski (2010), which resolved some mutually exclusive results, but could not resolve the problem of the bifurcation in the stream. The spherical, prolate, oblate, and triaxial models are discussed further in Chapter 4 when we look at our stream data in detail.

The bifurcation of the leading tail of the Sgr stream detected in the SDSS survey (Peñarrubia et al. 2010) naturally arises in models in which Sgr was originally a disk galaxy, and where the disk of the Sgr dwarf is misaligned with respect to its orbital plane. For this reason, Peñarrubia et al. (2010) proposed that the progenitor might have been a very different object from the pressure supported spheroid commonly used. The model of a rotating disky progenitor was put forward and if this was indeed the case, we should still see rotation in the core of the Sagittarius dwarf. The initial six pointings we observed resulted in spectra of over 2000 stars near the core of Sgr. We used this sample to test the disk-galaxy hypothesis, and we present here our preliminary results, along with a comparison to model predictions.

The disk type progenitor of Peñarrubia et al. (2010) and Peñarrubia et al. (2011) is modelled with N-body simulations, where the Milky Way disk is represented by a Miyamoto & Nagai (1975) model. The Milky Way bulge profile used is from Hernquist (1990) and the dark matter halo is modelled as a Navarro-Frenk-White profile (Navarro et al. 1996) as in Klypin et al. (2002). This model made several assumptions about Milky Way parameters, notably using a disk mass of $M_d = 7.5 \times 10^{10}$ $M_\odot$, a disk scale radius of $c = 1.2$ kpc, a dark matter halo virial mass of $M_{vir} = 10^{12}$ $M_\odot$, a virial radius of $r_{vir} = 258$ kpc and a concentration $c_{vir} = 12$. As in Law & Majewski (2010), a triaxial halo is assumed. The Sgr orbital parameters used for Peñarrubia et al. (2010) are given in Table 3.1.

The N-body simulation uses the modelled behaviour of the Milky Way and integrates the test particles back in time from their current position to derive a set of initial conditions. The Milky Way halo parameters are fixed through the evolution and the integration time of 2.5 Gyrs corresponds to about 2.5 orbital periods for the Sgr dwarf progenitor. Setting the halo parameters as outlined above, the N-body representations of the Sgr stream progenitor are integrated forward 2.5 Gyrs to roughly present day when the rotation and pressure supported progenitor models have lost 42% and 48% of their initial stellar mass (Peñarrubia et al. 2011).

3.1.2 Rejecting the disky progenitor hypothesis

Figure 3.1 shows the six Core 1 pointings, where the centre of the Sgr dwarf is located in the middle with 2 pointings to the left, 2 to the right and 2 below. Due to cloudy weather it was not possible to map out a full grid, but the Core 1 fields were sufficient

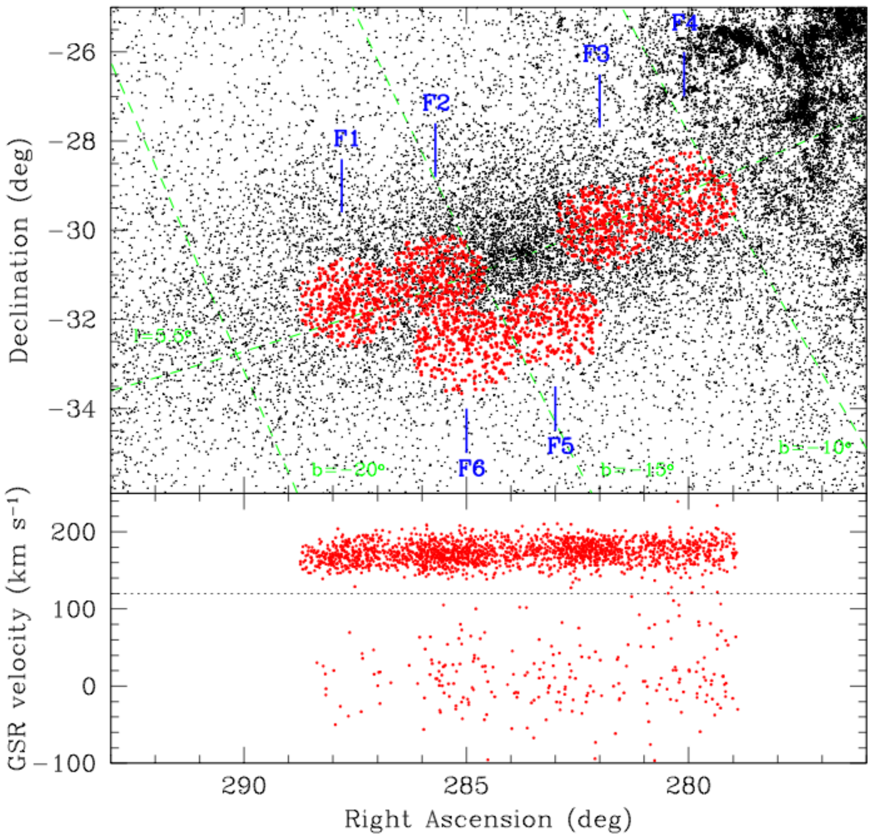

Figure 3.1: The initial six Core 1 fields observed from Peñarrubia et al. (2011) are shown in red. The black points are the 2MASS catalog input with the color selection as discussed in Section 2.2 (i.e. $9 < K < 13$ and $J - K > (20.0 - K)/90.0$ from Majewski et al. (2004)). The separation in velocity of the Sgr core region is illustrated by the dotted line in the bottom panel.

to test for rotation. For these 6 pointings, we find the velocities shown in Figure 3.1 (the data reduction and analysis is discussed in Chapter 2).

If Sgr was in fact originally a disk galaxy, the model of Peñarrubia et al. (2011) predicts that the core should still show residual internal rotation with an amplitude of ~ 20 km s^{-1}.

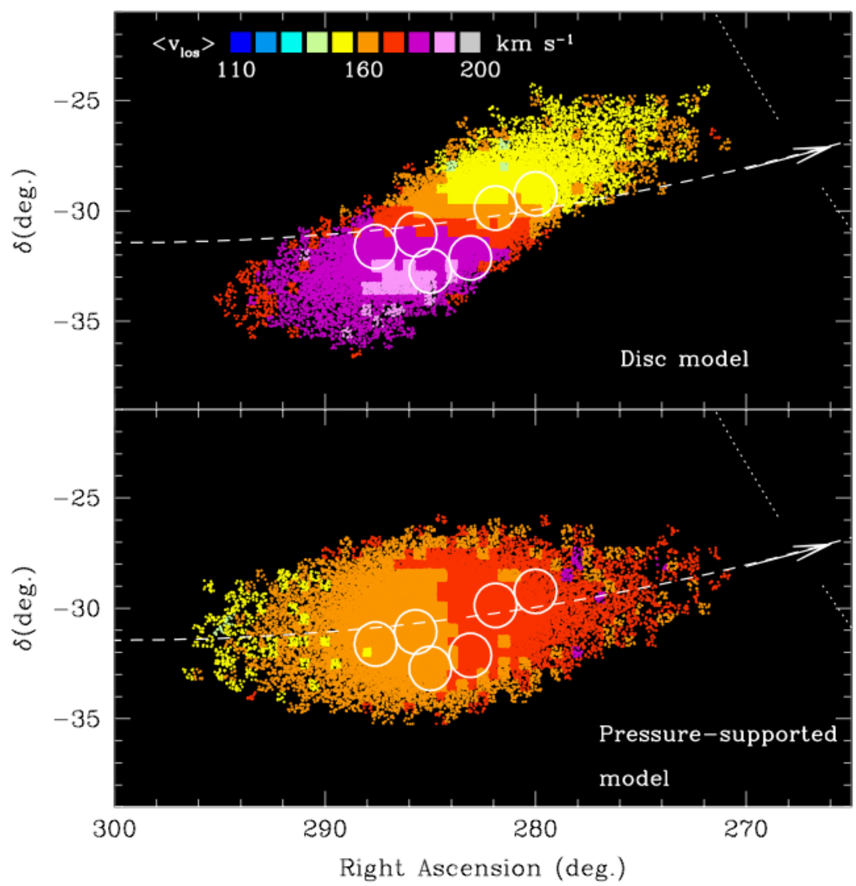

FIGURE 3.2: The model predictions for the Core 1 fields of Figure 3.1 (from Peñarrubia et al. 2011). The points shown are the model points at different velocities in the case of the disk model (top) and the pressure supported model (bottom). The white circles show where our observations would lie in the case of each model. The disk model predictions at the top show a much stronger change in velocity for our pointings than the pressure supported model at the bottom. We note that in the pressure supported case the gradient in velocity is due to the Sgr dwarf's orbit around the Milky Way.

Stars were selected with a velocity cut of $V_{GSR} > 120$ km s^{-1} to correspond with the Sagittarius dwarf core (the dotted line in the bottom panel of Figure 3.1). Models presented in Peñarrubia et al. (2011) fit our Core 1 data and simulate the stream progenitor as a pressure-supported, mass-follows-light system, and, significantly, as a late-type, rotating disk galaxy. These models are shown in Figure 3.2.

Although there is a predicted rotation signature in the disk model, we also see a ~ 10 km s^{-1} gradient in velocity across the body of the dwarf in the pressure-supported model. This velocity gradient is consistent with a velocity distance due to a line-of-site projection of the orbital velocity vector. This is because the orbital trajectory (the dashed line in Figure 3.2) is nearly perpendicular to the disk of the Milky Way (the dotted line in Figure 3.2). This gives an approximately 16 km s^{-1} difference between the pointings which are closest and furthest from the Milky Way plane. We note that this is similar in magnitude to the raw velocity trend seen by Frinchaboy et al. (2012), who are able to completely subtract the trend by correcting for either a solid body or the model of Law & Majewski (2010).

Hence, velocity measurements should be able to distinguish between the disk model and the pressure-supported model. We compare the velocity profiles in each field to both models in Figure 3.3. The two fields with the largest distance between them are F1 and F4, which have a 8° separation. The peak in velocity shifts from $\simeq$ 185 km s^{-1} in F1 to $\simeq$ 165 km s^{-1} in F4. This matches the projection effect rather well and as such does not indicate any rotation. It was noted by Peñarrubia et al. (2011) that additionally there is no such shift in the minor axis between F2 and F6, which is further evidence that it is in fact only due to this line of sight projection. The pressure-supported model in Figure 3.3 clearly yields a better match, although it fails to reproduce the line-of-sight velocity distribution. Although the pressure supported model does not reproduce the velocity distribution, it does provide a qualitative description of the mean velocities seen in the Sgr dwarf core.

Our initial six pointings show no evidence for internal rotation at the predicted level of $\sim$ 20 km s^{-1} in the remnant core (Peñarrubia et al. 2011) of the Sgr dwarf. The accuracy of this non-detection was $\sim$ 2 km s^{-1}. The non-rotating nature of the Sgr core was confirmed by additional measurements from Frinchaboy et al. (2012), who limit any potential trend in velocity to $\leq$ 4 km s^{-1} deg^{-1}. This appears to rule out models where the bifurcation in the Sgr stream was caused by transfer of angular momentum from the progenitor.

From the prediction and null detection of rotation in the remnant core of the Sgr system as proposed in Peñarrubia et al. (2011), it was concluded that more detailed

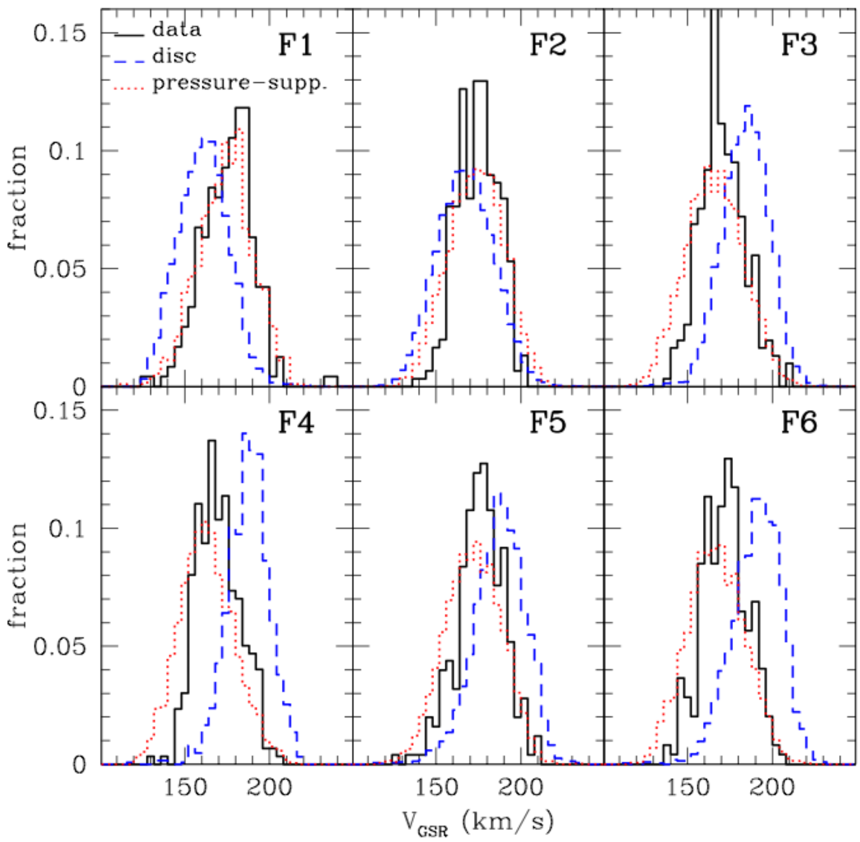

FIGURE 3.3: Velocity histograms of the six fields in Figure 3.1 (from Peñarrubia et al. 2011). Our observations are shown in black, the disk model prediction is shown in blue and the pressure-supported model in red. Although not perfect matches, the pressure supported model is clearly a better fit to the observations than the disk model.

modelling, in addition to more kinematic data, would be necessary. In particular, models that could simultaneously treat the locations and velocities associated in the stream. The triaxial model of Law & Majewski (2010) is used as reference in Chapter 4, and additional measurements by Frinchaboy et al. (2012) expanded the parameter space slightly. We chose an observational approach and, independently of Frinchaboy et al. (2012) obtained a large additional sample set of data on the Sgr core region.

3.2 The core revisited

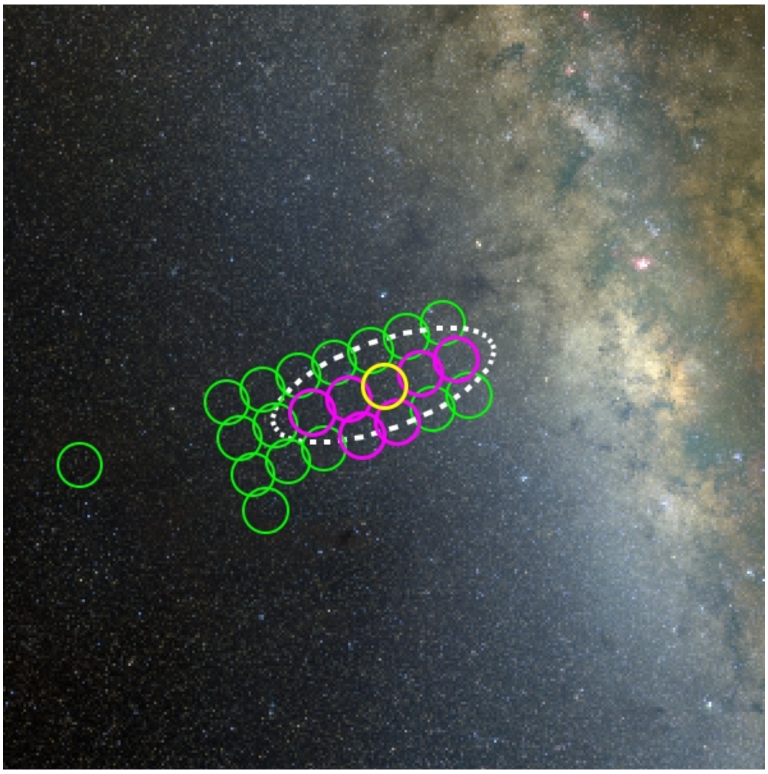

FIGURE 3.4: Sgr dwarf core fields observed (comprising R01). The central field is yellow, the original six fields (Core 1) are magenta, subsequent core observations are shown in green, and the outline of the general shape of the Sgr dwarf is shown in the dashed white oval outline. The field on the left away from the main body is part of the extended stream program, and is additionally discussed in Chapter 4. Background image constructed from online data (Mellinger 2009).

After we demonstrated that there was no discernible rotation in the core, we performed a follow-up program to more completely map the core region. These observations increased the number of core fields and we additionally expanded the dataset by combining our observations of the core with the Sgr stream observations initiated by R. Ibata, resulting in the full distribution shown in Figure 3.4.

This extended dataset gave us a total of 23 pointings around the core area. This total core area will be referred to as 'R01', as discussed previously, and includes 9,086 distinct M and K-giant star candidates. The R01 spectra were analysed using the modified RAVE pipeline discussed in Chapter 2. After RAVE quality cuts, we had

7,036 stars in R01 for our analysis. The data were additionally matched to 2MASS to retrieve the JHK colour information. In Figure 3.4 we show the final distribution of fields observed.

To analyse this region we have developed several techniques to divide up the Sgr dwarf and investigate changes in metallicity and velocity across the body of observations. The entire dataset in the core region is found to have a mean metallicity of [m/H] = -0.59 dex with $\sigma_{[m/H} \simeq 0.34$ dex and a velocity of $V_{GSR} = 168.76$ km s^{-1} with $\sigma^{all}_{VGSR} = 12.2$ km s^{-1}. These results are shown in detail in Section 3.6 where we summarise our overall core sample. However, with the uneven nature of our sampling, the overlap of some pointings, and a higher density of stars in pointings closer to the Galactic centre, the actual number of stars observed per unit area varies greatly. To separate out our observations in an unbiased way, we will first perform several different spatial divisions of the R01 region and then investigate the entire distribution.

3.3 Radial annuli distribution

One method of looking at the R01 region is to divide the data based on its distance from the centre of the Sgr dwarf. In this investigation, we focus in particular on the metallicity ([m/H]) values of the stars in R01.

As discussed in Chapter 2, the [m/H] value that we get from our modified RAVE pipeline analysis is calibrated to star clusters analysed in the literature. We use only stars with a RAVE Rcoeff ≥ 15 to reduce errors. Since the number of stars in an area varies depending on how many observations we were able to do, we choose to divide R01 into annuli based on the distance from the published centre of the Sgr dwarf as shown in Figure 3.5.

It has been noted that the metal-rich population of dwarf spheroidal galaxies appears to be more concentrated in the central region (e.g., Koch et al. 2006). Harbeck et al. (2001) find dwarf spheroidal galaxies with indications of metallicity gradients, as well as dwarf spheroidals with no or weak gradients. They conclude that '*no two*

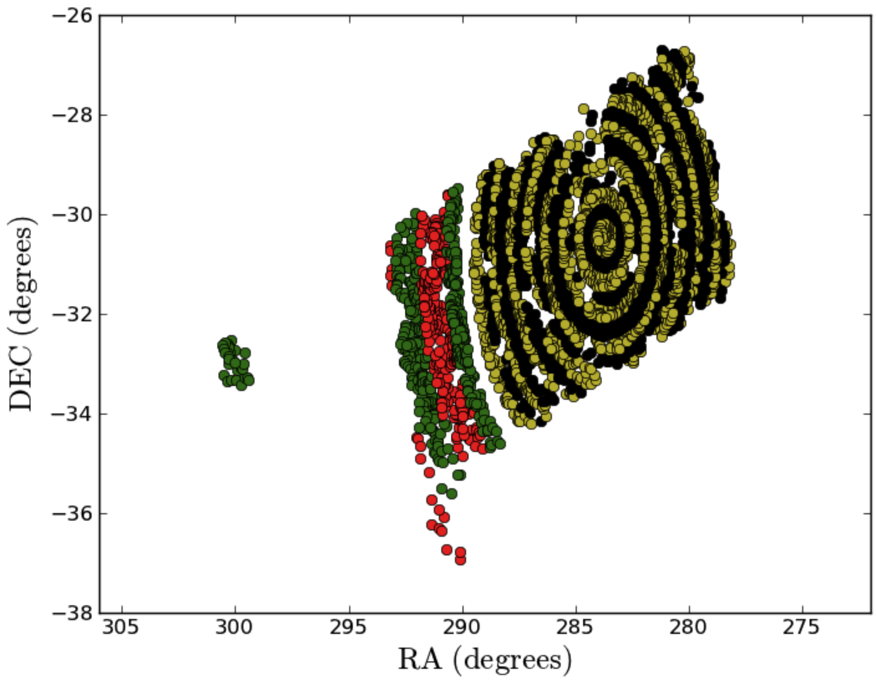

Figure 3.5: Radial annuli for the Sgr core region stars which have a metallicity [m/H] determination with Rcoeff ≥ 15. Yellow and black are finer divisions where we have a higher density of data points, and green and red show broader annuli corresponding to the numerical scale in Figure 3.6.

galaxies are alike, not even when they are of the same morphological type' (Harbeck et al. 2001). To investigate the metallicity and velocity distribution in the core of Sgr we will first set up a fractional metallicity measure.

In Figure 3.5 the data are divided into annuli starting in the centre of Sgr. We use annuli centred at the Sgr core with radii of 0.3°, 0.6°, 1.0°, 1.3°, 1.6°, 2.0°... out to 6° (the first green annulus) and then increase to annuli with widths of 1°, shown at 6°, 7° and 8°. The last two annuli extend from 8° to 9.5° (the last red annulus) and from 12.5° outwards (encompassing the one small green region to the southeast, separated from the core). These degree separations are the angular separations as defined by $D_{center} = R = \sqrt{x^2 + y^2}$ using:

$$x = (\cos(D_{core}) \times \sin(R_s - R_{core}))/Cc \quad (3.1)$$

$$y = ((\cos(D_s) \times \sin(D_{core})) - (\sin(D_s) \times \cos(D_{core}) \times \cos(R_s - R_{core})))/Cc \quad (3.2)$$

$$Cc = (\sin(D_s) \times \sin(D_{core})) + (\cos(D_s) \times \cos(D_{core}) \times \cos(R_s - R_{core})) \quad (3.3)$$

where R_s and D_s are the RA and DEC positions of the stars and (R_{core},D_{core})$\simeq$ (283.7,-30.48) is the centre of Sgr, and the location of M54 (Harris 1996; Sarajedini & Layden 1995). The separation for these annuli are additionally shown by the red points in Figure 3.6. These radii are chosen to give a reasonable number of counts in each region so that we can compare the metallicity from the outer to inner regions.

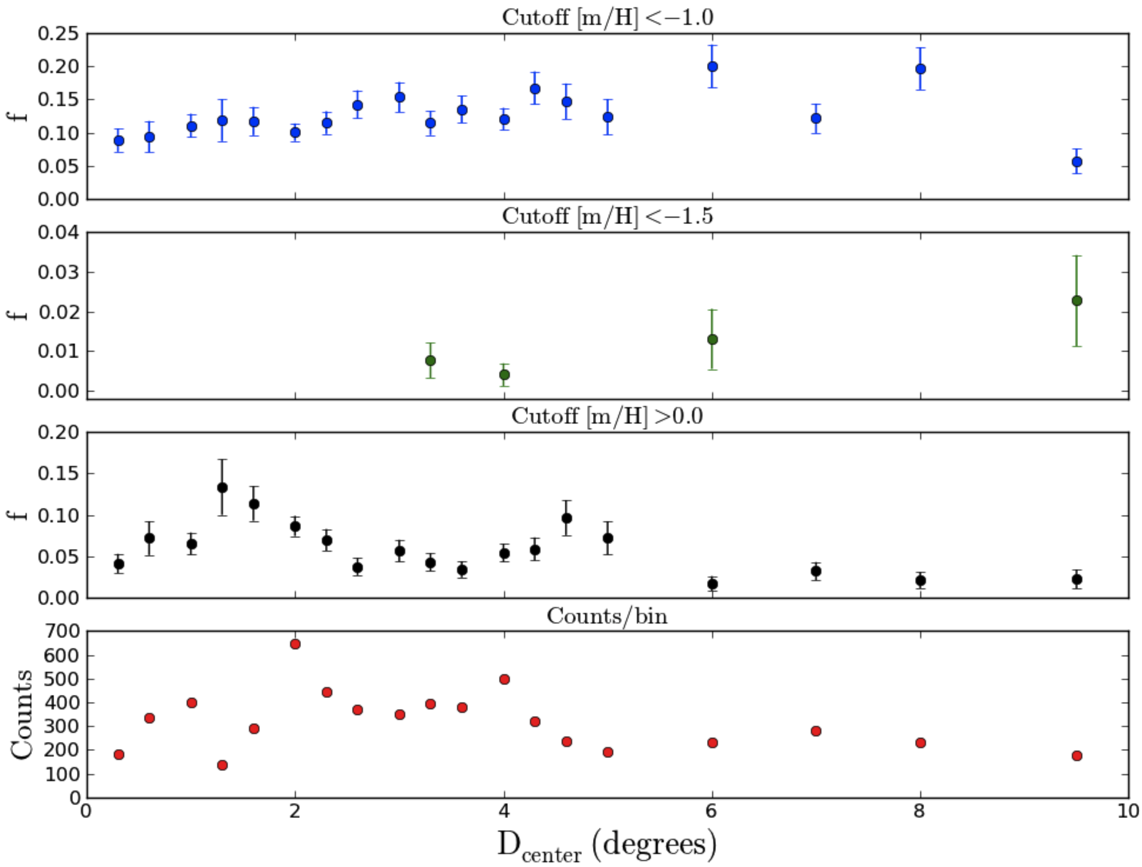

Figure 3.6: The fractional metallicity f, at cut off values of less than [m/H]$= -1.0$, less than [m/H]$= -1.5$, or more than [m/H]$= 0$ for the annuli in Figure 3.5. The total number of stars in each annulus is shown in the bottom panel.

We divide our candidate M and K-giants into metallicity bins, designed to trace the fractional contributions of metal-poor (less than [m/H]$= -1.0$ and less than [m/H]$= -1.5$) and metal-rich (greater than [m/H]$= 0.0$) components. We consider the fractional metallicity in each annulus in the main body from Figure 3.5 for each of these bins as shown in the panels of Figure 3.6. We do not include the final small green region at larger radii as it contains only 29 stars (versus the more than 100 points in each other region).

Since the RAVE values of [m/H] are less reliable below [m/H]$= -1.5$ we have less (low error) measurements in that panel of Figure 3.5. The low metallicity population is not well probed in this sample, and although we expect the bulk of the stars to peak around [m/H]$\simeq -0.4$ dex, there may be an unprobed metal poor tail to the distribution. This possibility is discussed later in Section 3.6. For each annulus we then calculate the fraction of stars:

$$f = N_p/N_{all} \tag{3.4}$$

where N_p is the number of stars either below [m/H] of -1.0 (the first low metallicity bin), below -1.5 (the second low metallicity bin) or above [m/H] of zero (the third bin). The fractional metallicity change for each of these cases is shown in Figure 3.6. The 'Counts' axis in Figure 3.6 shows the total number all (N_{all}) stars within each annulus. Assuming Poisson errors in Figure 3.6 the error bars are calculated individually for each point f. For Poisson errors the standard deviation is defined as the square root of the variance $\sigma \equiv \sqrt{V} = \sqrt{N}$ so the error bars use an error of:

$$f_{err} = f \times \sqrt{(\sqrt{N_p}/N_p)^2 + (\sqrt{N_{all}}/N_{all})^2}. \tag{3.5}$$

In the low metallicity cut from Figure 3.6 objects with metallicity less than [m/H]$=$ -1.5 are not well sampled as we only have objects in four of our annuli which meet this criterion. We note that even with our sampling, the number of stars does change in each annulus (see Figure 3.6), so although trends are apparent additional mapping is necessary. The mapping of metallicity further out into the stream of Sgr is discussed in Chapter 4.

In Figure 3.6 we have a possible increase of stars with metallicity greater than [m/H]$= 0$ just inside $D_{centre} \simeq 2°$ from the centre. Some evidence has additionally been found by McDonald et al. (2013) suggesting a greater fraction of metal-rich stars concentrated near the centre of the Sgr dwarf (near M54). While we expect the core of Sgr to be fairly well mixed in terms of its metallicity population (Bellazzini et al. 1999a), the absence of metal rich stars in the tidal tails found by Chou et al. (2007);

Carlin et al. (2012) does suggest selective stripping of metal poor stars away from the Sgr dwarf core over the last several Gyr (Bellazzini et al. 2006b; Chou et al. 2007). The centre of the Sgr dwarf has previously been measured at a slightly higher metallicity than the surrounding area (Cole 2001). We detect a possible peak of stars greater than [m/H]=0 just inside $D_{centre} \simeq 2°$ from Figure 3.6, but before investigating the central region of Sgr in more detail we need to determine what impact the M54 globular cluster might have (if any) on our data.

3.4 M54: the cluster in the core

The M54 globular cluster (also known as NGC 6715) sits in the centre of the Sgr dwarf and has the same heliocentric velocity. It was thought that the Sgr dwarf might be a nucleated galaxy with M54 as its nucleus (Sarajedini & Layden 1995; Layden & Sarajedini 1997, 2000), but due to the very different velocity profile shapes (M54 has a much narrower profile), and metallicities of the two objects (Siegel et al. 2007; Bellazzini et al. 2008), it is now believed that the Sgr nucleus formed independently of M54.

From Bellazzini et al. (2008) we expect that the spatial extent of M54 should not exceed 12 arcmin from the centre of Sgr and should drop off sharply after 4 arcmin. We furthermore expect for M54 that [Fe/H] would range from about -1.1 to -1.8 (Bellazzini et al. 2008). This metallicity was updated to [Fe/H]$\sim -1.6 \pm 0.19$ by Carretta et al. (2010). From Chou et al. (2007) the Sgr dwarf should have $\langle$[Fe/H]$\rangle = -0.4 \pm 0.2$. If M54 is visible in our data, a population of lower metallicity stars within the innermost regions of our core data should be evident.

Previously we looked at the fractional changes in metallicity in slices of distance from the centre of the dwarf. By choosing annuli at smaller radii, we can determine if there is a significant M54 component closer in to the centre. Using radial annuli, we see in Figure 3.7 that between 0 and 0.3 degrees from the centre there is a possible separation between metallicity peaks at [m/H]~ -1.2 and [m/H]~ -0.5. We continue

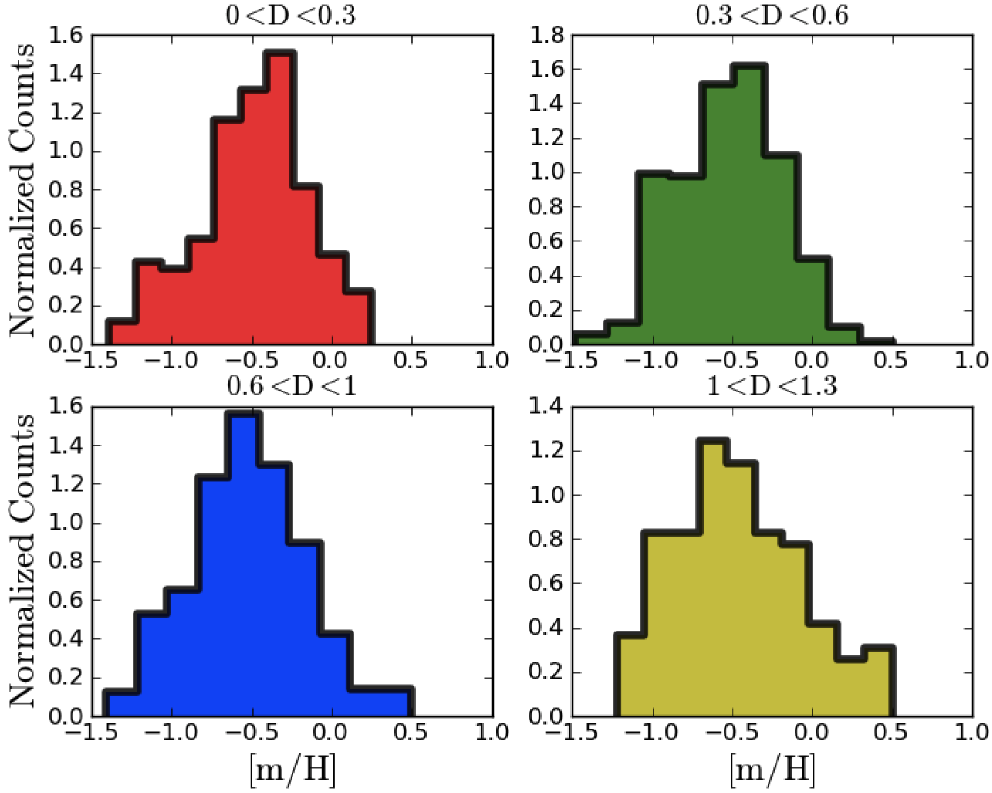

FIGURE 3.7: Normalised MDFs within different distances D from the core (these correspond to the annulus radii mentioned in Figure 3.5), between 0 and 0.3 degrees, from 0.3 to 0.6 degrees, from 0.6 to 1 degree and from 1 to 1.3 degrees. Each annulus contains 181, 338, 398, and 135 stars, respectively.

to see a component of metallicity between [m/H]~ -1.1 and [m/H]~ -1.5 at higher radii. From 0.3 to 0.6 degrees we still see what could be two populations, but in the MDFs from 0.6 to 1 degrees (blue) and 1 to 1.3 degrees there is no evidence of a significant component from M54. Hence, based on Figure 3.7 there is a potential for a small 1 to 3 star contribution from M54 within 0.6 degrees from the centre of Sgr.

Figure 3.7 additionally shows the MDF of each individual region of the Sgr core. The regions, from the center going out, contain 181, 338, 398 and 135 stars, respectively, and show a peak in their metallicity distributions at roughly $\simeq -0.5$ dex. The slightly increased metal rich fraction in the outer region between 1 to 1.3 degrees gives us our first hint that the inside of the core might have a different distribution in metallicity than the outside. This issue will be investigated in the following sections, but will not affect our investigation for potential M54 contamination. To check the inner region of Sgr in more detail for M54 contamination we look at finer spatial divisions.

To include a finer view of the interior of the Sgr dwarf core we calculate the MDF as we step over progressively larger areas, rather than annuli at different distances. We choose to look at the cumulative MDF corresponding to all the stars within 0.2° (12 arcmin), 0.1° (6 arcmin), and 0.06° (3.6 arcmin) from the centre of Sgr. The cumulative MDF is calculated at a range of radii from the centre in Figure 3.8. At a distance D< 0.03°, we are 1.8 arcmin from the centre and should have a high contribution from M54 stars, but our relatively low target density in this small area samples only 4 stars. We sample the MDF at distances D of 0.03, 0.06, 0.1, 0.2, 0.3, 0.6, 1, 1.3 degrees. The number of objects in each bin for the plots in Figure 3.8 are 4, 13, 37, 105, 181, 519, 917, and 1052, respectively.

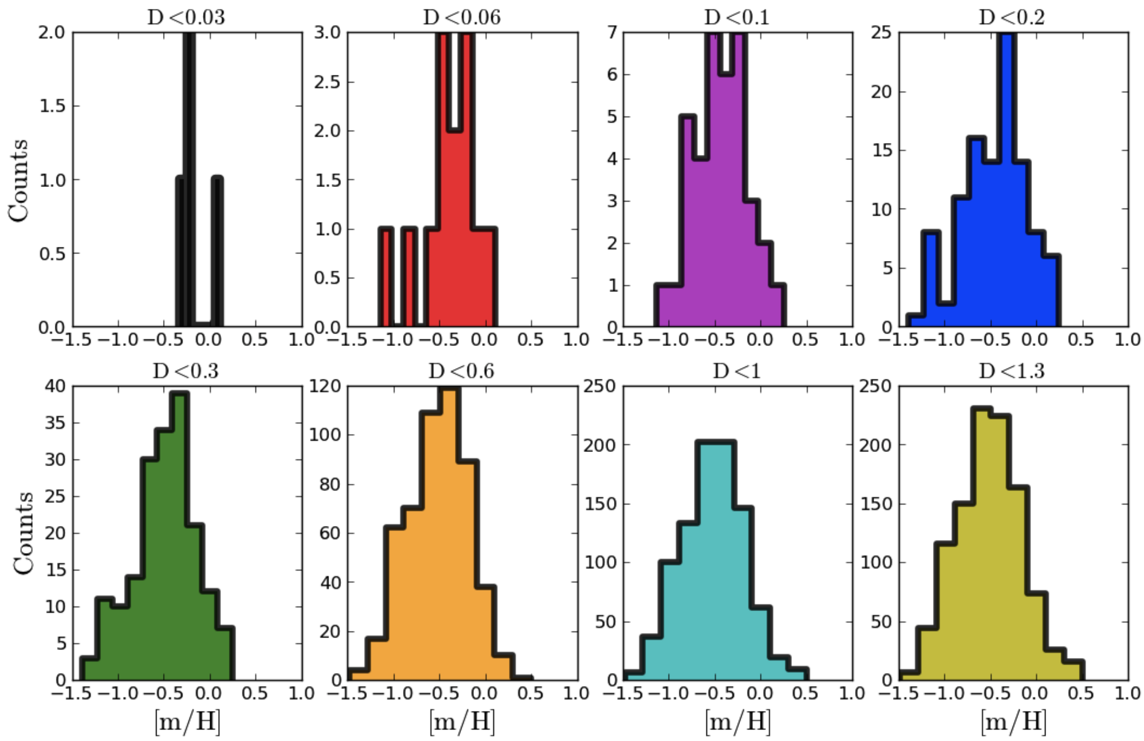

FIGURE 3.8: The MDFs within different distances D from core. The raw number of counts is shown; note that the D< 0.3 histogram corresponds to the normalised plot of 0 <D< 0.3 in Figure 3.7. The left peak in the (dark blue) D< 0.2 MDF shows the best population separation and the most likely detection of M54.

The MDF evolution in Figure 3.8 shows a separation in population for D$< 0.06°$ which corresponds to 3.6 arcmin. We confirm the two stars to the left of the main (red) distribution in the D< 0.06 plot as a likely detection of M54. Previous measurements have found that the M54 distribution drops off sharply after about 4 arcmin (Bellazzini et al. 2008). We further expect that the M54 contribution should not extend past 12 arcmin or D$< 0.3°$. This is seen in Figure 3.8 as the separation between the populations at [m/H]~ -1.2 and [m/H]~ -0.5 is not visible past a distance from the core of D$< 0.3°$. The number of stars which may be from M54 rather than the Sgr dwarf would be at most 1-6 based on the D$< 0.2°$, D$< 0.1°$, and D$< 0.06°$ histograms in Figure 3.8. We note that, although the green D$< 0.3°$ histogram does have a higher number of stars at [m/H]~ -1.2 dex, we expect that most of these will be part of the Sgr distribution. At greater distances when more stars are included, the Sgr MDF distribution easily takes over and overwhelms any potential M54 component.

3.5 Hexagon-based spatial distributions

The centre of the Sgr dwarf corresponds to the region of the globular cluster M54, but our core R01 region is much greater in extent. We use the entire area shown in Figure 3.4. This region has an advantage over other parts of the Sgr dwarf in the stream, namely that the Sgr stars near the core separate well in metallicity and velocity from Galactic contamination. We want to characterise the behaviour of the velocity and metallicity in more detail. As the data coverage is uneven, one option for doing this is to bin the data spatially.

We choose hexagonal spatial binning which divides the data into regions shown in Figure 3.9. For each hexagon in Figure 3.9 the colour shows the number of points in the bin with the bin centres given by black dots. We note that the bin centres are determined by the desired density of hexagons in the region, these do not correspond to our previously mentioned observational regions. We use the Python task '*hexbin*' to generate our areas by requesting a gridsize of 20 over our total range. This then

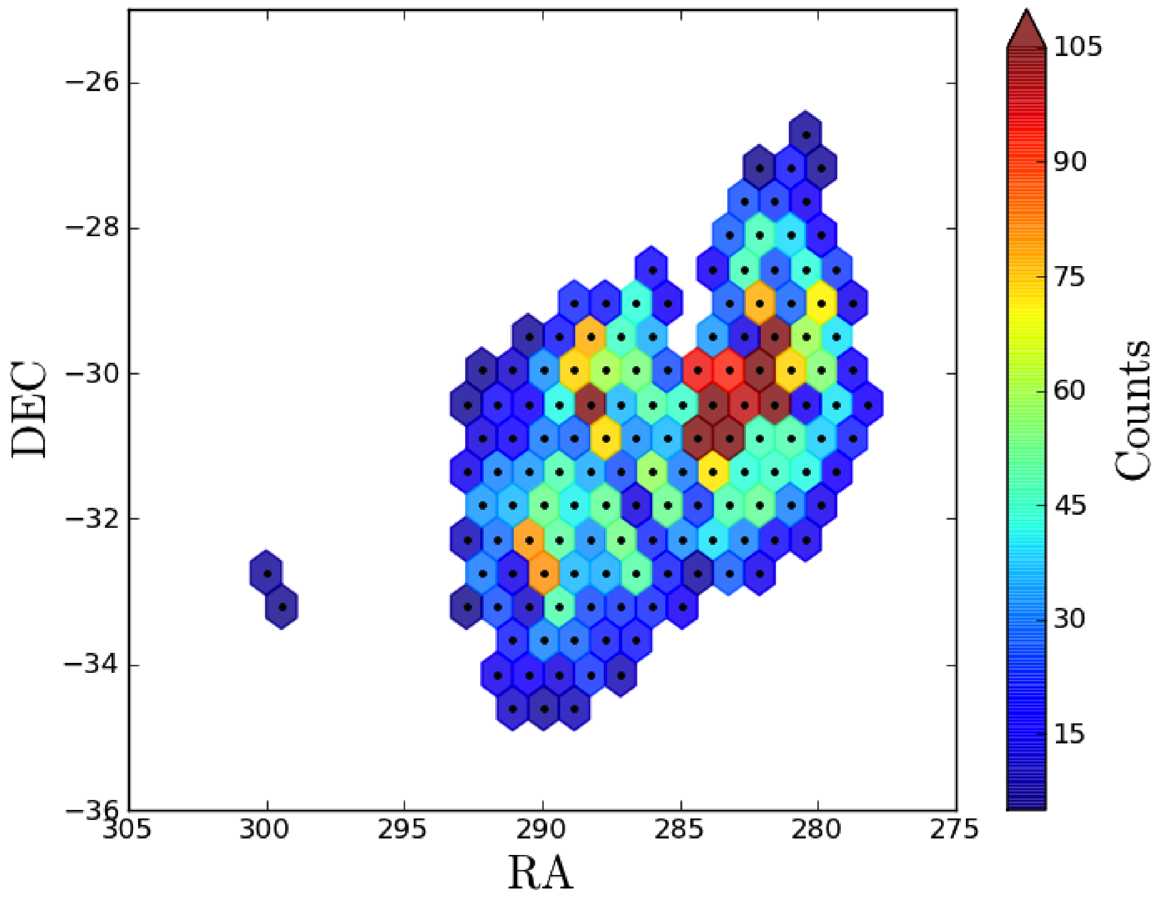

Figure 3.9: Hexagonally binned image for the spatial distribution of our stars. Each centre is given by the black points, and colours correspond to the mean number of stars in each hexagonal region. Note that bin centres do not correspond to pointings and are assigned based on the hexagon density.

generates 146 hexagons which then can contain various parameter information for the points inside. For Figure 3.9 we have the sum returned using the Python sum '*np.sum*' which gives us the number of points in each area. We additionally define an extent for our area which is bounded by the maximum and minimum coordinates in RA and DEC for Figure 3.9, 3.10 and 3.11. This results in a consistent area and identical binning for these plots. We require that there be at least 5 points in each bin to create the values shown; we do this directly in the '*hexbin*' function and blank areas on the plot correspond to 4 or fewer valid measurements of the quantity in question.

To characterise the velocity over the R01 region, we calculate the mean values of the Galactocentric velocity, V_{GSR}, as well as the standard deviation σ_{VGSR} in each hexagonal area. As in Figure 3.9, for Figure 3.10 this is done by generating '*hexbin*' areas. In the case of Figure 3.10 we return the Python mean '*np.mean*' mean value of the velocity to produce the top plot and we return the standard deviation in Python '*np.std*' to reproduce the bottom plot. For velocity measurements we require that the measurement error be less than 3 km s^{-1} for each star and that it be within 60 km s^{-1} of the average core velocity of $V_{GSR} \simeq 168.4$ km s^{-1} (converted from $V_{helio} = 139.4$ km s^{-1} of Bellazzini et al. 2008). The velocity of the core falls within a heliocentric velocity range of 100 to 200 km s^{-1} (or $120 < V_{GSR} < 180$ km s^{-1}) based on its radial velocity profile within 3σ. The resulting mean velocity and velocity standard deviation maps in Figure 3.10 show the changes with RA and DEC for these quantities.

3.5.1 Velocity and metallicity trends

The previous velocity offsets seen between different fields for the Core 1 region (in Figure 2.9) indicated a gradient in velocity with changing spatial coordinates across the Sgr dwarf, and from Figure 3.10 we can see that is indeed the case. From Figure 3.2 the predicted velocity gradient across the body of the dwarf in the pressure-supported model had an amplitude of $\sim$10 km s^{-1}. This is approximately what we would expect due to the orbit of Sgr around the Milky Way (Peñarrubia et al. 2010).

We note that the velocity range illustrated by the colour scale in Figure 3.10 reproduces the velocity trend predicted by the pressure-supported model shown in Figure 3.2. The mean V_{GSR} ranges from about 156 to 170 km s^{-1}, increasing east to west across the RA direction, i.e. an amplitude of $\sim$ 15 km s^{-1}. As mentioned previously there is an approximately 16 km s^{-1} difference expected due to the line-of-sight projection of the orbital velocity vector. Our velocity change is only slightly lower than the expected difference, and as such we do not expect any contribution from other sources. This provides support (using the whole R01 region) for our original result (based on the Core 1 region) matching the non-rotating pressure-supported model of Peñarrubia et al. (2011).

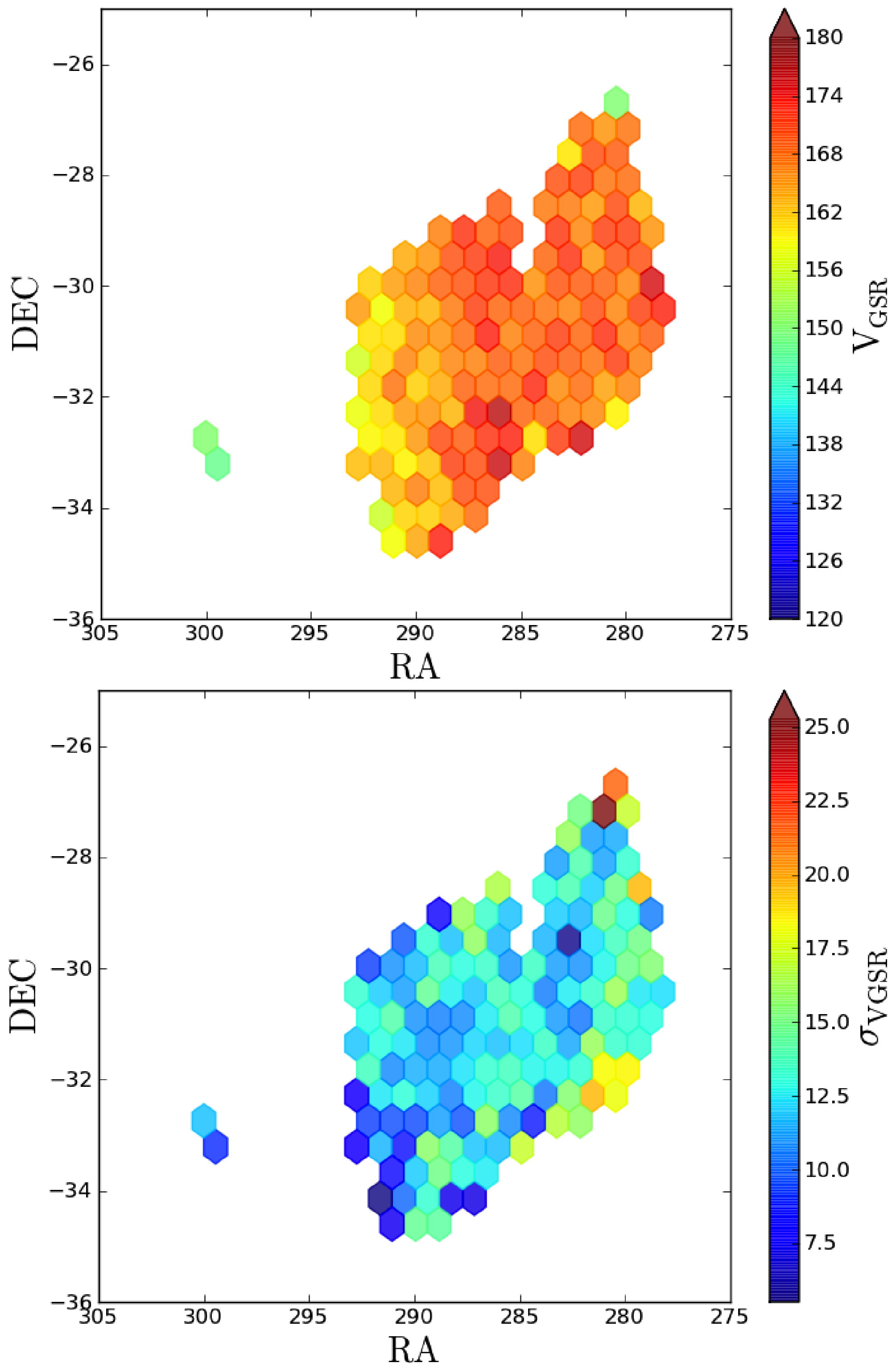

FIGURE 3.10: Hexagonally binned images for the velocity relative to the Galactic Standard of Rest, V_{GSR}, and the standard deviation of that velocity, σ_{VGSR}.

The velocity standard deviation $\sigma_{\rm VGSR}$ shown in the lower panel of Figure 3.10 for each hexagonal region can be used to create an average spatial value of standard deviation. Taking the sum of the individual $\sigma_{\rm VGSR}$ from each hexagon and dividing by the total number of hexagons ($\rm N_{hex} = 146$) we find that the average or 'typical' value of the standard deviation is $\sigma^{\rm typ}_{\rm VGSR} = 12.7$ km s^{-1}. We note that the velocity values corresponding to a high $\sigma_{\rm VGSR}$ in the lower panel of Figure 3.10 have a high error association, and expect that the low velocity given near the top right of the velocity

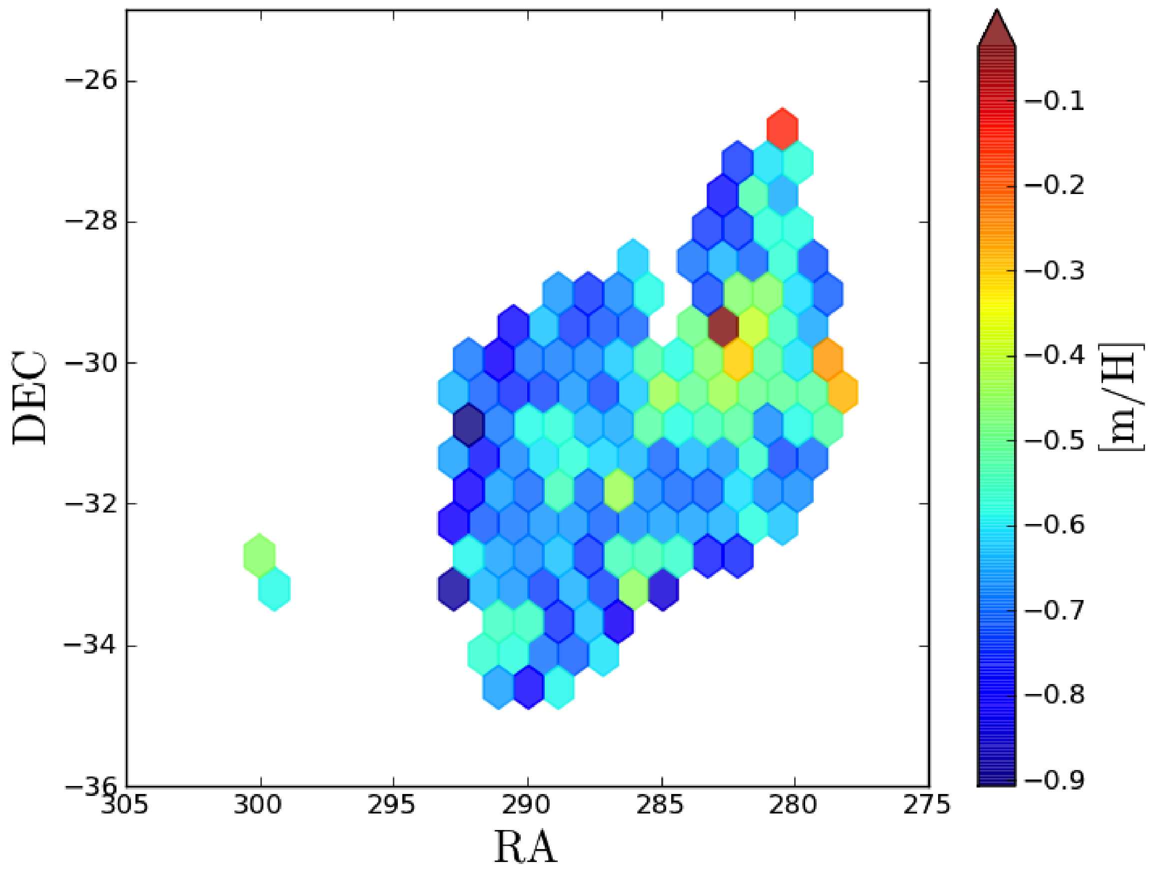

FIGURE 3.11: Binned hexagon images for the metallicity [m/H].

plot is most likely an artefact of that error.

The spatial representation of the metallicity is given in Figure 3.11; for this calculation we simply measure the mean metallicity value in each hexagonal bin, requiring that the RAVE Rcoeff ≥ 15 (as in Chapter 2). This is performed using the same binning as in Figures 3.9 and 3.10 but with the value in the bin this time corresponding to the '*np.mean*' calculation for metallicities contained in the bin. We find a higher average metallicity near the centre of Sgr. This would not be due to M54, as it would contribute a lower metallicity value, and has a negligible contribution, as discussed previously. We also find that the distribution is not completely flat and some variation in metallicity appears to occur from the inner to outer regions, with lower metallicity preferentially farther from the core. This is consistent with the results of Koch et al. (2006), who noted that dwarf spheroidal galaxies can have metal-rich populations which are more concentrated in the centre. This effect will be investigated in the following sections.

3.5.2 Kolmogorov-Smirnov test

What appears to be a shift to a higher metallicity (on average) in the centre parts of the core, as shown in Figure 3.11, is associated with a large range of metallicity values. Broad metallicity distributions are seen in the inner and outer regions as shown in Figure 3.12. We define the cut off for the inner and outer regions that are most significant by using a Kolmogorov-Smirnov (K-S) (Massey 1951) test. The K-S test constructs empirical distribution functions for two sets of points to determine if they are part of the same parent population.

The two-sample K-S statistic is:

$$D = sup_x \; |A(x) \; - \; B(x)| \tag{3.6}$$

where sup_x is the supremum of the set of distances. $A(x)$ and $B(x)$ are the empirical distribution functions of the first and second samples, respectively. This is a two-sided test for the null hypothesis where the two samples are drawn from the same continuous distribution. This method asks the question, '*are these two populations the same?*'. The p-value of this test is the probability of obtaining a test statistic at least as extreme as the one that is observed, assuming that the null hypothesis is true. The null hypothesis can be rejected when the p-value is less than a predetermined significance level. For example, a p-value of 0.01 would indicate that we can reject the

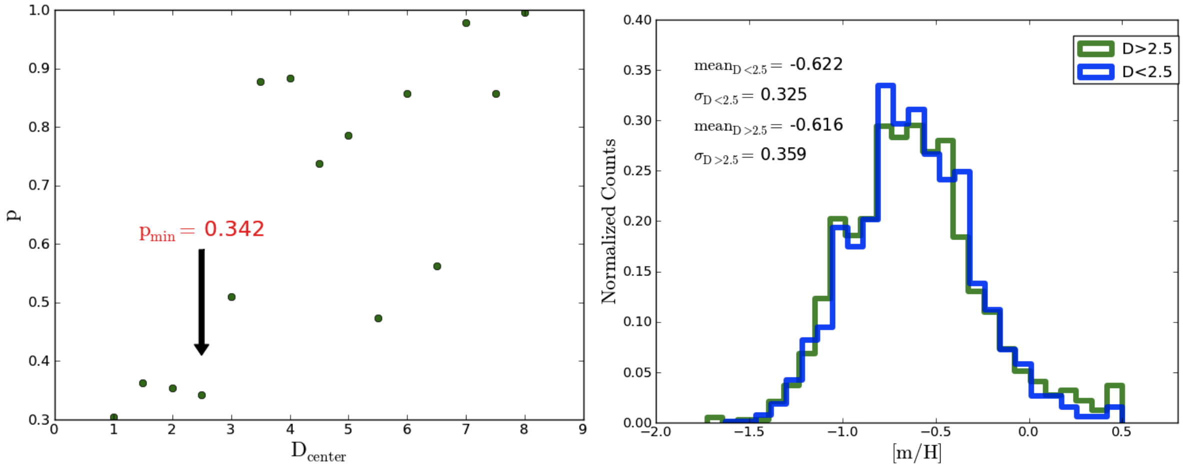

Figure 3.12: The p-value (left) for KS tests on the MDF (right) at different radii. We use two regions, inner and outer with the dividing line for the regions equal to the distance from the center, D (in degrees). The MDF shown on the right is for the two regions created when the data is divided at D= 3°. The high variability (standard deviation) in the measurements of the MDF limits the detection of a shift in the peak metallicity.

null hypothesis at a 2% level (2%>0.01), i.e. the populations are '*not*' the same. If the p value is greater than the significance level, then we cannot reject the hypothesis that the data come from the same population (i.e. for a p-value of 0.3 we cannot reject the null hypothesis at a 30% level, but we can reject it at a 40% level).

To run the K-S test, we divide the data into two regions, an inside and outside region. We then use the metallicity of the inner region (one) as $A(x)$ and the metallicity of the outer region (two) as $B(x)$. Graphically from Figure 3.11 we expect that any difference in the distribution would be around 2-3 degrees from the centre. We use the Python function '*ks_2samp*' to test the two samples. When the p-value is high we cannot reject the hypothesis that the distributions of the two samples are the same. We run the test several times at different dividing radii and plot the resulting p-values in Figure 3.12.

From Figure 3.12 we can see that the p value is generally high, but has a sharp drop to p= 0.342 at a distance D= 2° from the centre of the Sgr dwarf. This visible population difference at D= 2° indicates that the population inside D= 2° is different than that outside, or to use the p-value terminology, we can reject the null hypothesis at 40% as p= 0.342 < 40%. This is then the cut off between the inner and outer regions of Figure 3.12. The variation in the metallicity samples is $\sigma_{[m/H]} > 0.3$ dex for the inner and outer regional MDFs we are interested in.

We conclude that the average metallicity is likely higher within a region roughly 2° from the centre of the Sgr core, but the overlapping MDFs of the inner and outer regions make for a large uncertainty in our measurements.

3.6 Total core metallicity and velocity distributions

The region around the core of Sgr is much more densely populated with Sgr member stars than the Sgr stream (see Chapter 4). As the densest and easiest to detect region, the core has also been studied by a number of other groups. We can thus compare the velocity and metallicity distributions from the literature with our results where we have overlapping observations.

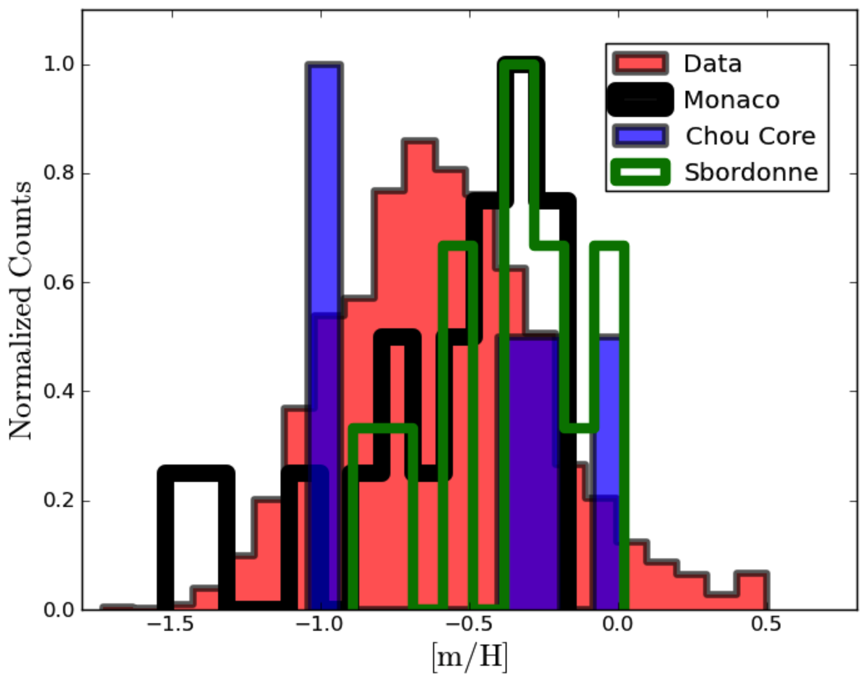

FIGURE 3.13: The distribution of metallicities for the core. These distributions have been normalised to better show the differences in peak positions. We have a higher number of low metallicity objects than previous studies. We include our data in red, and comparison metallicities from 'Monaco' Monaco et al. (2005) in black, 'Chou' Chou et al. (2007) in blue, and 'Sbordone' Sbordone et al. (2007) in green.

We show velocity and metallicity distribution functions (MDFs) in Figures 3.14 and 3.13, respectively. For comparison, we additionally show the core MDFs from Chou et al. (2007), who measure different points along the tidal stream of the Sagittarius, from Monaco et al. (2005), who surveyed 15 red giant branch stars in the core, and from Sbordone et al. (2007), who studied 12 giant stars around the core. In the core region, our MDF (red) is comparable to what other groups have found, but shows more metal-poor objects in a more continuous distribution.

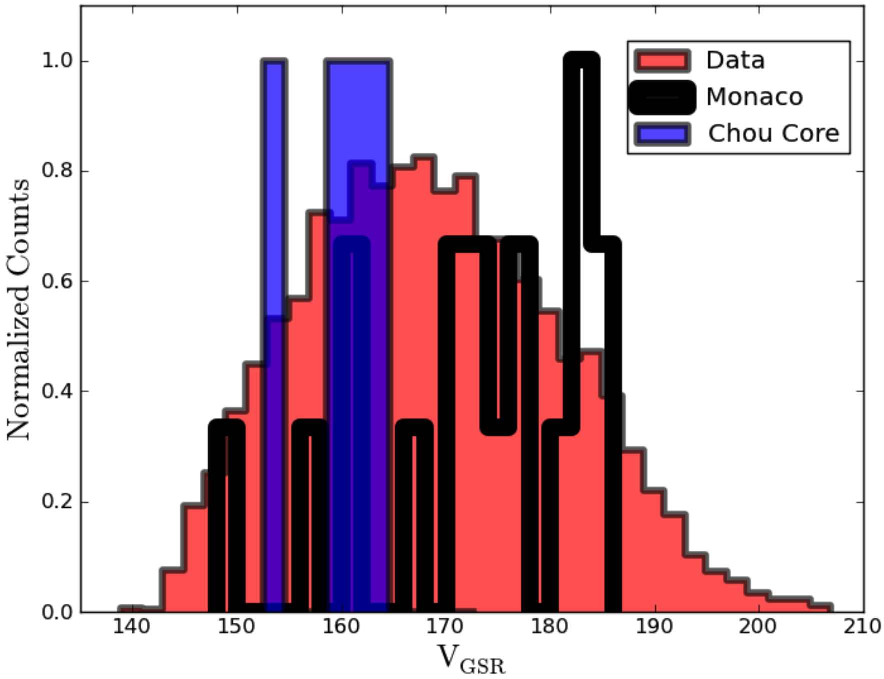

Figure 3.14: The distribution of velocities for the core. These distributions have been normalised to better show the differences in peak positions. The heliocentric velocity measured by Bellazzini et al. (2008), 139.4 km s^{-1} (or $\sim$ 168 km s^{-1} in V_{GSR}), agrees with what we find. We show our data in red, and comparison velocities from Monaco et al. (2005) in black, and Chou et al. (2007) in blue.

Previous measurements of the mean metallicity of the Sgr core have yielded a wide range of values. These estimates include: [Fe/H] $\simeq 1.1 \pm 0.3$ (Mateo et al. 1995), [Fe/H] $\simeq -0.25$ (Bonifacio et al. 2000), [Fe/H]$\lesssim -0.8$ (Whitelock et al. 1996); a spread from $-0.71 \leq$[Fe/H]≤ -1.58 (Mateo 1998); and a range from $-1.3 \leq$[Fe/H]≤ -0.7 (Bellazzini et al. 1999a,b). For the inner regions, within less than half a degree of the

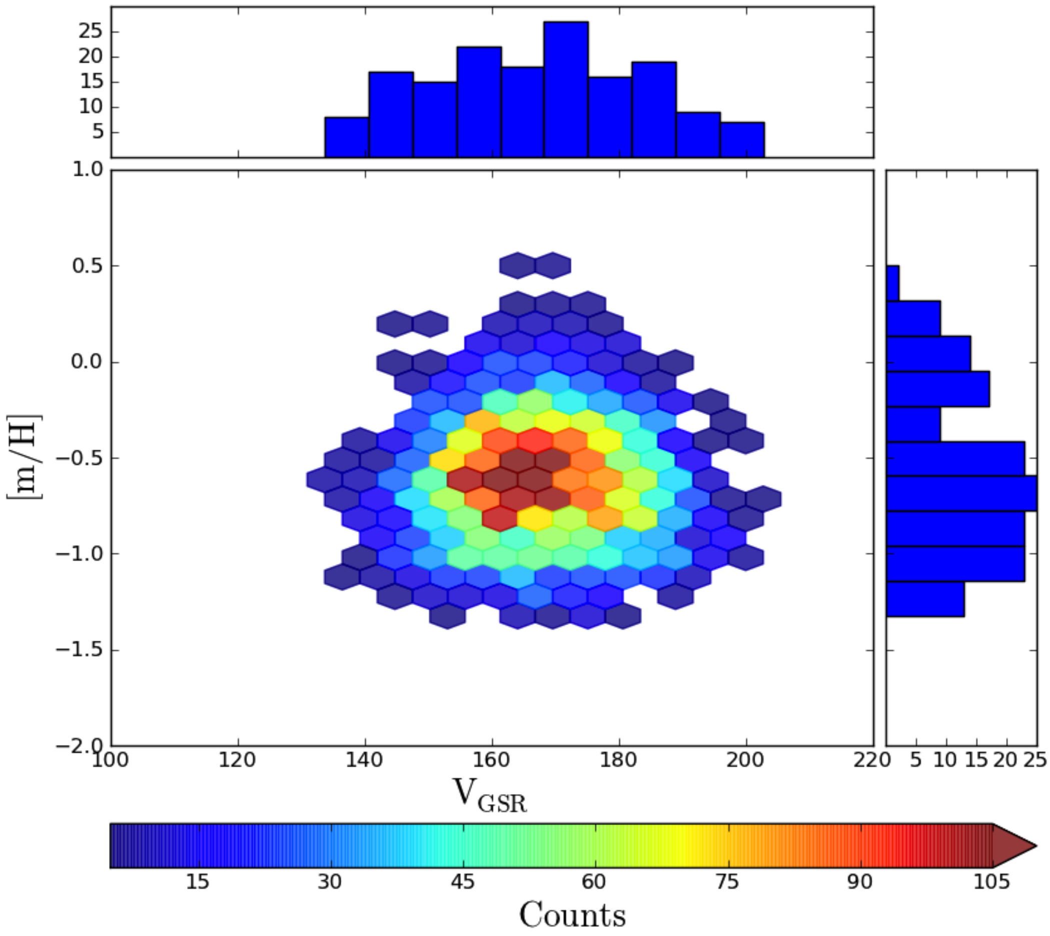

FIGURE 3.15: Hexagonally binned images for the R01 population showing the velocity-metallicity relation for the Sgr core. The binning is assigned to correspond to 20 hexagons in the V_{GSR} direction. One dimensional histograms for velocity and metallicity are shown as side panels in x and y respectively.

centre, Bellazzini et al. (2008) found a mean metallicity of [Fe/H]$\simeq -0.45$ dex and a dispersion of 0.28 dex, which agrees with the increased mean metallicity values we see in the centres of Figure 3.11 and 3.15. For the core, the most recent update of the McConnachie (2012) compilation uses [Fe/H]$= -0.4 \pm 0.2$ (Chou et al. 2007). This is slightly higher than the earlier value of [Fe/H]$= -0.5 \pm 0.2$ from Cole (2001), but none of these prior studies have as large a sample size as we do.

From Figure 3.13 we find that the core stars have a mean metallicity of [m/H]$= -0.59$ dex with a variation of $\sigma_{[m/H]} \simeq 0.34$ dex as given in Table 3.1. This is only slightly more metal-poor than the previously measured mean of [Fe/H]$\simeq -0.5$ dex

(Monaco et al. 2005; Keller et al. 2010; Cacciari et al. 2002; Cole 2001) or the value of [Fe/H]$= -0.4 \pm 0.2$ (Chou et al. 2007), from Table 3.1.

When we visually examined our core spectra we noted about 55 stars of [m/H]≤ -2.0 dex in our pre-processed core (R01) data. The RAVE errors on many of these measurements do not pass the selection criteria for this thesis, but the spectra are sorted via a individual *splot* IRAF measurement of the Ca II 8500 Å triplet spectral lines. We calibrate those to a metallicity measurement with the Starkenburg et al. (2013) relation as discussed in Chapter 2. Thirty of these have velocities and positions matching the central region of the Sgr dwarf (within $\sim 6°$ of the core), and these intriguing objects are part of an ongoing proposal for follow-up (Hyde et al. 2012).

The number of candidate metal-poor objects in the core supports the findings of Casey et al. (2012a), which suggest that the stellar population may be more metal-poor than was previously thought. As stated earlier, in this work we are disregarding any poor fits to the RAVE templates. This means many potentially very low-metallicity stars are excluded from this analysis, as they cannot be measured by the automated routines we use. This would have a minimal effect on the peak of the MDF in Figure 3.13, but would extend the tail further into the extremely-metal-poor regime.

The velocity distribution in the core region is shown in Figure 3.14. We find a peak position which is roughly consistent with what has been measured previously. We know from Table 3.1 that the velocity has been measured previously at $\mathrm{V_{GSR}} \simeq 168.4$ km s^{-1} (converted from the $\mathrm{V}_{helio} = 139.4$ km s^{-1} of Bellazzini et al. 2008). The velocity we find from our measurements is $\mathrm{V_{GSR}} = 168.76$ km s^{-1} with a scatter of $\sigma^{\mathrm{all}}_{\mathrm{VGSR}} = 12.2$ km s^{-1}. We note that $\sigma^{\mathrm{all}}_{\mathrm{VGSR}}$ is a separate measurement from the average hexagonal bin standard deviation $\sigma^{\mathrm{typ}}_{\mathrm{VGSR}} = 12.7$ km s^{-1} calculated previously.

To quantify the relationship of the metallicity and velocity in the core region, we visualise the data in the metallicity-velocity plot shown in Figure 3.15. We create 20 hexagonal bins along the x-axis of Figure 3.15, similar to the method used for Figures 3.10 and 3.11, but this time in metallicity-velocity space. We plot the histogram distributions of velocity and metallicity along the x and y axis respectively. The colour bar gives the average number of stars in each hexagon. We can see in Figure 3.15 that, although there is a concentration of points near our average value, we have a relatively wide spread in metallicity from -1.5 to 0.5 dex within the velocity range of the Sgr dwarf. This spread is broader than the previous ranges found by Mateo (1998) or Bellazzini et al. (1999a,b); however, our larger sample size is likely to be more representative of the overall stellar population.

3.7 Results

Our investigation of the Sgr R01 region has led to several results. We find a potential detection of M54 in the centre of the Sgr dwarf. Signs of an M54 signature (1-6 stars) are detected out to its previously measured extent of $0.06°$ from the centre. This detection is overwhelmed by contribution from Sgr as more stars at larger distances from the centre are included in the distribution. Significant contamination by M54 in our main R01 sample is therefore unlikely.

The average metallicity is likely higher within the region $2°$ from the centre of the Sgr core, but the overlapping MDFs of the inner and outer regions make for a large uncertainty in our measurements. The concentration of more metal-rich stars in the centre of the Sgr dwarf is significant at a 40% level. A higher core metallicity is a property found for some, but not all, other dwarf spheroidals in the Local Group (Koch et al. 2006; Harbeck et al. 2001). On average we find a more metal-poor population with a potentially lower metallicity outer region to the Sgr dwarf shown in Figure 3.11.

The mean R01 metallicity distribution (listed in Table 3.1) is $\langle[\mathrm{Fe/H}]\rangle \simeq \langle[\mathrm{m/H}]\rangle \simeq -0.59$ dex with a standard deviation of $\sigma_{[\mathrm{m/H}]} \simeq 0.34$ dex. This is lower than the previously measured $[\mathrm{Fe/H}] = -0.4 \pm 0.2$ dex of Chou et al. (2007) though it is in good agreement with the earlier value of $[\mathrm{Fe/H}] = -0.5 \pm 0.2$ from Cole (2001). We note that none of the previous studies have as large of a sample size as we do.

For R01 we find a mean velocity (listed in Table 3.1) of $\mathrm{V_{GSR}}$=168.76 km s^{-1} with a variation of $\sigma^{\mathrm{all}}_{\mathrm{VGSR}} = 12.2$ km s^{-1}. Using hexagonal binning the sum of the standard deviations in each hexagon divided by the number of hexagons gives a typical velocity standard deviation of $\sigma^{\rm typ}_{\rm VGSR} = 12.7$ km s^{-1}. The overall spatial velocity distribution of R01 in Figure 3.10 is a good match to the pressure-supported model (Peñarrubia et al. 2011) shown in Figure 3.2. Our data show a $V_{\rm GSR}$ gradient from about 156 to 170 km s^{-1} from east to west in the RA direction. This is consistent with a gradient of $\sim$ 15 km s^{-1} as expected from Peñarrubia et al. (2011).

"In this galaxy there's a mathematical probability of three million Earth-type planets. And in the universe, three million million galaxies like this. And in all that, and perhaps more...only one of each of us."

-Dr. McCoy, Star Trek, Balance of Terror'

4 Observations and Analysis of the Sagittarius Stream

Outside the core region of Sgr discussed in Chapter 3, the density of Sgr member stars drops sharply. We know the approximate position of the stream on the sky as mapped by Majewski et al. (2003), but specific member stars are not known on large scales. It is expected that $> 75\%$ of M and K-giants will be Sgr stars in the high latitude part of the smooth halo (Majewski et al. 2003), and, as in the core region, we selected a range of M and K-giants from 2MASS data for each of the stream regions we observe. To determine which are likely to be true members of Sgr we cannot use velocity and metallicity information as we did in the core region, as we expect the stream to have a range of velocities which occasionally overlap with the distributions we would expect for smooth Milky Way halo stars.

To map the position and determine the properties of the Sgr stream we observed several pointings across the sky and developed a new selection technique to extract likely Sgr members from the data.[1] These stream stars were selected with photometry which corresponded to a range of visual magnitudes $V \sim 12 - 18$ as discussed in Chapter 1. This increases the number of stars available in the stream, although it is still a very sparsely populated region.

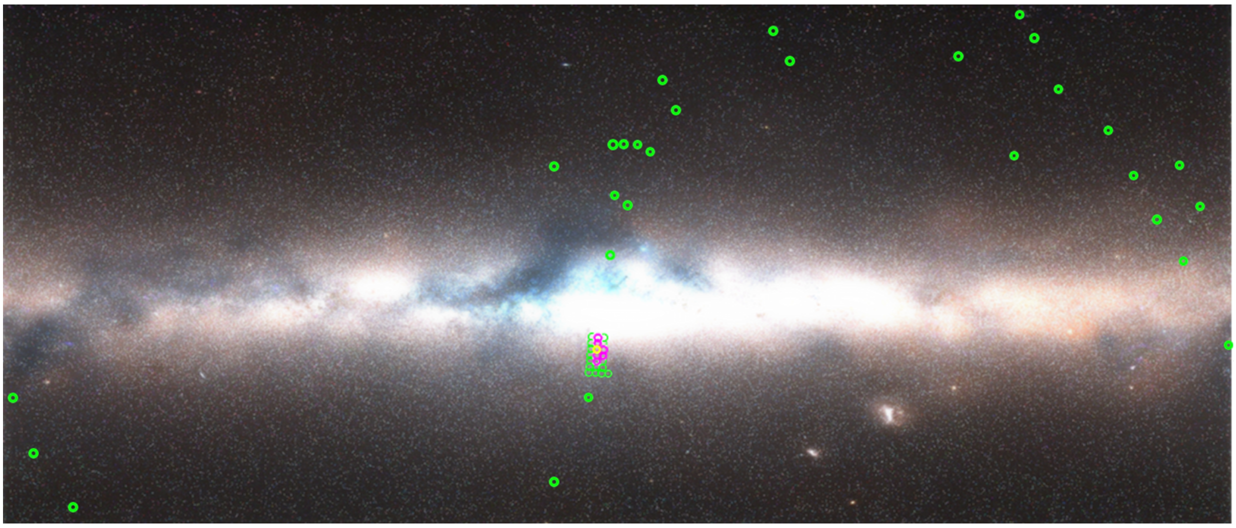

FIGURE 4.1: Sgr dwarf observations on the sky. Each pointing is 2 degrees in diameter. The centre of the Sgr dwarf is located in the yellow circle and the central rectangular block makes up our 'central region'. This is Region 01 from Chapter 3. The magenta circles are the Core 1 observations, used to show no rotation in the core of Sgr (Peñarrubia et al. 2011). Background Milky Way image constructed from online data (Mellinger 2009).

As mentioned in Chapter 1, tidal streams can help us to probe the dark matter halo around the Milky Way (Ibata et al. 2001) and determine not only its general shape, but also its distribution. Some of the first central density models for Sgr show that a constant density dark matter halo for Sgr is consistent with its survival to present day (Ibata et al. 1997). The question of whether or not the halo of the Milky Way might be lumpy or smooth was brought up by Ibata et al. (2002a), who showed that a spherical gravitational potential would suggest dark matter halo substructures. A

[1]Portions of this section were presented at the Winter 2013 meeting of the American Astronomical Society (Hyde et al. 2013), and the general stream description was given as part of the published proceedings (Hyde et al. 2012).

test for halo substructures based on observations of stellar streams was consequently proposed by Ibata et al. (2002b), as tidal tails are predicted to be sensitive to heating by interaction with sub-halos. This idea was followed up by Majewski et al. (2003), and Majewski et al. (2004), who used Sgr stream debris to provide an upper limit on heating by a lumpy Milky Way halo.

While the Milky Way dark matter halo shape was favoured to be either oblate or prolate by the simulations of Law et al. (2005), the oblate halo is modelled by Johnston et al. (2005), who rule out flattening in the Galactic potential at a 3σ level. For comparison with our data, we will consider spherical, prolate and oblate models from Law et al. (2005), as well as the more recent triaxial model from Law & Majewski (2010).

The Sgr stream was kinematically traced in K-giants by Casey et al. (2012a), who found that a triaxial dark matter halo model (Law et al. 2005) for the Milky Way matched their data for the stream better than a spherical model. The triaxial model has since gained further support with data from blue horizontal branch stars in the Sgr stream as traced by Yanny et al. (2009). It was found that observed velocities closely match those predicted in the triaxial model case.

One particular feature that models have had some issue reproducing in the Sgr stream is an apparent bifurcation discovered by Belokurov et al. (2006b). This bifurcated nature of the stream has been confirmed in both hemispheres (Koposov et al. 2012; Slater et al. 2012) and was thought to result from a spherical dark matter halo according to Fellhauer et al. (2006). As noted by Casey et al. (2012a), the bifurcation may not need to be fit to current models if it was caused by some dramatic recent event.

Although there is support for a Milky Way triaxial dark matter halo model, there are still numerous questions to be answered about the progenitor of the stream, in particular its metallicity. The metallicity distribution function (MDF) in the core and stream of Sgr has been mapped in some areas previously, but the areas which show a mixed orbital phase and the gradients in metallicity with distance along the stream still show large uncertainties. The population near the core of Sgr has been found to have a mean value of [Fe/H] ~ -0.5 dex (Cacciari et al. 2002; Bonifacio et al. 2004; Monaco et al. 2005). This value is known to vary as we move out from the core, potentially reflecting the properties of the original progenitor of the dwarf and stream.

As discussed in Chapter 3, after the scenario of the rotating disky progenitor for the Sgr core was shown not to be the case (Peñarrubia et al. 2011), we obtained additional observations from the AAT to further investigate the system. As we expanded our research into the Sgr system, we further developed our data reduction and analysis techniques. The full data set is shown in Figure 4.1 and is comprised of:

- The Sgr core region R01.
- The Sgr Stream, covering 15,000 additional spectra (outside of R01).

This expanded set ranges across the entire sky and includes all the core (see Chapter 3) and stream observations. To determine the properties of this set we will develop a new selection technique to distinguish the likely Sgr members from the smooth halo population of the Milky Way.

4.1 The Sagittarius stream star selection

The low density of stars associated with the Sgr stream necessitates a new selection process for finding likely members. By using the well studied core region as our test area, we should be able to recover the core population by applying the same selection criteria we use on the stream. Selecting the most likely set of Sgr core and stream member stars is a several step process. We start with the 2MASS colour cuts when selecting stars for observation. Then we exclude processed RAVE data results with any null or anomalous calcium line measurements. We use the quality selection on the RAVE correlation coefficient Rcoeff ≥ 15, and visually inspect the residual spectrum (the difference between the reduced spectrum and the RAVE fit). This process allows for only stars which return a reliable spectrum fit to be passed through.

The number of stars and observed per pointing varies substantially. For the stream selection we divide the data up into 30 regions across the sky. As mentioned previously, the entire core area from Chapter 3 is our first region, R01. The remaining pointings are divided into regions R02 to R30. The locations of these regions are labeled at the top of Figure 4.6 (1-30). We choose spatial areas of a few degrees across (many consisting of single observations) for the stream to increase the sensitivity to local variations in the properties of the stream.

In the entire set of AAT observations (currently ∼24,110 individual stellar spectra), there are 9,086 stars observed in the R01 region. The Sgr candidate stars are selected from the modified RAVE pipeline log(g) and $T_{\rm eff}$ values. The selected and processed stars are then used to calculate the highest probability members of Sgr.

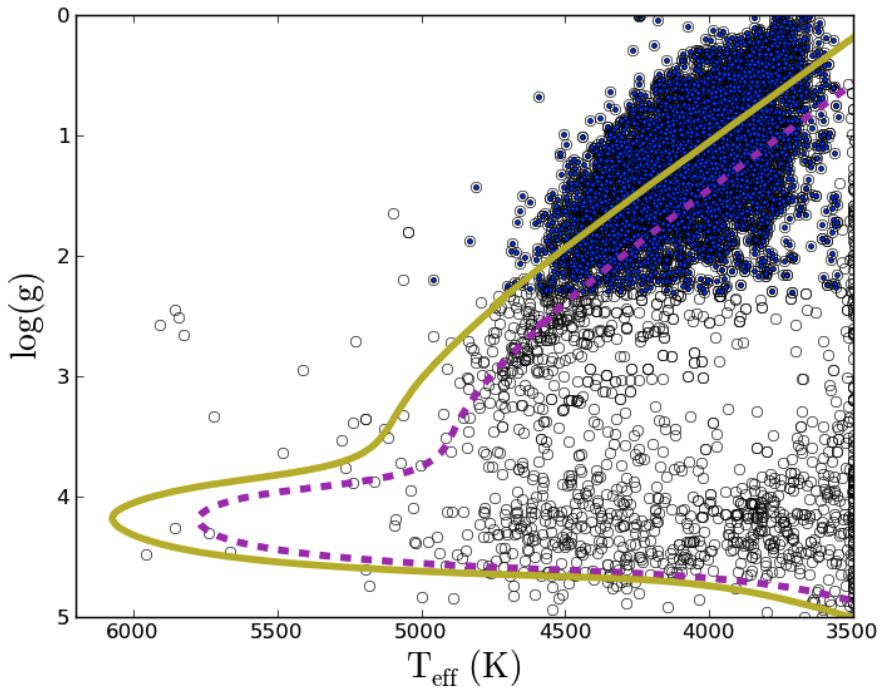

FIGURE 4.2: The color cuts in log(g) and $T_{\rm eff}$ for R01. The filled circles represent the selected stars. The Dartmouth isochrones (Dotter et al. 2008) shown are a 10 Gyr isochrone at [Fe/H] = 0.0, as the dashed line, and a 10 Gyr isochrone at [Fe/H] = −0.5, as the solid line. Open circles are the stars before selection

Using R01 as an example case, we show in Figure 4.2 the selection for M and K-giants on a colour-magnitude diagram. To select M and K-giants we require that: $\log(g) \leq 2.3$ and $3500 \leq T_{\rm eff} \leq 5000$. In R01 this selection returns 6,227 (blue points) from the 9,086 candidate (black circles) stars in R01. The Dartmouth isochrones for

[Fe/H] = 0 (dashed) and −0.5 (solid) metallicities (Dotter et al. 2008) are overplotted in Figure 4.2 for reference. These selected 6,227 stars represent the candidate sample for R01. Applying the same parameter cuts for all the stream stars, we are left with 809 stream candidates, giving a total of 7,036 stars for which we will assess the membership probability (using the distribution functions of Equation 4.1 in Section 4.1.1). We note that the pileup of stars seen near $T_{eff} \sim 3500$ K in Figure 4.2 is an artefact of the modified RAVE pipeline, and they are excluded based on their RAVE correlation coefficients.

For coordinates in this thesis we use the Sgr coordinate system Λ, B as defined by Majewski et al. (2003). In this system, the Sgr core is placed at the origin, and oriented so that the Sgr stream system has its axis along the spatial direction. This flattens the system along the sky, placing the stream parallel to the x-axis.

4.1.1 Membership probability

After excluding all but the best candidates, it is still possible that the stars we have captured may be members of our own Milky Way halo rather than the desired Sgr stream stars. To identify Sgr stars in our sample we look for velocity substructure as deviation from the Galactic halo.

We use generalised Gaussian histograms to compare the data to the smooth Galactic halo, and to define a probability selection for Sgr members in our regions (R01 to R30). The objects we consider are pre-selected to be likely M and K-giants, based on log(g) and T_{eff} criteria as described previously.

First we calculate the generalised Gaussian histogram of the velocity distribution of the objects in each of the 30 regions. For each of our 30 regions, we consider the range of velocity between -400 and 400 km s^{-1}. Dividing that range into 100 bins we calculate the distribution:

$$D_{reg} = \sum_{i}^{N} D[i] = \frac{1}{(\sigma \times \sqrt{2\pi})} \times e^{-(x-\mu)^2/(2\sigma^2)} \tag{4.1}$$

over all bins, where i is each measurement V_{GSR} for each star in the region in question. The value μ is given by each measurement of Galactocentric velocity (V_{GSR})

in the region. N is the number of stars in the region. The value of σ is the error associated with the velocity measurements. The candidate distribution for each region is $D_{reg} = D_{R01}, ...D_{R30} = D_{cand}$ using $\sigma = V_{err} = 2.7$ km s^{-1} and $\mu = V_{GSR}$. This produces the red velocity distributions shown in Figure 4.3.

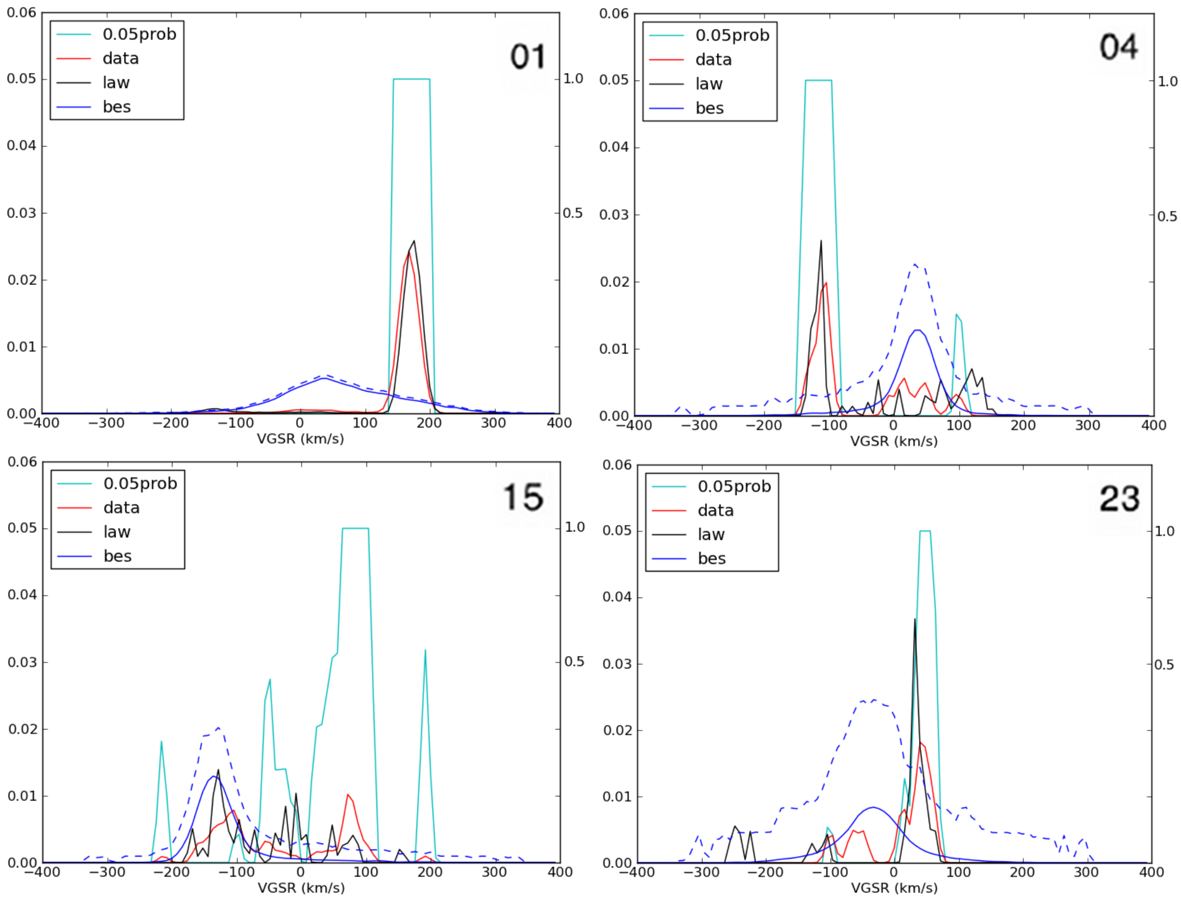

Figure 4.3: The Sgr membership probability calculations for regions R01, R04, R15 and R23 are shown in light blue (scaled to 0.05% to be visible on the same plot as the individual distributions). Red is the generalised Gaussian histogram for our velocity data in the region. The scaled counts axis gives the amplitude of the distribution. Dark blue shows the expected velocity distribution from the Galaxy based on the Besançon model (Robin et al. 2003). The top dark blue dotted line marks the confidence level (C_{bes}) cutoff for membership to the dark blue distribution (the smooth Galactic halo). Black is the expected velocity distribution for Sgr in the region based on Law & Majewski (2010) (online data from Law 2012). The measurement of the likelihood is given as the thin light blue colored line, this is the scaled likelihood value P (scaled to be visible in the same plot, where $P=0.05P_{NotHalo}$).

To compare our observations to the expected background of the smooth Galactic halo, we use the Besançon model velocities (Robin et al. 2003) with Equation 4.1 to calculate a smooth halo generalised Gaussian histogram (D_B). The value of $\mu = V_{vbc}$, where V_{vbc} is V_{GSR} predicted by the Besançon Galaxy model (Robin et al. 2003). When using the Besançon Galaxy model we select each region based on the center coordinates of our fields R01 to R30. We select stellar types to include M and K giants, and bright giants with the default parameters to represent the smooth Galactic halo. We use $\sigma = 2.7$ km s^{-1} to match our measured velocity errors in Chapter 2. By setting the same velocity range and number of bins as in the case of our data distribution we then sample the same number of points as present in the data, but multiple times. This gives us D_B, the blue curve in Figure 4.3, and provides us a normalised and representative halo distribution which we can compare directly to our data distribution in red.

We expect that Sgr stream stars will have a velocity distribution that is not consistent with the smooth Galactic halo. Hence, we only consider stars which are not probable smooth halo members in our Sgr selection. To do this we first calculate which observed stars lie within the D_B distribution of the smooth halo, and find which are likely Galactic halo members. We then choose only objects which are '*not*' smooth halo stars for our Sgr selection.

To calculate whether a star is a likely member of the smooth halo (as modelled by Besançon), we compare D_B with the D_{reg} (the generalised Gaussian histogram of the data) as shown in Figure 4.3. Also shown in Figure 4.3 is the expected velocity distribution from the triaxial model for the Sgr stream (Law 2012) as a black line. The black distribution is drawn from the model points corresponding to the spatial region spanned (in degrees) by regions 1 - 30 respectively. Each black distribution is the model points in the RA-DEC range of the corresponding region. We also require the same binning over velocity range mentioned above to place them on the same scale as the data. This is simply the generalised Gaussian histogram of the model points which lie within the region in question, i.e., for R01 this would be the model points within $\sim 6°$ of the Sgr core.

The D_{reg} and D_B distributions are used to calculate the likelihood of a given star in a region *not* being in the smooth halo, and therefore a likely member of the Sgr stream (although we cannot rule out other sources for the stellar substructure, as discussed later). To establish limits on the likelihood we set stars with $D_{reg} \leq D_B$ to have a $P_{NotHalo} = 0$ and likewise if $D_B \leq 0.001$ we let $P_{NotHalo} = 1$. In the region where $D_{reg} \geq D_B$ then we need to consider the difference in the distributions. To keep an accurate scale of likelihood between zero and one we will set a confidence level which can be used as a cut off in the region where $D_{reg} \geq D_B$.

The limits for selecting smooth halo stars and '*not*' Sgr candidates are set by the confidence level in our representation of the Besançon model. The confidence level at which $D_{reg} \geq D_B$ determines the cut off for the smooth halo population and give us a scale of probability between zero and one for stars which are within the confidence level for the Besançon distribution (from the base solid dark blue line to the upper dotted dark blue line in Figure 4.3).

4.1.2 Determination of the confidence level from the Besançon model

For each region, we require an appropriately large sample of simulated data points from the Besançon model for the region in question (the centre of each region corresponds to one model line of sight pointing). The Besançon model is designed to return a smaller number of data points than we need to draw a smooth velocity distribution for most of our regions queried. We create a improved distribution by sampling the model points several times to produce a smooth halo distribution for each of our regions. To determine the standard distribution for each Besançon region (corresponding to R01 through R30) we draw the Besançon distribution several times using the same sample number of points as are present in the data (the red distribution) as shown in Figure 4.4.

We return the same number of model points as the number of stars in the region to create a sample, drawing that several times creates a smooth Milky Way halo distribution even for sparsely populated regions. Each time we draw our sample corresponds to one iteration. The sampling in the Besançon model is visibly smoother from 100 to 1000 iterations, only 100 are shown in Figure 4.4 for clarity. The sampling does not

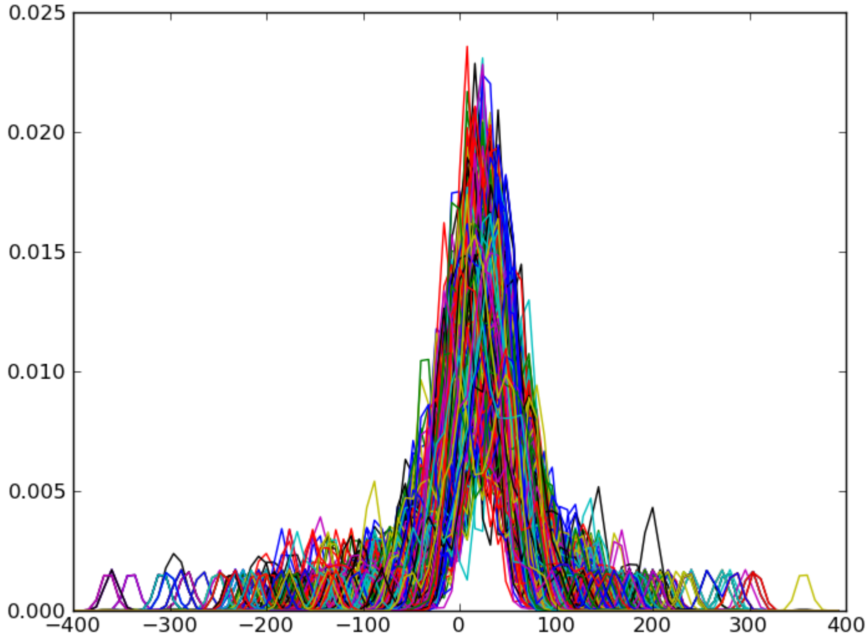

FIGURE 4.4: 100 iterations of the Besançon model (Robin et al. 2003) for one region. As the number of iterations increases the distribution becomes smoother and sets the confidence level (C_{bes}) cutoff for membership to the smooth Galactic halo.

improve notably after 1000 iterations.

A confidence level of C=0.996 corresponds to the level at which 99.6% of the data in the sample lies in 1,000 iterations of sampling the Besançon model for each of the 100 bins in our velocity range. The location of this confidence level gives us the cutoff $C_{bes} = C(0.996)$. We choose this confidence level as it corresponds to a 3σ cutoff for normally distributed data (although we do not assume anything about the distribution a priori). The C_{bes} cutoff is drawn as the dotted blue line in Figure 4.3.

All data in the red (i.e., observed) distribution in Figure 4.3 which exceed C_{bes} (from the Besançon model) are defined to be likely Sgr stars (rather than part of the smooth halo), so if $D_{reg} \geq C_{bes}$ then $P_{NotHalo} = 1$. To establish limits on the probability, we set stars with $D_{reg} \leq D_B$ to have a $P_{NotHalo} = 0$ (i.e., no contribution from the smooth halo is included) and similarly if $D_B \leq 0.001$, we set $P_{NotHalo} = 1$. In the regime where $D_{reg} \geq D_B$, but is still less than C_{bes}, then we need to consider the difference in the distributions. If $D_{reg} > D_B$ and $D_{reg} \leq C_{bes}$ we use:

$$P_{NotHalo} = \left[\frac{D_{reg}}{D_B} - 1 \right] / (C_{bes}/D_B) \tag{4.2}$$

to calculate the likelihood. This gives us a smooth linear trend between the $P_{NotHalo} = 0$ (P0) and $P_{NotHalo} = 1$ (P1) limits. The total $P_{NotHalo}$ is shown scaled to 0.05% (the light blue curve) so that it is in the same range as the data from the Besançon model, D_B, and the Sgr data, D_{cand}, as shown in Figure 4.3. Combining results from all of our regions we find a total of 5513 core R01 candidates and 106 stream candidates, a total of 5619 possible Sgr members. The metallicities for the 106 P1 stream stars are given in Appendix A.1 and the routine to calculate them is given in Appendix A.3. We note that although we assume Sgr membership this may not be the case for all objects, as discussed further in Section 4.3.2.

4.1.3 Probabilities around the Sgr core

The globular cluster M54 is near the centre of the Sgr dwarf, but as discussed in detail in Chapter 3, the R01 region is much greater in extent. The area spans a box twenty degrees wide centred on the Sgr dwarf as shown in Figure 4.1. This region has an advantage over the Sgr stream, namely that the Sgr objects near the core are more readily separated in both position and velocity. Using only the core (R01) we can test the applicability of the probability selection to the core Sgr population as defined by its grouping in velocity and spatial coordinates.

As previously noted, after quality cuts for the modified RAVE pipeline, 7,036 M and K-giants are detected. Out of these stars 6,227 are in R01 (this is the number of stars in R01 or '#R01'). Applying Equation 4.1 and Equation 4.2 we recover 5,513 P1 stars in R01 (the number of P1 stars in R01 or '#R01P1').

In R01 we use the stellar velocities as well as the probability of being part of the Besançon smooth halo distribution to identify likely Sgr members. From Chapter 3 the velocity of the core falls within a heliocentric velocity range of 100 to 200 km s^{-1}. The number of core stars belonging to this velocity range (5,408) make up the population $\#R01_{vSgr}$. The set of core stars with a non-halo likelihood of P1 and belonging to the velocity range for Sgr are then given by $\#\mathrm{R01P1}_{\mathrm{vSgr}}$.

We will use the velocity range to compare the number of stars in the R01 population (#R01) to the number of stars selected with a likelihood of P1 (#R01P1). We find that the ratio of the number of R01 stars at the known Sgr velocity in the case of the R01 population is $\#\mathrm{R01}_{\mathrm{vSgr}}/\#\mathrm{R01} \simeq 93.3\%$. When we constrain ourselves to only the P1 (#R01P1) population of we get $\#\mathrm{R01P1}_{\mathrm{vSgr}}/\#\mathrm{R01P1} = 100\%$. The P1 criterion thus gives a selection of stars for the core which agree with the Sgr velocity range to 100%.

Using the P1 probability gives a clean selection of Sgr stars in R01. It is also possible to select lower (i.e., more inclusive) probabilities. In R01 we find that there is the same number of stars selected at $P \geq 0.2$ and $P=1$, because the probability distribution has a steep break from the smooth halo. This is a direct result of the large number of stars observed in the core. Unfortunately the Sgr stream regions have a much smaller number of stars observed, and in some cases, overlap with the expected smooth halo (Besançon) distribution. This is visible in Figure 4.3, where we have proportionally higher values of C_{bes} in region 23 (R23) as compared to R01. Lowering the probability cutoff increases the number of stars selected in the stream: if we use $P \geq 0.2$ we get 330 stream objects. However, this results in a less precise set of candidates in the stream. It is the primary set of 106 P1 stars which we will use in Section 4.3.2 to look for overdensities or 'clumping' in our data.

4.2 Comparison of models to our data for the Sagittarius stream

As mentioned previously, the shape of the Milky Way dark matter halo shape can be constrained by the properties of streams in the halo, in particular the Sgr stream which completely encircles the Galaxy. Here we compare the four main models of Law (2012) to the P1 selection of the Sgr stream. These four models are generated with triaxial, spherical, prolate, and oblate Milky Way dark matter haloes respectively. The

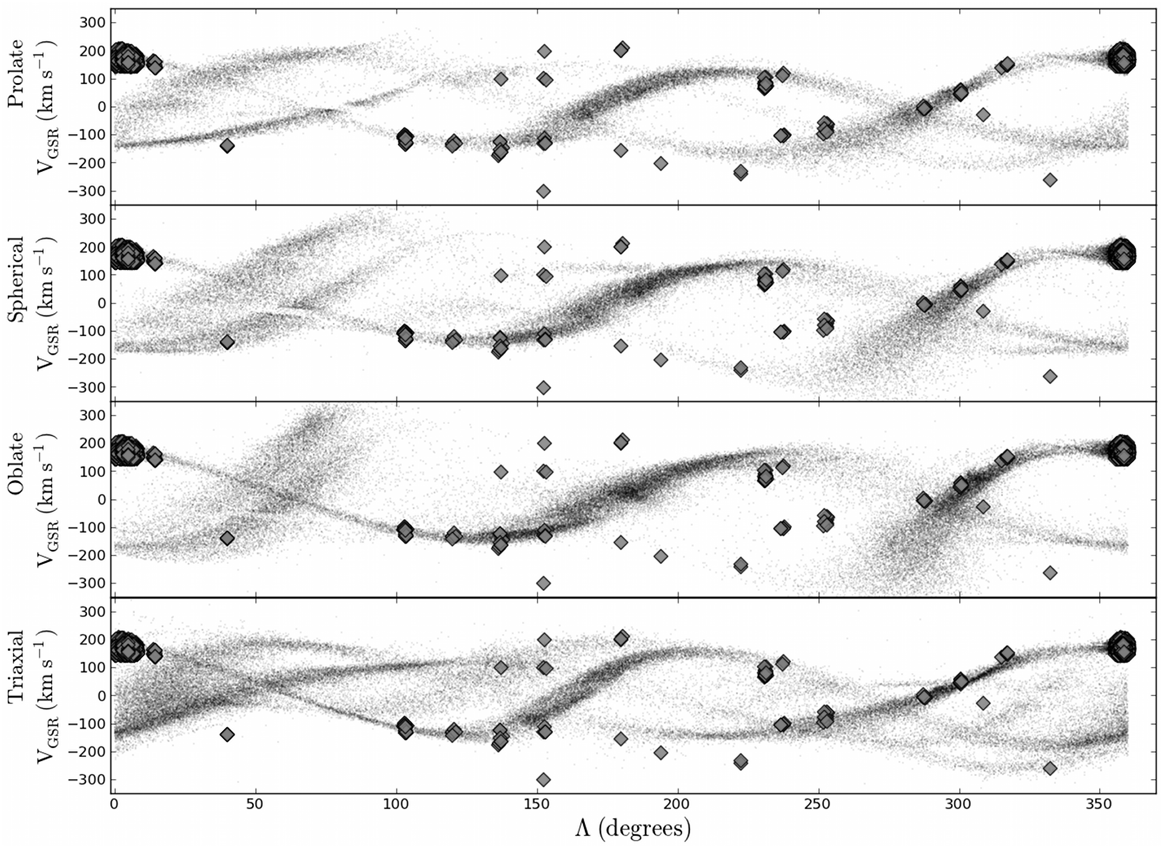

Figure 4.5: Comparison between our P1 data (diamonds) and the spherical, prolate and oblate models from Law et al. (2005) as well as the triaxial model from Law & Majewski (2010). Both leading and trailing arm P1 debris kinematically overlap with the models. The prolate and triaxial models provides a better correspondence to the cluster of P1 points at $\Lambda \simeq 250°$.

spherical, prolate and oblate models were discussed in Law et al. (2005) whereas the more recent triaxial model is from Law & Majewski (2010).

Mapping the P1 stars returned by our selection technique, we find that the leading arm of Sgr (known to be particularly sensitive both kinematically and spatially to the shape of the Milky Way dark matter halo, Law & Majewski (2010)) overlaps with both the triaxial and prolate models in velocity space, as shown in Figure 4.5. All four models show agreement in velocity as they pass through or near P1 points but only the prolate and triaxial models show agreement in the $\Lambda, V_{GSR} \simeq (250°, -200 \text{ km s}^{-1})$ region where we have a large number of high likelihood P1 Sgr stars.

The triaxial model appears to be a better match to our P1 data at the highest cluster of modelled points in the regions set by $\Lambda \sim 200° - 350°$, although the point at $\Lambda \sim 40°$ in Figure 4.5 is better fit in the prolate, spherical, and oblate cases. We find that both leading and trailing arm debris seems to kinematically match the triaxial model overall but with discrepancies in some locations. In particular we note the P1 points at $\Lambda, \mathrm{V_{GSR}} \simeq (39.74°, -139.6 \text{ km s}^{-1})$ and $\Lambda, \mathrm{V_{GSR}} \simeq (152.3°, -300.8 \text{ km s}^{-1})$ do not seem to fit the triaxial model well, although we cannot rule out that they might be statistical outliers, or that they might represent halo substructure unrelated to the Sgr stream.

Figure 4.5 shows that, in the range from $\Lambda \sim 200 - 300°$, the triaxial and prolate models more closely line up with the P1 Sgr members than the oblate or spherical models. The more recent triaxial model matches the point at $\Lambda, \mathrm{B} \simeq (332.4°, -260.9°)$ (which is not well fit by the other models), as well as the average points for the leading and trailing arms. Although there are discrepancies found between our data and all four of the models, in general, the triaxial dark matter halo provides a reasonable fit to the observations across the sky. Although it is known that the triaxial model does not reproduce the bifurcation in the Sgr stream (Belokurov et al. 2006b) we consider it to be the best of these four options.

As mentioned previously this bifurcation may have resulted from a kinematic disruption of some kind, but if the bifurcation was caused by some more recent event then there would be no need to account for the bifurcation feature in formational models of the stream (Casey et al. 2012a). The triaxial model seems to match both leading and trailing arm observations kinematically, and as it is the most recent of the models we are considering, we use it as a point of comparison for our data in the stream. We show the full set of P1 coordinates and velocities as well as comparisons to other observations as well as the triaxial model in Figure 4.6.

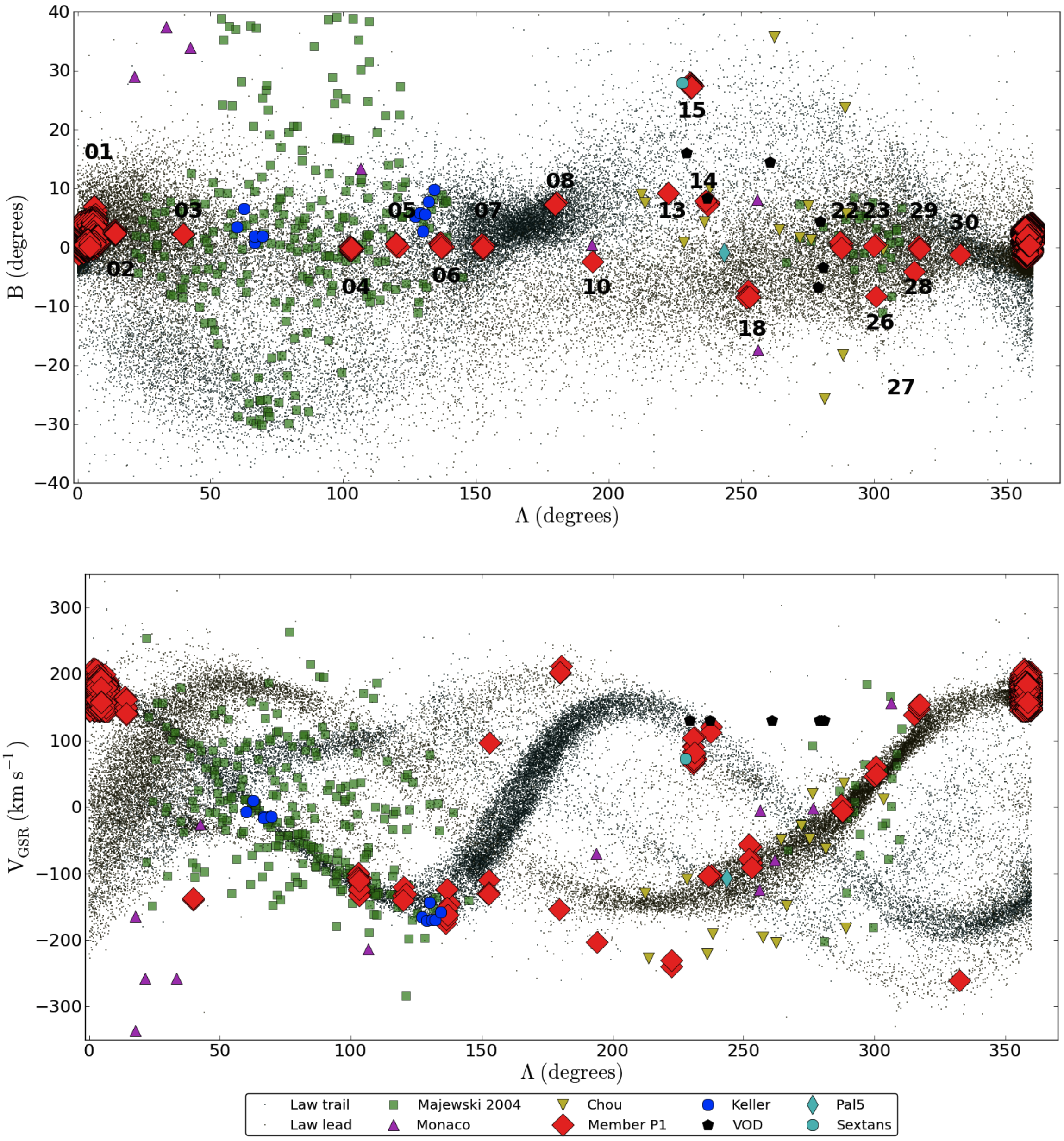

Figure 4.6: The distribution of the highest likelihood Sgr stars. P1 stars are shown as large red diamonds. Top is the region numbering used in the likelihood calculations, starting at the core (R01) and going to stream region 30. For comparison we show the data from Majewski et al. (2004) as squares, the data from Keller et al. (2010) as circles, Monaco et al. (2007) as upwards triangles, and data from Chou et al. (2007) as downwards triangles. The triaxial model of Law & Majewski (2010) is given by the very small dots (online data from Law (2012)). The trailing arm starts at a velocity of about 180 km s^{-1} at $\Lambda = 0$ and goes down to a velocity of about -150 km s^{-1} at 360 degrees, whereas the leading arm starts at -150 km s^{-1} at $\Lambda = 0$ and goes up to 180 km s^{-1}. Other halo substructures, the Virgo Overdensity (VOD), the Sextans dwarf and Pal5 are marked for reference.

4.3 Discussion

As shown in Figure 4.3 we have a range of calculated likelihood values that go from zero to one. The highest likelihood objects are $P_{\mathrm{NotHalo}} = 1$ (P1) stars, which give us a total of 5,619 very high likelihood Sgr members, 106 of which are in the stream (i.e. not in R01). The P1 selection includes only those stars which lay on or outside of the C_{bes} dotted blue line shown in Figure 4.3.

We find that 100% of the P1 stars selected in the R01 region lie within the known velocity range for the Sgr dwarf, i.e. within a range of heliocentric velocity of 100 to 200 km s^{-1}. This range is chosen based on the radial velocity profile of the core to within 3σ (from Bellazzini et al. (2008) $V_{core} = 139.4 \pm 0.6$ km s^{-1}). Including all Sgr candidates for R01 we find 93.3% of the stars are within the velocity range for Sgr. The P1 selection then gives us zero halo objects in the well known Sgr core region, without assuming anything other than they not part of the smooth Milky Way halo. We use these P1 stars to trace likely Sgr members in the stream where the velocity distribution is less well known. The spatial and velocity distribution of Sgr P1 data is compared to the triaxial model of Law & Majewski (2010) in Figure 4.6. The stream of Sgr has been extensively mapped in the literature and we choose several illustrative examples to compare to our P1 stars. We elect to show the positions and velocities observed for the stream from Majewski et al. (2004), Keller et al. (2010), Monaco et al. (2007), Chou et al. (2007) as they cover similar regions and, in the case of Majewski et al. (2004), start from nearly identical selection criteria.

There are 106 P1 stream members shown in Figure 4.6. The P1 data show that the distribution of Sgr stars in the core and stream roughly agree with triaxial model of Law et al. (2005). In both leading and trailing arm regions of the model there is a general consistency in velocity space. The discrepancy between data and models could be due with problems in the models or with the small number statistics, i.e. the low density of P1 stars in the stream.

The Law & Majewski (2010) model assuming a triaxial halo does not reproduce the apparent bifurcation in the Sgr stream (Belokurov et al. 2006b). As postulated recently by Casey et al. (2012a), this bifurcation may have resulted from a kinematic disruption of some kind, but if the bifurcation was caused by some more recent event, then there would be no need to account for this feature in formational models of the stream. The full set of probabilities and velocities, as well as comparisons to other observations in the case of the triaxial model are shown in Figure 4.6.

Although the apparently bifurcated nature of the stream has been recently confirmed in the south as well as the north (Koposov et al. 2012; Slater et al. 2012), other properties of the stream remain more difficult to pin down. In particular Koposov et al. (2012) speculate that the bifurcation itself could be due to infall of two satellites, Sgr and a companion, with each branch of the bifurcation arising from a different progenitor.

There is some disagreement currently in the literature about to what extent the measured properties of the Sgr stream agree with models. From Slater et al. (2012), distances to the bright arm of the stream agree well with the models of Law & Majewski (2010). However, according to the RR Lyrae measurements of Drake et al. (2012), there are some significant differences between measured and predicted distances in the stream. In Figure 4.6 we see that for the leading arm of the triaxial model (the small yellow points), the P1 measurements (red) lie close to the highest concentration of modelled values with only a few outliers in the V_{GSR} plot.

The trailing arm seems to be fit less well. There are several points which do not coincide exactly with the model and one of the major groupings of data points that we find lies at a velocity inconsistent with the model. We discuss this is the R15 overdensity further in Section 4.3.2.

4.3.1 The stream metallicity distribution

We note agreement in the P1 stream stars and the triaxial model (listed as ‘Law’) in the bottom panel of Figure 4.6, (Law & Majewski 2010) in velocity space. Though there are a few interesting discrepancies (these may be due to other unknown overdensities or kinematic substructure as discussed in Section 4.3.2) the expectation is that the majority of P1 stars will be Sgr members.

The largest discrepancies between the data and the triaxial model lie in the region $\Lambda \sim 150^\circ - 250^\circ$ shown in Figure 4.6 and Figure 4.5. The trailing arm starts at a velocity of about 180 km s^{-1} at $\Lambda = 0$ and goes down to a velocity of about -150 km s^{-1} at 360 degrees whereas the leading arm starts at -150 km s^{-1} at $\Lambda = 0$ and goes up to 180 km s^{-1}. The areas with the highest density of P1 stars show a good correspondence with the model but the mis-matches indicate that there is more work to be done in particular in fitting the trailing arm. Towards that end we investigate the metallicity distribution from the core and across the stream.

We find the average metallicity of core (R01) P1 stars to be -0.59 dex with a dispersion of $\sigma \simeq 0.34$ dex. Although this is only slightly more metal poor than the previously measured mean of [Fe/H]$\simeq -0.5$ dex (Monaco et al. 2005; Keller et al. 2010; Cacciari et al. 2002), we expect that the metal poor tail will extend quite a bit lower and indeed may even go into the extremely metal poor (EMP) range as discussed in Section 3.6.

If our 30 potentially extremely metal poor Sgr objects described in Chapter 3 can be confirmed with high resolution spectroscopy, this number of metal poor objects in R01 would support the findings of Casey et al. (2012a) who indicates that the distribution in the core of Sgr may be more metal poor than was previously thought. As stated previously, for this study we disregard any poor fits to the RAVE templates. This means many of the very lowest metallicities fall out of the reduction as they are not measurable by the automated routines we used.

To investigate the leading and trailing arm of the stream we select arm stars that are coincident with the triaxial model in the Λ, B, and V_{GSR} coordinates. We also require that the stars not be in an overlapping region, i.e. areas of the model where both leading and trailing stars are predicted to lie. In Figure 4.7 we show the bins containing only P1 points. Law et al. (2005) indicates that along the leading arm of the stream, stars which are lost from Sgr in different orbits around the Milky Way can overlap in orbital phase position. As mentioned by Chou et al. (2007); Keller et al. (2010) the longer trailing arm yields better energy sorting of the debris and can be more cleanly isolated from background or mixed populations. To select a clean set for leading and trailing arm populations we choose only stars which do not occupy a mixed phase position and create the leading and trailing population as shown in Figure 4.7.

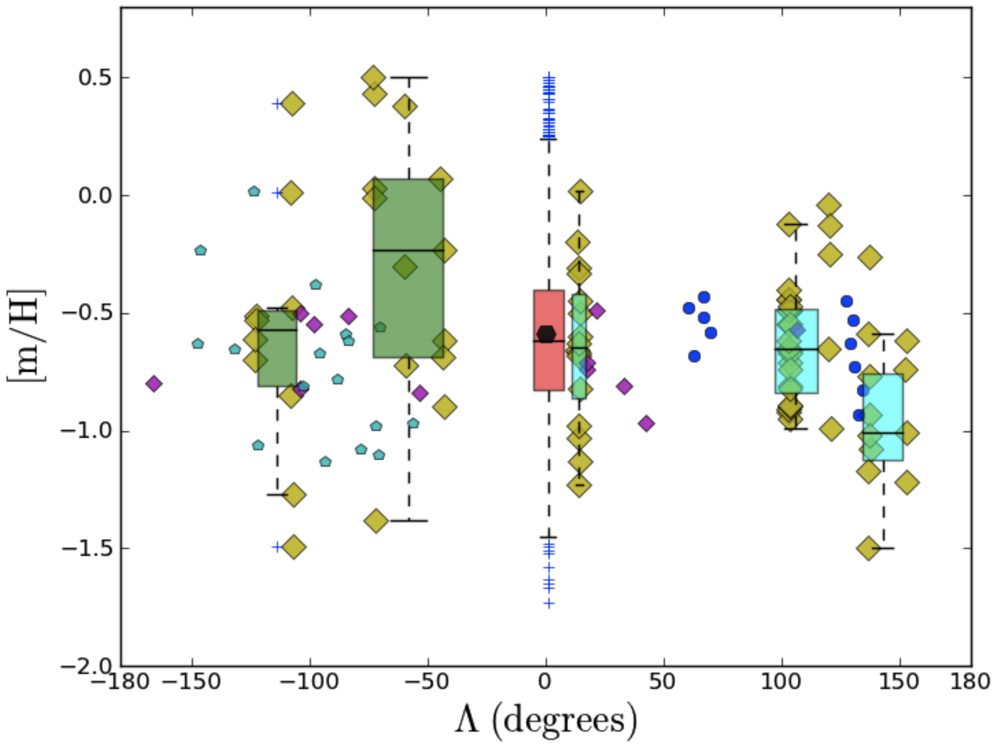

FIGURE 4.7: MDF evolution with Λ for the leading (two negative Λ boxes) and trailing (three positive Λ boxes) Sgr arms. The Sgr core (R01) region is shown by the single boxed area at $\Lambda = 0$. The black line in each box is the median value of metallicity for the area, the 25th percentile is given by the upper edge of the box, the 75th percentile is given by the lower edge of the box and the maximum and minimum are at the ends of the whiskers. Our Sgr points included are shown as yellow diamonds, comparison data are shown from Keller et al. (2010) as small blue circles, Monaco et al. (2007) as magenta diamonds, and Chou et al. (2007) as light blue pentagons. The literature value for the Sgr core is given as the black hexagon at [Fe/H] ~ -0.5 dex (Cacciari et al. 2002; Bonifacio et al. 2004; Monaco et al. 2005).

We create 2 bins for the leading arm (negative Λ) and 3 bins for the trailing arm (positive Λ) along 360 degrees of Λ, placing the Sgr core at $\Lambda = 0$ at the center. These bins are defined to maximize the number of stars included as well as spatial resolution as shown in Figure 4.7. The five stream bins are located at $\Lambda \simeq [-59, -112, 142, 106, 13]$ with a range of $\Lambda_{\rm min} - \Lambda_{\rm max} \simeq [30, 17, 17, 18, 1]$ and $[13, 10, 11, 24, 16]$ stars in each bin respectively. The distributions in metallicity in these bins is shown in Figure

4.7, the median of the bin is given by a horizontal line. The mean metallicity of the five stream bins are $[-0.27, -0.60, -0.97, -0.63, -0.64]$ dex, with MDF dispersions of $[0.55, 0.52, 0.26, 0.24, 0.33]$ dex corresponding to the Λ coordinates above. The core R01 region has a mean metallicity of -0.59 dex and a dispersion of 0.34 dex from our sample of 5513 P1 core stars. The P1 objects which do not exclusively lie within a leading or trailing arm portion of the model are not included in the bins.

We find that the mean metallicity starting from -0.59 dex in the core drops from -0.63 dex to -0.97 dex as Λ increases along the trailing arm in Figure 4.7 (in the positive direction). This is roughly consistent with the metallicity gradient of $-(2.4 \pm 0.3) \times 10^{-3}$ dex/degree gradient seen in the trailing arm metallicity by Keller et al. (2010). Although previous work indicated a gradient in the leading arm as well as the trailing arm of Sgr (Chou et al. 2007; Keller et al. 2010; Carlin 2012; Carlin et al. 2012), in our data we see little or no trend in Λ for the leading arm metallicity. The higher dispersion in the leading arm may be preventing any discernment of trends. Mapping of the arms by Chou et al. (2007) indicates that leading arm stars seem to be more metal poor than the core, although like us, the difference in the mean metallicities of the samples they use is less than their MDF dispersions (0.31 and 0.33 dex respectively).

Chou et al. (2007) find that the MDF of the Sgr stream evolves from a median of [Fe/H]$\simeq -0.4$ dex to about -1.1 dex over a leading arm length, but our mean values do not drop off at that level, staying in the range of [m/H]$\simeq -0.61$ dex to about -0.27 dex. Although the distribution in leading arm stars is known to be quite broad we find that our leading arm stars seem to lack a decrease to metal poor, and do not seem to show more metal poor stars than the trailing arm as mentioned by Chou et al. (2007). The broad range of metallicities in the leading arm has additionally been noted by Casey et al. (2012a). The median metallicity of the Galactic thick disk is ~ -0.7 dex, and as noted by Chou et al. (2007), should not have a large impact on MDF trends across the stream. The trend to lower metallicities in the leading arm of the stream found by Chou et al. (2007) may be due to their slightly more metal rich value for the Sgr core.

The comparison of the Sgr core region with the leading arm does not show the decline in median metallicity which would be represented by debris lost some 3.5 orbits ($\sim 2.5 - 3$ Gyr) ago (Law et al. 2005), but we do find substantial variation in the MDF along the stream. The observed MDF variation supports the theory of Martínez-Delgado et al. (2004), who suggest the satellite shed successive layers in its orbit, over which there could have been an intrinsic MDF gradient. The disagreement in the direction of the trend between our data and that of Chou et al. (2007) indicates that perhaps the variation may be wider, and the gradient less, than either of our samples suggest. This would support a rapid change in the binding energy of Sgr over the past several gigayears, providing a large net metallicity variation, but a shallow gradient. The sudden change of state could have been caused by some dramatic event, which may also provide the source of kinematic disruption invoked by Casey et al. (2012a) to account for the bifurcation seen in the stream.

We additionally find a large MDF variation in the trailing arm sample, as mentioned above. If this region is truly less susceptible to overlap in orbital phase position, then this would indicate evolution in the stream from a mean of -0.63 (near what we find for the core) to -0.97 dex (our most distant trailing arm box). This variation is additionally on the order of the MDF dispersion, but with overall lower dispersion than what is found in the leading arm. We then can conclude that although the dispersion in the leading arm may be due to mixed orbital phase, the trends we find in the leading and trailing arms support a gradient in the Sgr MDF with the stream, and therefore a intrinsic MDF gradient in the progenitor to the Sgr dwarf and stream system we see today.

4.3.2 Overdensities in the stream

In Figure 4.6 we include information for known features (overdensities and streams) that are near the Sgr stream at various points on the sky. While we don't recover any of them in this data set, in our parameter space there are two which have noteworthy overlaps.

Firstly we consider the VOD (Keller 2010). This includes three halo substructures;

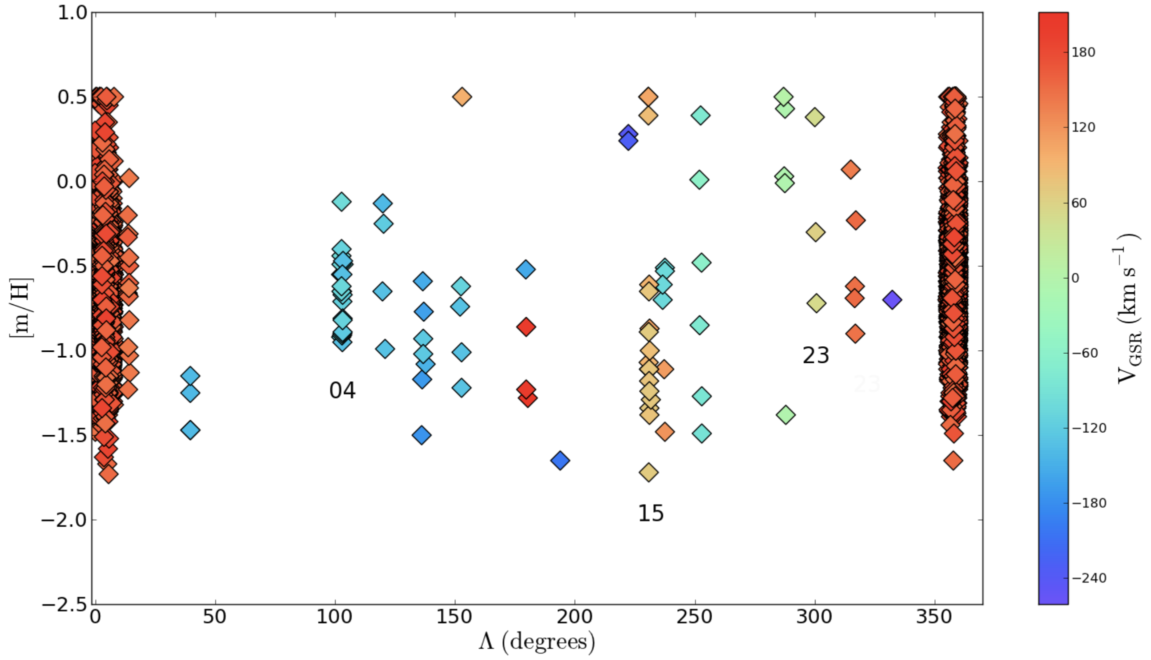

FIGURE 4.8: The metallicity distribution as a function of position along the Sgr stream. We colour code each data point by scaled velocity in V_{GSR} to distinguish the R15 (15) overdensity from the stream and bring out potential new stream features. The main core is clearly visible, and the labeled regions correspond to other overdensities from regions R04, R15 and R23 as listed in Table 4.3.2.

the 160 and 180 degree overdensities (at distances of 17 and 19 kpc respectively and radii of 1.3 and 1.5 kpc respectively) and an extended feature at 28 kpc that covers at least 162 deg^2 (the Virgo Equatorial Stream). We use the coordinates found in Keller (2010) to plot the spatial points and we adopt $V_{GSR} = 130 \pm 10$ km s^{-1} for VOD from Newberg et al. (2007). This gives us the black pentagons shown in the top two sections of Figure 4.6.

The Palomar 5 (Pal5) globular cluster is located at coordinates l, b $\sim (0.85°, 45.86°)$ shown by the light blue diamond. The metallicity is [Fe/H]=−1.41 dex from the Harris Catalogue (2010 edition) (Harris 1996) which is only slightly richer than what we expect for Sgr stars. Pal5 has an extremely low velocity dispersion, it was calculated to have a heliocentric velocity of $v_{hel} = -58.7 \pm 0.2$ km s^{-1} and a total line-of-sight velocity dispersion of 1.1 ± 0.2 km s^{-1} by Odenkirchen et al. (2002). From Equation 2.14 this translates into $V_{GSR} \sim -106.47$ km s^{-1}.

Finally we consider the Sextans dwarf centred on the light blue circle. At coordinates of (RA, Dec) $\simeq$ (10h1.5', -01°22') or (l,b) $\simeq$ (4.2,0.7) it is known to have a Galactocentric velocity of V_{GSR} $\simeq$73 km s^{-1} from Irwin et al. (1990); Irwin & Hatzidimitriou (1995). Sextans members have been measured to have a metallicity of [Fe/H]$= -1.7 \pm 0.25$ dex (Da Costa et al. 1991) which is slightly more metal poor than what we expect for Sgr stars. With a diameter of 30 arcminutes on the sky this large and somewhat diffuse structure is similar to the type of detection we are looking for in the Sgr stream.

Although the structure of Sgr overlaps with these overdensities in several regions it appears to remain well separated when metallicity, velocity, and spatial coordinates are taken into account, except in the case of the Sextans dwarf. The presence of the comparison features above led us to search for additional groupings of stars in our data.

Field	Stars	Λ_{avg}	B_{avg}	RA_{avg}	DEC_{avg}	$[m/H]_{avg}$	σ_{mH}	V_{GSR}(avg)	σ_v	type
		degrees		degrees		dex	dex	(km s^{-1})	(km s^{-1})	
04	23	103.05	-0.22	02.0	-01.9	-0.65	0.2	-112.61	10.90	Sgr Stream
15	17	231.02	27.52	10.2	-01.4	-1.10,+0.48	0.65	79.45	11.49	Sextans
23	3	300.31	0.23	15.0	-06.9	0.38	0.02	50.71	5.39	Sgr Stream
01	5513	154.32	1.65	19.0	-30.8	-0.59	0.34	168.76	12.15	Sgr Core

Table 4.1: The approximate position and velocity of P1 overdensities. These groups correspond only to collections of three or more stars within $\pm$25 km s^{-1} in velocity for an area with a 5 degree radius on the sky. The distribution of all points is given in Figure 4.6.

We searched the P1 data and found 4 sets of data which have stars that are coincident in velocity and spatial coordinates; i.e. within $\pm$ 25 km s^{-1} in velocity for an area with a 5 degree radius on the sky. These sets or 'over dense' regions in the data are located in R01, R04, R23 and R15 as shown in Figure 4.8. The mean properties for each of these overdense regions is listed in Table 4.3.2. While R01, R04, and R23 velocities correspond with what is expected from predictions of the triaxial model, the group of $\sim$ 17 stars from R15 has a large offset with respect to the triaxial model. This detection is well observed in Figure 4.3, where comparison shows little correspondence with the Milky Way smooth halo or the triaxial model for Sagittarius. The peaks for

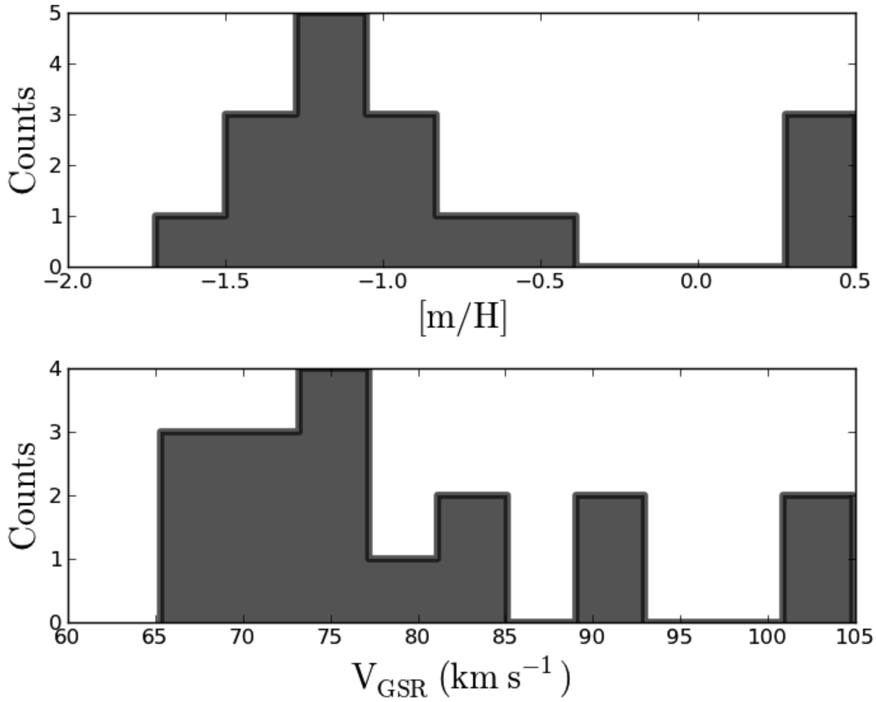

FIGURE 4.9: The top panel shows the MDF for the R15 overdensity, showing a super-solar population as well as a lower metallicity group at [m/H]$\simeq -1.10$ dex. Bottom is shown the velocity distribution for the R15 overdensity, the higher velocity objects do not correspond to the super solar metallicity group. The detection of R15 in gave a velocity range of about 50 km s^{-1} in the heliocentric coordinates, taking only the most likely non-halo candidates, this translates to the above range in V_{GSR}.

the MDF and the velocity distribution of R15 is given in Figure 4.9.

The group of 17 stars in R15 has an average velocity of $V_{GSR} = 79.45$ km s^{-1} (where $\sigma = 11.49$ km s^{-1}) and an average metallicity of $[m/H]_{avg} = -0.83$ (where $\sigma = 0.65$ dex) for a position centered on Λ, B $\simeq (231.02°, 27.52°)$. From Figure 4.9 we note that the MDF seems to be bimodal; however, the three supersolar metallicity values do not reflect a grouping in velocity. The coordinates in ([m/H],V_{GSR}) are (+0.39,83.79), (+0.5,65.31), and (+0.5,103.94) and removing them from our distribution will shift the mean metallicity to [m/H]$\simeq -1.10$ dex but will have almost no effect on the average velocity.

The R15 group is near the spatial coordinates of three of our overdensities, namely the VOD, Pal5 and the Sextans dwarf. However, the velocity measured corresponds closely only with Sextans. As mentioned previously, we expect a value of approximately

73 km s^{-1} from the literature for Sextans, and we measure $V_{GSR} = 79.45$ km s^{-1} for R15. This is dissimilar to the other overdensities in the region, i.e. the adopted VOD velocity ($V_{GSR} \simeq 130$ km s^{-1}), the Pal5 velocity ($V_{GSR} \simeq -106.47$ km s^{-1}) or the expected velocity of the Sgr stream from the triaxial model (which shows peaks at $V_{GSR} \simeq 0$ and -150 km s^{-1} as shown in Figure 4.3). This potential detection of Sextans in our data provides an additional validation for our statistical method and its ability to distinguish structure from the smooth Galactic halo.

4.4 Results

We introduce a selection technique to separate Sgr member stars from the background. As part of this method we first select only the best K and M-giant measurements from 24,110 spectroscopic observations. We then assign a likelihood of a given star *not* being part of the smooth Galactic halo. This is done by drawing a distribution using Equation 4.1 and calculating a likelihood per star per field using Equation 4.2. We identify 106 likely members of the Sgr stream and find three main results:

1) The Sgr stream V_{GSR} evolution with Λ indicates agreement with a triaxial model for the Milky Ways dark matter halo. We compare the kinematics of the observed Sgr stream stars with those of extant simulations of the tidal disruption of Sgr. From comparisons with 4 models we choose to use the triaxial model of Law & Majewski (2010) and find general agreement across the Sgr stream.

2) The Sgr stream MDF evolution with Λ has yielded several interesting results. We find that the trailing arm mean metallicity seems to evolve to a more negative mean as you move away from the Sgr core. We measure a decrease in mean metallicity from -0.59 dex in the core to -0.97 dex as you increase in Λ. This metallicity gradient in which material further from the Sagittarius core is less metal-rich is consistent with the scenario of tidal disruption from a progenitor dwarf galaxy that possessed an internal metallicity gradient. In the leading arm we have larger standard deviations lacking a clear trend; this larger range of values may be due to a mixing of orbital phases in the leading arm.

3) A search for overdensities finds three groups consistent with the triaxial model and one potential detection of the Sextans dwarf at R15. We report on this new detection, the R15 overdensity, located at RA, DEC $\simeq$ (10.2, $-$01.4), which has peaks in the metallicity distribution at [Fe/H] = -1.10 and $+0.46$ dex and an average velocity of $V_{GSR} = 78.48$ km s^{-1}. The R15 overdensity does *not* appear to coincide with either the triaxial model of Law & Majewski (2010), the VOD, Pal5 or the smooth galactic halo as represented by Besançon; but it does coincide in both spatial and velocity coordinates with the Sextans dwarf.

The parameter space we use for this study includes the modified RAVE pipeline log(g), T_{eff}, [m/H] metallicity, and velocity. We have velocity values obtained through fitting the Ca II 8500 Å triplet with IRAF software and we use the 2MASS photometric colors for initial object selection, but we note that for many of our objects this parameter space could be expanded. The *ppmxl* (Roeser et al. 2010) catalog, the Sloan Digital Sky Survey (SDSS) (York et al. 2000) observations, and the ongoing Skymapper photometric survey (Casey et al. 2012b) may all be incorporated in the future.

"There's no reward in being right all the time."

Batman

5

The Orphan Stream

5.1 Introduction

Deep, large-area photometric surveys such as 2MASS and SDSS have revealed that the sky is criss-crossed with stellar streams. These include the main focus of this work, the broad trails of stars torn from the Sagittarius dwarf galaxy (e.g., Majewski et al. 2003; Belokurov et al. 2006b), as well as narrow, delicately-shaped streams such as those from the disrupting globular clusters DG-1 (Grillmair & Dionatos 2006), Pal 5 (Odenkirchen et al. 2003) and NGC 5466 (Belokurov et al. 2006a).

One such stream found in the halo of the Milky Way is the 'Orphan Stream', so named for its lack of an obvious progenitor. The Orphan Stream was detected in SDSS data by Belokurov et al. (2006b), and independently by Grillmair & Dionatos (2006). On the sky, it crosses the Sgr stream some 50 degrees above the disk in the direction of the Galactic anti-centre. Subsequent analysis showed that the stream's width is in excess of 500 pc (> 1 degree on the sky) and has a noticeable heliocentric distance gradient (Belokurov et al. 2007a). The leading disruption hypothesis put forward for the Orphan Stream's progenitor is that it has undergone near complete disruption and is hidden somewhere below the Celestial Equator, i.e., outside the SDSS footprint (Sales et al. 2008; Newberg et al. 2009). However, another exciting hypothesis is that the Orphan Stream is associated with the object Segue 1 (Figure 5.1) which has a radial velocity similar to the Orphan Stream (Newberg et al. 2010).

Parameter	value	source
Orphan		
[Fe/H] (dex)	-1.63 to -2.10	Newberg et al. (2010); Casey et al. (2013)
σ([Fe/H]) (dex)	0.56	Casey et al. (2013)
D(kpc)	22.5 ± 2.0	Casey et al. (2013)
$V_{\rm GSR}$(km/s)	95	Newberg et al. (2010)
$V_{\rm GSR}$(km/s)	82.1 ± 1.4	Casey et al. (2013)
Segue 1		
[Fe/H] (dex)	-2.7 ± 0.4	Norris et al. (2010a)
σ([Fe/H]) (dex)	0.7 ± 0.3	Norris et al. (2010a)
D(kpc)	23 ± 2	Belokurov et al. (2007b)
$V_{\rm GSR}$(km/s)	113.5	Simon et al. (2011)
r_h (arcseconds)	4.5t o 4.6	(Belokurov et al. 2007b)
RA,DEC	10:07:04,+16:05:55	(Belokurov et al. 2007b)

TABLE 5.1: Table of parameters from the literature for the Orphan Stream and its possible progenitor Segue 1. Note that all $V_{\rm GSR}$ velocities for the Orphan Stream are for coordinates near $\Delta\Lambda_{\rm Orphan} \sim 4°$of Newberg et al. (2010), located approximately 35° from Segue 1.

The Orphan Stream is particularly intriguing. Its width on the sky is broader than globular cluster streams, and smaller than streams from dwarf galaxies such as Sagittarius (Belokurov et al. 2007a). The Orphan Stream exhibits chemo-dynamical properties which are in between those of streams arising from dwarf galaxies and those from globular clusters (Belokurov 2013). The progenitor for the system remains unknown, and it is perhaps the only major tidal stream discovered in the outer Milky Way halo without much spectroscopic follow-up data. To date, only a handful of members scattered along the stream have been detected in SDSS data (Grillmair & Dionatos

2006; Belokurov et al. 2007b; Niederste-Ostholt et al. 2009; Norris et al. 2010a). High resolution spectra taken with the Very Large Telescope of the Orphan Stream have been inconclusive because of the extreme sparseness of the stream (Gilmore et al. 2013).

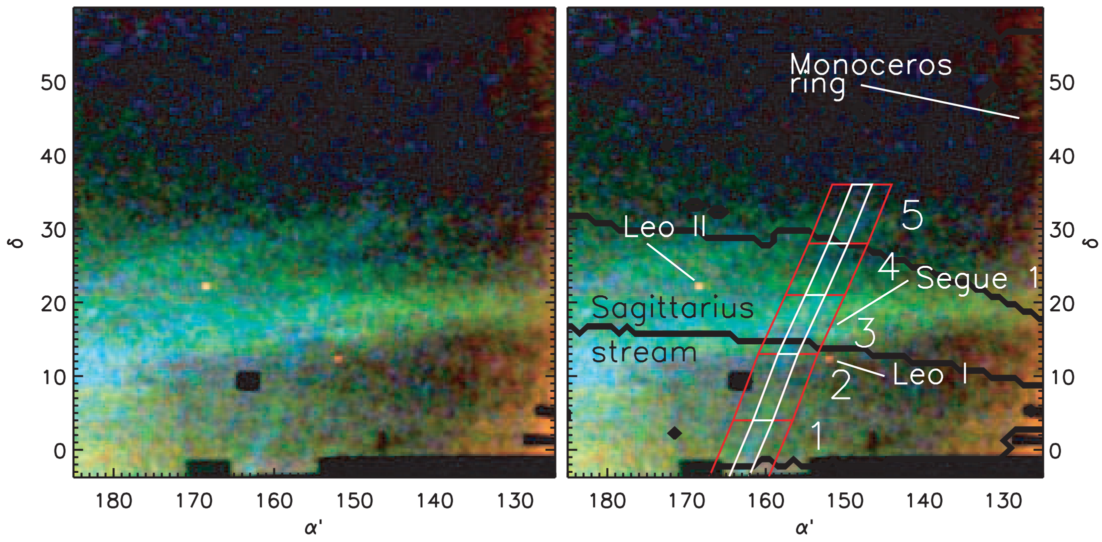

Figure 5.1: Left: False colour RGB composite image showing the density of stars near the Orphan Stream. Right: Sagittarius and Monoceros structures, together with the on-stream and off-stream fields along the Orphan Stream and Segue 1 (Belokurov et al. 2007a).

Because the Orphan Stream is so diffuse and extended on the sky, the wide field of view and large number of fibres of 2dF + AAOmega on the AAT make it the ideal instrument for its study. We observed a large sample of candidate Orphan Stream stars in a single 2dF+AAOmega pointing at (RA,DEC)=(10:48:48.0,−00:42:00). The single pointing we chose corresponds to coordinates near $\Delta\Lambda_{\mathrm{Orphan}} \sim 4°$of Newberg et al. (2010). Our goals were to: 1) gain a better understanding of the progenitor, as the velocity dispersion of the stream can indicate whether the progenitor was a globular cluster or a dwarf galaxy; 2) identify bright member stars, whose metallicities we can estimate and which we can target for follow-up high-resolution spectroscopy to obtain detailed elemental abundances; 3) potentially test the cold dark matter (CDM) paradigm, since CDM simulations indicate that stellar streams orbiting the Milky Way should interact with small dark matter sub-halos (Yoon et al. 2011; Carlberg 2009), causing twists and holes, as well as kinematic heating of stars in the stream. These data will shed light on the nature of the stream's progenitor and its possible association with Segue 1.

Segue 1 is a faint satellite galaxy of the Milky Way. Originally thought to be a star cluster, it was discovered by Belokurov et al. (2007b) as an over-density of stars in the SDSS. It is now thought to be a dissolving dwarf galaxy largely because of its metallicity spread (Niederste-Ostholt et al. 2009; Norris et al. 2010a). Segue 1 is located at (RA, DEC)$_{\mathrm{J2000}}$ =(10:07:04, +16:04:55) or (l,b) = $(220.5°, 50.4°)$, and has a distance of about $\sim 23 \pm 2$ kpc (Belokurov et al. 2007b).

Segue 1 overlaps the leading arm of the Sgr stream, but its velocity is about $\sim$ 100 km s^{-1} separated from that of the Sgr stream at that position. A stellar velocity structure near Segue 1 was found to overlap with the ultra-faint satellite galaxy (Belokurov et al. 2007b). Estimates of the half light radius (the extent) of Segue 1 are between r_h $\sim$4.5 and 4.6 arcminutes (less than 0.1°)(Belokurov et al. 2007b). The average metallicity of Segue 1 should be approximately [Fe/H] = -2.7 ± 0.4 dex (Norris et al. 2010a), although it has individual stars as low as [Fe/H]= -3.3 ± 0.2 dex (Geha et al. 2009).

The Segue 1 dwarf has a mean heliocentric velocity of 208 km s^{-1} (which corresponds to a $V_{\mathrm{GSR}} \simeq 113.5$ km s^{-1}) with a dispersion of $3.7^{+1.4}_{-1.1}$ km s^{-1} as measured by Simon et al. (2011). Radial velocity measurements by Geha et al. (2009) also found a group of four stars moving near 300 km s^{-1} (heliocentric velocity) which occurred in the same region of the sky. Frebel et al. (2013) analysed one star associated with this latter group (having a heliocentric velocity of 300 km s^{-1}) near Segue 1, finding a metallicity of [Fe/H]= $-1.46 \pm 0.05 \pm 0.23$ and typical halo abundances.

The Orphan Stream has been previously found to be rather metal-poor with reported metallicities of [Fe/H]= -1.63 to -2.10 dex from Newberg et al. (2010) and Casey et al. (2013), respectively. The measured parameters from the literature for the Orphan Stream are given in Table 5.1.

In this chapter we compare our observations of the Orphan Stream with the observations by Casey et al. (2013) and Newberg et al. (2010). We apply our Sgr selection technique discussed in Chapter 4 to identify Orphan Stream candidates based on the smooth Galactic halo as simulated by the Besançon model (Robin et al. 2003). We then discuss our results in relation to previous observational studies of this rather complex region of the Galactic halo.

5.1.1 Observations

One field of the Orphan Stream, centred on (RA,DEC)=(10:48:48.0,−00:42:00)[1] was observed using the AAOmega instrument on the AAT described in Chapter 2.

We concentrate our analysis on the features of the calcium triplet in the red and the magnesium triplet in the blue following the standard data reduction plus the modified RAVE pipeline as outlined in Chapter 2. Following Chapter 2, the velocities are obtained through template fitting of the calcium triplet lines and metallicities [Fe/H]≃[m/H] come from the modified RAVE pipeline. We additionally have SDSS photometric colour information for these objects as that was our selection catalog (as opposed to the 2MASS colours we used for the Sgr dwarf). We obtained five exposures at 2700 seconds each and used them to create one co-added image consisting of roughly 300 target spectra.

5.1.2 VGSR discussion

As discussed previously in Section 2.4.2, there are two main conversions of V_{GSR} in Sgr literature. However, in order to compare our results to literature for the Orphan Stream we will need to consider not only our conversion (Equation 2.14), the conversion from Casey et al. (2012a) (as shown in Equation 2.13) but also that of Newberg et al. (2010).

The conversion to V_{GSR} from Newberg et al. (2010) is given by:

$$V_{\mathrm{GSR3}} = V_{hel} + 10.1\cos(b)\cos(l) + 224\cos(b)\sin(l) + 6.7\sin(b) \tag{5.1}$$

[1]The observations were prepared with collaborators Sergey Koposov and Vasily Belokurov from the Institute of Astronomy, University of Cambridge, Cambridge UK. Guide stars were picked as low proper motion stars from the Sloan Digital Sky Survey (SDSS) and ppmxl proper motion catalogs to be within the recommended magnitude range. The target objects were selected from the same catalog.

where the l, b coordinates are converted beforehand, following Section 2.4.2.

Comparing our own conversion from Equation 2.14 we follow Section 2.4.2, finding a small mean difference between Equation 2.13 and Equation 2.14 (our conversion versus that of Casey et al. 2012a). The offset from the Newberg et al. (2010) conversion of Equation 5.1 is substantially larger for Orphan Stream data.

For our Orphan Stream stars, we find that the difference in V_{GSR} between Equation 2.14 and Equation 2.13 of $\langle V_{GSR1} - V_{GSR2} \rangle \sim$ -0.015 km s^{-1} . This is a bit higher than what we previously found for Sgr stars, which had a mean difference of $\sim$ 0.0012 km s $^{-1}$, but still small enough to cause no problems with any comparisons to Casey et al. (2012a). However, when comparing to Newberg et al. (2010), we find (using Equation 2.14 and Equation 5.1) that we have a mean difference $\langle V_{GSR1} - V_{GSR3} \rangle \sim$ -4.47 km s^{-1} . This offset is systematic and will need to be accounted for in data comparisons with Newberg et al. (2010).

5.2 Probability of Orphan Stream membership

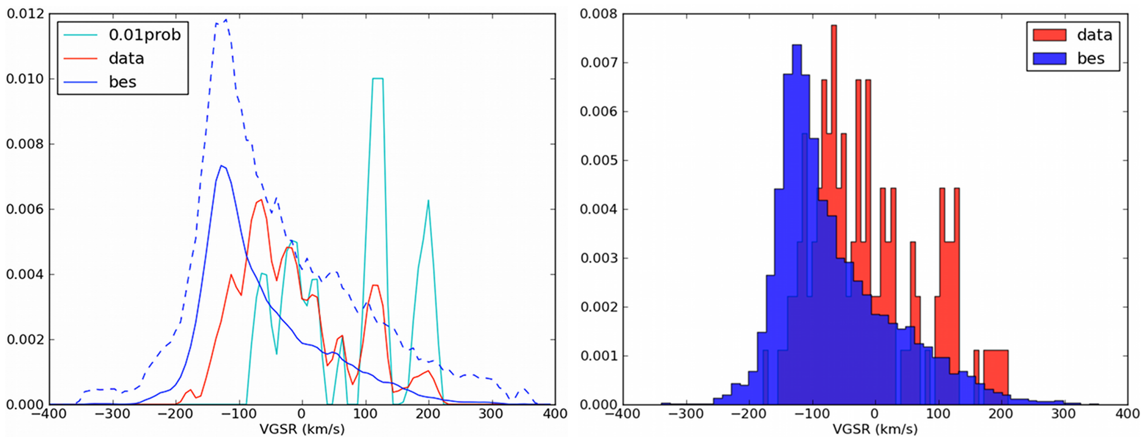

FIGURE 5.2: The membership probability calculation for the Orphan Stream region (left panel), applying the same methodology as Figure 4.3. Red is the generalised Gaussian histogram for the region. Dark blue is the Besançon Galactic model (Robin et al. 2003). Light blue is the probability of our data deviating from the smooth halo (scaled to be visible). The top dark blue dotted line marks the confidence level (C_{bes}) cutoff for membership in the dark blue distribution (the modelled smooth Galactic halo). Right is the velocity histogram for the raw data and the predictions of the Besançon model.

As initial criteria for selecting Orphan Stream stars, we require that the velocity be between -400 and 400 km s^{-1} and that the measured IRAF radial velocity error V_{err} not be greater than 30 km s^{-1} (see Chapter 2 for a full error description). We do not use the RAVE quality cut in drawing our velocity distributions.

To determine if our stars are members of the Orphan Stream there are several directions from which to approach the problem. We will use the method developed in Section 4.1.1 to screen our stars for objects which are '*not*' likely to be part of the Milky Way's smooth halo. Using Equation 4.1 we generate a generalised Gaussian histogram of the velocity distribution of the objects in our data and compare them to the Besançon model of the Galaxy (Robin et al. 2003).

The probability of not being part of the Galactic smooth halo is calculated following Equation 4.2, where the distribution for the Besançon model is sampled to give a confidence level corresponding to the location of 99.6% of the data. This probability distribution is shown in Figure 5.2 in light blue. The high probability 'P1' objects are seen where the light blue line is at its maximum (defined to be one, but scaled to fit the plot of Figure 5.2). The largest detection of P1 stars appears to be near $V_{GSR}(P1) \simeq 110$ km s^{-1}, with a small secondary (non-P1) peak in probability at $V_{GSR} \simeq 200$ km s^{-1}, as shown in Figure 5.2. These two maxima are the most significant deviations from the smooth Galactic model in our data. The P1 detection velocity is consistent with the Segue 1 dwarf mentioned earlier, as Segue 1 is known to have a mean velocity of $V_{GSR} \simeq 113.5$ km s^{-1} (Simon et al. 2011). However, we note that as our stream area is separated by more than 35 degrees from Segue 1 this apparent agreement is likely coincidental.

We note that both of these values are higher than the previously estimated velocities for the Orphan Stream in this area (given in Table 5.1). The small increase in the distribution near $V_{GSR} \simeq 80$ km s^{-1} in Figure 5.2 may be due to a component of the 82.1 ± 1.4 km s^{-1} stellar group from Casey et al. (2013), but as it is below the confidence interval for detection with respect to the Besançon model we cannot confirm that we are detecting the same velocity structure. The full set of P1 data is given in Table 5.2. We note that the high errors reflect a overall signal-to-noise for our Orphan Stream data, which were taken under cloudy conditions.

RA,DEC	V_{GSR},V_{err}	gmag	rmag	pRA,pDE	Rcoeff	T_{eff}	log(g)	[m/H]
(°)	(km s^{-1})	mag	mag	(mas yr^{-1})		K		(dex)
10:49:55.80 -01:08:37.2	108.63,8.835	18.006	17.439	-8.8,2.3	23.7	3562	1.26	-1.79
10:47:22.50 -00:49:29.3	127.43,16.452	19.199	18.678	-7.3,-12.2	13.27[a]	5388	2.16	0.19
10:46:29.30 -00:19:38.5	124.40,13.246	17.92	17.325	-1.7,-2.1	8.17[a]	12437	4.34	-0.63
10:46:50.40 -00:13:15.6	119.42,14.347	17.477	16.94	1.8,-5.6	11.6[a]	7270	4.99	-0.06
10:46:26.70 -00:05:25.6	107.8,27.382[b]	20.274	19.954	-1.5,-8.4	48.74	…	…	…
10:47:39.90 +00:08:40.5	131.88,19.411	19.049	18.689	-3.8,-8.2	…[a]	8239	1.0	-2.43
10:48:41.40 -00:13:55.6	108.69,24.955[b]	20.365	19.913	12.0,-4.2	…[a]	8578	1.81	0.45
10:49:51.10 +00:08:55.6	125.16,27.91[b]	20.53	20.166	-10.6,-8.1	9.83[a]	3495	1.89	0.5
10:49:28.00 -00:12:09.0	112.99,17.863	20.287	19.884	25.0,-29.4	13.32[a]	3077	3.76	0.38
10:49:27.40 -00:21:43.4	130.22,24.376 [b]	19.866	19.615	-5.6,-7.8	23.76	3088	4.41	0.27
10:49:55.90 -00:09:56.2	110.84,26.695[b]	20.144	19.843	-4.8,-7.3	…[a]	7594	0.92	-2.29
10:52:21.60 -00:22:18.3	121.66,20.882[b]	20.293	19.708	-3.2,-4.7	19.15	6722	0.45	-0.9
10:50:34.20 -00:43:06.1	117.02,19.127	20.487	20.008	…,…	…[a]	8575	2.63	-0.25

TABLE 5.2: P1 data from the Orphan Stream. We note the relatively high velocity errors (subset[b] data) and the large number of stars below the RAVE Rcoeff limit (subset[a] data, Rcoeff$\leq$ 15). The best candidates for metallicity and velocity are shown highlighted. This list of candidate stars is given with the original SDSS photometric g and r colours as well as the ppmxl proper motions, pRA and pDE, used in the initial selection.

The velocities are provided via template fitting of the calcium triplet. These templates use a Gaussian fit as described in Chapter 2. As the velocities are not from the modified RAVE pipeline we only limit them according to the velocity errors to return the maximum number of usable velocities for the Gaussian velocity distribution. We only restrict Rcoeff based on the final selected metallicity estimates, not the velocity values. The values that do not fill the Rcoeff requirement are 'SetA', shown as the values in subset[a] in Table 5.2. The value of Rcoeff = 48.74 is the only case of the modified RAVE template not converging while still fulfilling the Rcoeff $\geq$ 15 condition for the Orphan Stream. Visual inspection revealed the lack of conversion to be due to a low signal-to-noise for the spectra. We note that the star corresponding to the metallicity value of 0.27 dex has a rather high log(g) = 0.45 surface gravity, and we consider that this star and the other log(g) $\geq$ 2.3 stars may be dwarf contamination of our sample rather than true giant measurements. These are excluded from our measurements. For measurements involving the metallicity we require that the metallicity be a real number (have a converging fit from RAVE) and Rcoeff ≥ 15. Objects which do not fill the velocity requirement are 'SetB', shown as the values in subset[b] in Table 5.2. We are left with two stars with reliable metallicity measurements and three stars with low error velocity measurements after excluding high values of log(g), and errors (SetA and SetB, respectively).

As we have SDSS colours for all of our data in this field, we can examine the data in terms of photometric groupings. As Newberg et al. (2010) surveyed a large portion of the Orphan Stream we can use their results to compare with our smaller field of observations. We initially compare the observations of Newberg et al. (2010) and Casey et al. (2012a) with our data and, although we overlap in spatial coordinates, we do not have any shared objects.

5.3 Comparison with previous work

As likely Orphan member stars are assigned a probability by Casey et al. (2012a), we use only objects that are assigned a high probability to do our comparisons. Due to the difference between the spatial scale of our data and the observations of Newberg et al. (2010), we will concentrate on comparison with the nearby observations of Casey et al. (2012a).

The P1 objects in Figure 5.2 form a velocity group which indicates potential substructure in the halo. However, this velocity substructure is not consistent with the detections by Casey et al. (2012a) or Newberg et al. (2010). The target stars from our data and the data of Casey et al. (2012a) cover just two degrees on the sky, while the sample of Newberg et al. (2010) spans approximately 100 degrees.

The spatial distribution of the target stars for both our observations and those of Casey et al. (2012a) is shown in the top panel of Figure 5.3. Displaying only the high probability Casey objects we colour code the velocities of their objects (diamonds) as well as our P1 data (circles), and display our background observations as black points. Both our data and the data of Casey et al. (2012a) cover a similar region of the sky.

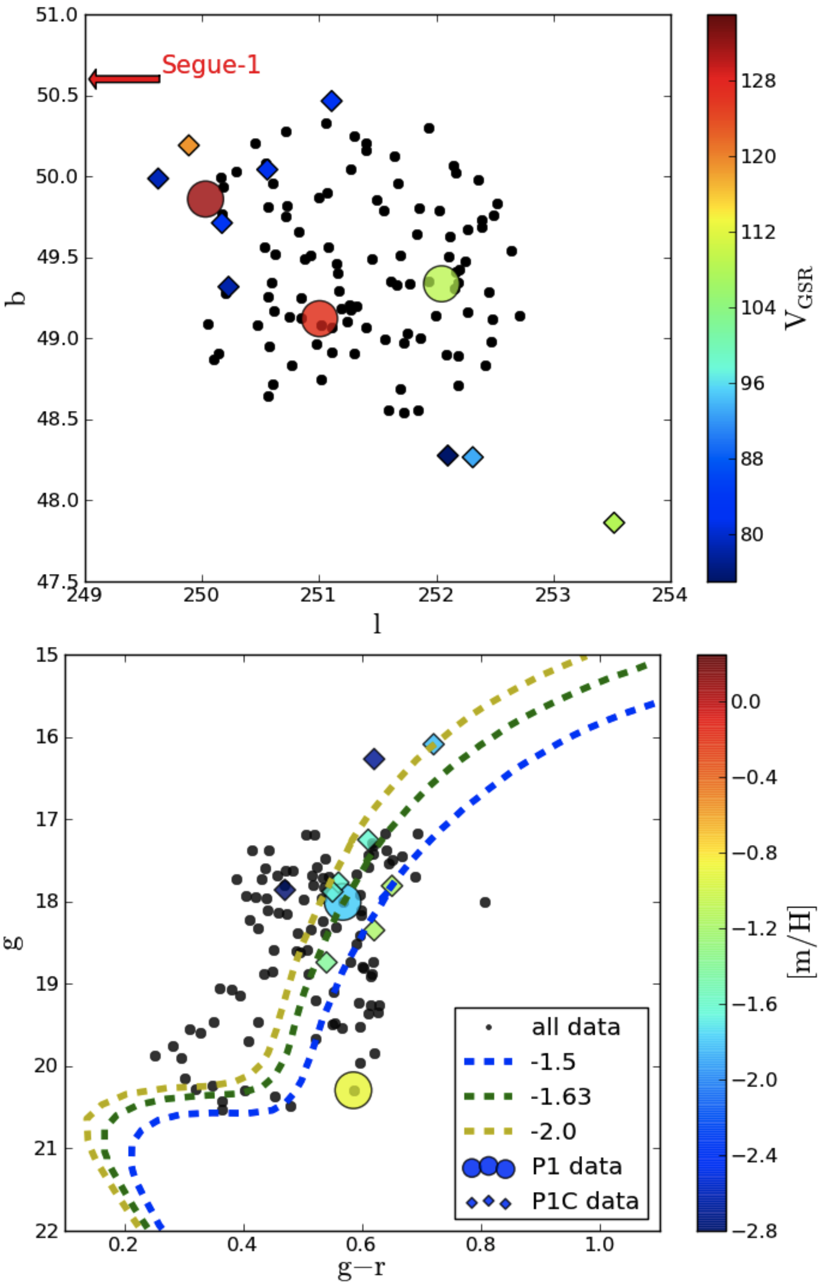

FIGURE 5.3: Top: the spatial comparison in l,b coordinates between our spatial and velocity data and the data of Casey et al. (2012a). Segue 1 is about 35 degrees to the left, as shown by the red arrow. The colour diamonds are high probability objects from Casey, the small black points are all of our observations, the large colour circles are our P1 data and the black points are other observations in our dataset. Bottom: the colour-magnitude diagram of our data in SDSS g-r and g. The Marigo et al. (2008) isochrones shown are 10 Gyr for metallicities of [m/H] = -1.5, -1.63 and -2.0, as referenced by Casey et al. (2012a). The smaller number of P1 objects in the bottom panel is due to the additional RAVE Rcoeff criterion for metallicities.

The distance between our observations and the Segue 1 galaxy (direction shown by the red arrow in Figure 5.3) is about thirty degrees. This suggests that our overlapping velocity points (Segue 1 is found at $V_{GSR} \simeq 113.5$ km s^{-1}; Simon et al. 2011) may be coincidental.

We overplotted the same isochrones used by Casey et al. (2012a) on our data, shown in the lower panel of Figure 5.3. The isochrones at [Fe/H]=-2.0 and [Fe/H]=-1.5 (shown in yellow and dark blue on Figure 5.3, respectively) are 10 Gyr isochrones from Marigo et al. (2008) shifted to the distance of 21.4 kpc to the Orphan Stream found by Newberg et al. (2010). The isochrone at [Fe/H] = -1.63 (the green curve in Figure 5.3) is the Casey et al. (2012a) best fit isochrone (from Marigo et al. 2008) which allowed Casey et al. (2012a) to measure a best-fitting distance to the stream of 22.5 ± 2.0 kpc at (l,b)=$(250°, 50°)$. The small number of our of P1 metallicities in Figure 5.3 does not enable us to make a new distance estimate and we note that only one of our three stars with a reliable metallicity lies along the best-fit Orphan Stream isochrone.

The colour-magnitude diagram in the lower panel of Figure 5.3 indicates that our target selection (shown as diamonds) has sampled a broader colour range than Casey et al. (2012a). This difference in sampling may result in our probing a different stellar population (or populations) than Casey et al. (2012a). There is, therefore, the definite possibility that our observations and those of Casey et al. are looking at different parts of Milky Way halo substructure.

5.4 Total velocity and metallicity distributions

Our final velocity and metallicity distributions are shown in the histograms of Figure 5.4. We note that, although we overlap in metallicity and velocity space with the data of Casey et al. (2013), our P1 data are peaked at a higher velocity. This supports the idea that we might be looking at different components of Milky Way halo substructure.

We find that our P1 data have a mean velocity $V_{GSR}(P1) \simeq 122.65$ km s^{-1} and a

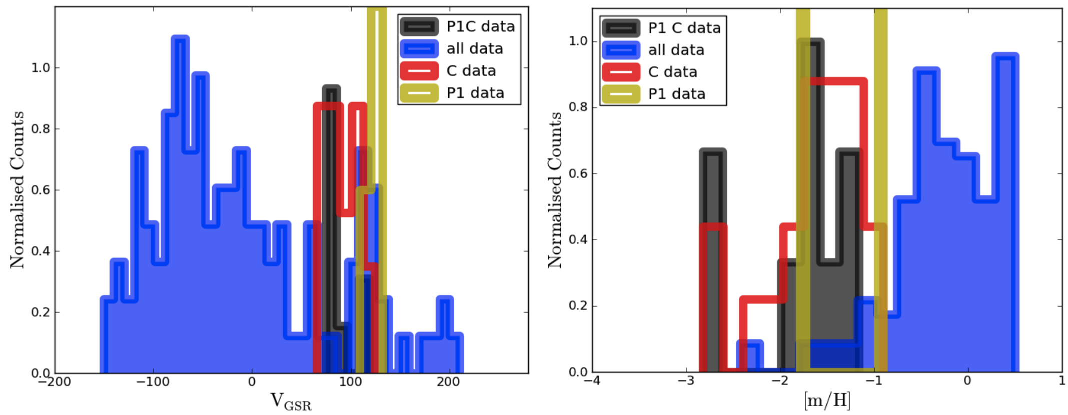

FIGURE 5.4: Histogram distribution in velocity (left) and metallicity (right) comparing our data for the Orphan Stream to those of Casey et al. (2013). Our overall distribution is given by 'all data' (blue), and our P1 points 'P1 data' (yellow). The stars from Casey et al. (2013) are labeled 'C data' (red), with their high probability stars as 'P1C data' (black). The smaller number of P1 points in the bottom plot is due to the additional Rcoeff data requirement from the RAVE pipeline.

mean metallicity of $[m/H](P1) \simeq -1.35$ dex. We note that these mean measurements only included two metallicity measurements and three velocity measurements respectively (the highlighted values in Table 5.2). When compared to the original literature values of Table 5.1 this is a higher metallicity (slightly) and higher velocity than we might expect for the Orphan Stream. However, if we only use the best measurements from Table 5.2, excluding points in SetA (subset^a) and SetB (subset^b), we find only one measurement at $[m/H](P1) \simeq -1.79$ dex and $V_{GSR} \simeq 108.63 \pm 8.83$ km s^{-1}. This single star is consistent with previous metallicity results for the Orphan Stream, although at a higher V_{GSR} (as compared to $V_{GSR} = 82.1 \pm 1.4$km s^{-1} from Casey et al. 2013).

5.5 Results

We present the results of our selection method from Chapter 4 on a single observation of the Orphan Stream centred at $(RA, DEC)_{J2000} = (10{:}48{:}48.0, -00{:}42{:}00)$. We search for substructure over the two degree field (diameter) we observe from the Orphan Stream and recover a significant radial velocity peak over the Milky Way smooth halo. The subset of data that gives the best detection of the overdensity includes higher error velocity points, as well as stars which do not have reliable RAVE fits for metallicity. After the detection we consider data which have velocity errors less than 20 km s^{-1} (four stars) and data which meet the metallicity quality criterion of Rcoeff ≥ 15 (two stars).

Using the selection method that we designed in Chapter 4 on the Orphan Stream has led to several results. Firstly, we find that our P1 data with velocity errors less than 20 km s^{-1} results in a mean velocity of $V_{GSR}(P1) \simeq 122.65$ km s^{-1}. We find that our two stars from the P1 data with low metallicity errors (Rcoeff ≥ 15) have metallicities of $[m/H] \simeq -1.79$ and -0.9 dex, or a mean metallicity of $[m/H](P1) \simeq -1.35$ dex. We note that the two metallicity measurements may be coincidental and future work is needed to determine if these two objects form a true group.

We additionally find that the mean velocity of our P1 detection is coincidentally consistent with the Segue 1 dwarf ($V_{GSR} \simeq 113.5$ km s^{-1}; Simon et al. 2011), although we are approximately 35 degrees away from Segue 1 in the sky. Our metallicity estimates for the Orphan Stream are slightly higher on average than previous measurements of $[Fe/H]= -1.63$ to -2.10 dex, from Newberg et al. (2010) and Casey et al. (2013) respectively. Finally, we note that we detect a low amplitude secondary spike in probability at $V_{GSR} \simeq 200$ km s^{-1}, as shown in Figure 5.2.

Our single low error measurement in both velocity and metallicity is at $[m/H](p1) \simeq -1.79$ dex and $V_{GSR} \simeq 108.63 \pm 8.83$ km s^{-1}. A small velocity component near $V_{GSR} \simeq 80$ km s^{-1} in Figure 5.2 could correspond to the Orphan Stream measurement of 82.1 ± 1.4km s^{-1} from Casey et al. (2013), but as it is below the confidence interval for deviation from the smooth Besançon model we cannot confirm it without further observations. We conclude that it is likely that, with our P1 detection, we are looking at a different substructure than the previously mapped Orphan Stream of Casey et al. (2013) and Newberg et al. (2010).

"The important thing is to not stop questioning. Curiosity has its own reasons for existing"

Albert Einstein

6 Conclusion

This project began as an effort to map out the core region (Core 1) of the Sgr dwarf galaxy and thereby test the 'rotating disk' hypothesis (Peñarrubia et al. 2010). The project was then expanded to provide more complete coverage of the core region (R01) and include data throughout the entire Sgr stream, spanning the entire sky. Our core mapping provides additional support for the idea of a non-rotating pressure supported dwarf as a progenitor of the Sgr dwarf system.

We then set out to compare our data to the models of the Sgr stream from Law & Majewski (2010). For this comparison, we developed a new selection method for identifying stars in our stream observations that are probably not part of the smooth Milky Way halo. We tested the results of our method on the Sgr stream model and then applied our method to a single observed field of the Orphan Stream.

6.1 Data reduction and analysis

In Chapter 2, we described our data reduction methods and showed the preliminary results from the Core 1 region. This included discussion of how the spectroscopic candidates were selected and the AAT instrument used to make the observations.

As mentioned in Chapter 1, there are three main datasets that we worked with in this thesis. These are the 'Core 1' set, 'R01', and a 'Stream' set, defined as:

- Core 1: The initial 6 pointings around the core of Sgr. These stars are used to illustrate the data reduction and discussed in detail in Chapter 3.

- R01: The entire core region, including Core 1 and all follow up observations near the core. The core region, shown in Figure 2.1, includes 23 pointings around the centre of the Sgr dwarf. Discussed in detail in Chapter 3, this region is treated as a single point when discussing the stream in Chapter 4.

- Stream: This data set includes all Sgr core and stream observations from Figure 2.1. The distribution and selection of Sgr members from the data is discussed in Chapter 4. As noted above, in the stream set all of the core data is referred to as R01.

The core and stream fields together result in a total of $\sim$24,110 spectroscopic observations for candidates associated with the Sgr dwarf and its stream.

The kinematics and metallicities derived from our spectroscopic observations can help us select stars that are members of the Sgr dwarf, as well as characterising the evolution of the the Milky Way. We include 2MASS photometry in our data selection and use template fitting to retrieve velocities for the majority of our spectra. The best metallicity calibration for our data comes from using the parameter [m/H] from the modified RAVE pipeline. We obtained AAT observations of several star clusters of known metallicity to test our calibration and conclude that [m/H]$\simeq$[Fe/H] for our data. The differences in the routines used to derive velocity and metallicity means that the number of stars with low error velocity measurements is larger than the number of stars with the low error metallicities. The metallicities and velocities are used in conjunction with the RAVE log(g) and $T_{\rm eff}$ parameters in Chapter 4 to select member stars of Sagittarius when the velocity is unknown.

6.2 The Sagittarius core

In Chapter 3, we investigated the R01 region around the Sgr core. Our investigation of the 7,036 Sgr stars in the R01 region led to several results:

- The detection of M54 in the centre of the Sgr dwarf. We find signs of an M54 metallicity signature out to its previously measured extent of 0.06° from the centre. This detection is limited to only a few ($\simeq$ 6) stars, and is overwhelmed by the contributions from Sgr as more stars at larger distances from the centre are included in the distribution.

- We find some evidence that the Sgr dwarf has a concentration of more metal-rich stars in its centre. We conclude that the average metallicity is likely higher within the region 2° from the centre of the Sgr core, but the overlapping MDFs of the inner and outer regions make for considerable uncertainty in our measurements. A higher mean core metallicity is a property found for some, but not all, other dwarf spheroidals in the Local Group (Koch et al. 2006; Harbeck et al. 2001).

- We find a mean metallicity distribution (listed in Table 3.1) of $\langle$[Fe/H]$\rangle \simeq \langle$[m/H]$\rangle$ $\simeq -0.59$ dex, with a standard deviation of $\sigma_{[m/H]} \simeq 0.34$ dex. This is lower than the previously measured [Fe/H] $= -0.4 \pm 0.2$ dex of Chou et al. (2007), although it is in agreement with the earlier value of [Fe/H]$= -0.5 \pm 0.2$ from Cole (2001). We note that our sample size is larger than that of any previous study, making subtler population properties like the wings of the MDF more readily apparent.

- For R01, we find a mean velocity (listed in Table 3.1) of $V_{\rm GSR} = 168.76$ km s^{-1} with a standard deviation of $\sigma^{\rm all}_{\rm VGSR}$= 12.2 km s^{-1}. Using hexagon binning, the typical standard deviation in the velocity measured within each hexagon in Figure 3.10 is $\sigma^{\rm typ}_{\rm VGSR} = 12.7$ km s^{-1}. The overall velocity distribution of R01 in Figure

3.10 is an excellent match to the Peñarrubia et al. (2010) pressure-supported model (originally fit to the Core 1 data) shown in Figure 3.2. Our data show a gradient in V_{GSR} from 156 to 170 km s^{-1} across the RA direction ($\sim$ 15 km s^{-1}) as expected from Peñarrubia et al. (2010).

Significant contamination by M54 in our sample is unlikely due to the compact nature of M54 and the large area we survey. We reproduce the velocity trend predicted by the pressure-supported model for the core (Peñarrubia et al. 2011) within 5 km s^{-1}, visually showing a shift of $\sim$ 15 km s^{-1} across the main body of Sgr. The robust results found here illustrate the importance of large sample size in distinguishing overall behaviour.

6.3 The Sagittarius stream

In Chapter 4 we introduced a selection technique to separate Sgr member stars from the background. As part of this method, we first selected only the best M and K-giant measurements from 24,110 spectroscopic observations. We then assigned a probability of a given star *not* being part of the smooth Galactic halo, as simulated with the Besançon model (Robin et al. 2003). The probability is found by drawing a distribution using Equation 4.1 and calculating a probability per star per region using Equation 4.2. We identified 126 stars in the Sgr stream as '*not*' part of the smooth Milky Way halo and therefore likely members of the Sgr stream.

- We compared the kinematics of the observed probable Sgr stream stars with those of extant simulations of the tidal disruption of Sgr. From comparisons with four models, we chose the triaxial model of Law & Majewski (2010) as the best match to the kinematics and positions of likely Sgr members.

- We followed the metallicity and velocity distributions of Sgr member stars. The largest discrepancies between likely Sgr members and the triaxial model of Law & Majewski (2010) lie in the region $\Lambda \sim 150 - 250°$. A higher sampling rate or re-selection of data in this region may help to clarify the true metallicity-velocity distribution of Sgr stream stars in this, the trailing arm region of the sky.

- We find that stars which clearly belong in the stream have a range of metallicities nearly as broad as the body of the core region R01, spanning $-1.5 < [\mathrm{m/H}] < 0.0$ dex. Furthermore, trailing arm mean values of [m/H] are generally lower than leading arm values, indicating a possible variation in metallicity from the leading to the trailing arm.

- We report on a new stellar over-density, the R15 overdensity, located at RA, DEC$\simeq$ (10:13:24, −01:26:30), which has an average metallicity of $[\mathrm{Fe/H}] = -0.81$ dex and an average velocity of $\mathrm{V_{GSR}} = 79.87$ km s^{-1} (the dispersion in velocity is $\sigma = 11.29$ km s^{-1}).

- The R15 overdensity does *not* appear to coincide with either the triaxial model, the VOD, Palomar 5 or the smooth Milky Way halo; but it does coincide in both spatial and velocity coordinates with the Sextans dwarf. The triaxial model predicts Sgr members in the locations of the peaks for R04 and R23. While there is a general agreement with the model of Law & Majewski (2010), we have 2 new M and K-giant overdensities which may be associated with the Sgr dwarf (the R04 and R23 items in Table 4.3.2), as well one which is a strong candidate for membership in the Sextans dwarf (R15).

We conclude that while there is a general agreement with the model of Law & Majewski (2010), we do have several new M and K-giant overdensities which may be associated with either the Sgr dwarf or the Sextans dwarf. The wide range of metallicity values for the Sgr stream across the sky appears to show more variation than previous mappings (Chou et al. 2007; Casey et al. 2012a). This wide spread in metallicity across the stream that will have to be accounted for in any future modelling efforts.

6.4 Observations of the Orphan Stream

In Chapter 5, we applied our selection method from Chapter 4 to the data from a single pointing on the Orphan Stream centred at (RA, DEC)$_{\rm J2000}$ = (10:48:48.0,−00:42:00). We searched for substructure over the two degree diameter field we observe from the Orphan Stream, and recovered a significant radial velocity peak over the Milky Way smooth halo. The subset of data that gave the best detection of the overdensity includes higher error velocity points as well as stars which do not have reliable RAVE fits for metallicity. After the detection, we divided the data into two regions, data which have velocity errors less than 20 km s^{-1} (seven stars) and data which have RAVE fits of Rcoeff $\geq$ 15 (three stars). Using our probability selection method on the Orphan Stream led to several main results:

- Our P1 data with velocity errors less than 20 km s^{-1} have a mean velocity $V_{\rm GSR} \simeq 122.65$ km s^{-1}.
- Our two stars from the P1 data with low metallicity errors (Rcoeff $\geq$ 15) have metallicities of [m/H] $\simeq -1.79$ and -0.9 dex.
- Our single low error measurement in both velocity and metallicity is at [m/H](P1) $\simeq -1.79$ dex and $V_{\rm GSR} \simeq 108.63 \pm 8.83$ km s^{-1}.
- We consider it likely that, with our P1 detection, we are looking at a different substructure than the previously mapped Orphan Stream of Casey et al. (2013) and Newberg et al. (2010).

The mean velocity of our P1 detection is coincidentally consistent with the Segue 1 dwarf ($V_{\rm GSR} \simeq 113.5$ km s^{-1}; Simon et al. 2011), although our observation is just over 30 degrees from Segue 1 in the sky. An additional small velocity component near $V_{\rm GSR} \simeq 80$ km s^{-1} in Figure 5.2 could correspond to the Orphan Stream measurement of Casey et al. (2013) ($V_{\rm GSR} = 82.1 \pm 1.4$ km s^{-1}) but as it is below our confidence interval we cannot confirm it without further observations.

6.5 Future work

In the course of this research project, a number of questions arose which warranted further investigation. Several of these in particular sprang from interesting subsets of data present in our large spectroscopic database. Time constraint prevented the presentation of these topics in this work, but we plan to follow them up at a later date. The first of these additional lines of investigation centres on a subset of targets which, on the basis of multiple ($\geq$3) observations, appear to be radial velocity variables. The characterisation of these objects (e.g., determining if they represent multiple star systems) is left for future work.

We also found a subset of stars which appeared to have calcium triplet line strengths consistent with their being extremely metal poor stars. As noted by Monaco et al. (2003), based on the observation of BHB stars we know that '*the Sgr galaxy hosts a significant (of the order of 10%) old and metal-poor stellar population ([Fe/H] -1.3; age 10 Gyr), similar to that of its oldest clusters (M54, Ter 8)*'. High resolution spectra would be needed to confirm our low metallicity objects. One key question that can be addressed by following up the low metallicity objects is whether or not extremely metal poor stars are common in dwarf galaxies, and if they can be held responsible for the population of extremely metal poor stars we see in the halo of the Milky Way.

It was thought that there were no extremely metal poor stars in classical dwarf galaxies (Helmi et al. 2006), but Tafelmeyer et al. (2010) showed that metal poor stars could be found in such systems. Additional support for the existence of extremely metal poor stars in an ultra-faint dwarf are provided by Simon et al. (2010). Since then the search has continued, and by examining the abundance pattern in M54 and the region around the core of the Sagittarius dwarf (Carretta et al. 2010), we can learn more about the relationship between dwarf galaxies and our Galactic halo (Kirby et al. 2008a).

Finally we observed three fields covering Leo IV, Leo V and the region between them[1]. From de Jong et al. (2010), Leo IV and V seem to share an elongated nature

[1] In the case of Leo IV and V, a program to find the sky positions was written and implemented

typical to Milky Way dwarf spheroids. They also indicate a possible stream feature by noting that: '*The spatial distribution of candidate RGB and HB stars in this region is found to be non-uniform at the* $\sim 3\sigma$ *level.*'. This possible stream was also measured by Jin et al. (2012). They find that a connection between the stream and the Virgo overdensity is much more likely than a connection to Leo IV and Leo V. The possibility that Leo IV and V might be a bound galaxy pair in a manner similar to the Magellanic clouds was investigated by Blaña et al. (2012). They simulate the pair assuming extended dark matter halos and find that the minimum dark matter mass that would allow the pair to be bound is within the range predicted for dark matter content in satellites. We were able to obtain three observations with the AAT centred on Leo V, Leo IV and the area between them. These observations were taken with the same instrument settings as our main Sgr observations during the few windows of time when our primary Sgr targets were not visible in the sky. Future work on this system would include applying the selection technique outlined in Chapter 4 in this part of the sky to determine whether we detect stream-like features.

6.6 The impact of future large surveys

Our efforts to map out Galactic structure have been aided by the AAOmega multiple object spectrograph on the AAT as well as the Sloan Digital Sky Survey (SDSS). Although it was the 2MASS survey that first opened up this field with the discovery of the Sgr dwarf, it was follow-up with the SDSS that led to much of the characterisation of that object and its stellar stream. In order to go further, it is important to note that future planned surveys will give us access to even more data. Two of those projects are outlined below.

With such large targets as M31 and the Milky Way, it is of great interest to note that there are a number of current and upcoming surveys and instruments which will be very useful for work in Galactic Archaeology. These include Gaia, LSST, Pan-STARRS, the Gaia-ESO survey, APOGEE, 4MOST, the Skymapper telescope and the

by Arik Mitchang: `http://web.science.mq.edu.au/ arikm/code/skyfind/`.

HERMES spectrograph. We will discuss the last two of these in more detail. The Skymapper telescope became operational in 2012. This telescope will have a 5.7 deg^2 field-of-view with a Cassegrain style imager and a 268 Mega-pixel CCD array (Murphy et al. 2009). It will be able to measure surface gravities and metallicities for 100,000,000 stars, and it is optimised to recover fundamental stellar parameters in the form of a six colour (uvgriz), six-epoch digital record of the southern sky. This multicolour and multi-epoch survey of the southern hemisphere, known as the Southern Sky Survey, will yield wide-area uniform photometry for objects between 8th and 23rd magnitude. It is now returning preliminary data.

Another new mission of great interest to Galactic Archaeology is 'HERMES', the High Efficiency and Resolution Multi-Element Spectrograph (Barden et al. 2010). Designed for the Anglo-Astronomical Telescope (AAT), HERMES is a four-channel high-resolution spectrograph fed by the 400-fibre 2dF fibre positioner, optimised for Galactic Archaeology. The goal of the GALAH (GALactic Archaeology with HERMES) survey, set to begin in 2014, is to determine stellar parameters and detailed elemental abundances for one million stars in the Milky Way. Using the technique of 'chemical tagging', GALAH will identify unique chemical signatures in the thin and thick disks, originating from different formation sites, for star clusters that have long since dispersed (Freeman & Bland-Hawthorn 2002). With these original star-forming groups identified, GALAH will then be able to study the history of star formation and accretion events as well as the overall chemical and dynamical history of the Milky Way. This further research will help us build a more detailed picture of the components of our Galaxy and Local Group, which is, as pointed out by Freeman & Bland-Hawthorn (2002) '*a necessary first step toward achieving a successful theory of galaxy formation*'.

6.7 Conclusions and summary

Looking for and characterising sub-structure in the Milky Way halo is a rapidly growing field of research, and with improvements in instrumentation, both present and future, it will help us to address some of the most important cosmological questions. We can model the growth of structure in a cold dark matter universe in numerical ΛCDM simulations, and try to resolve the problems matching those models to observations on the scale of Local Group galaxies. We can investigate the core/cusp problem by observing more detail from nearby Local Group galaxies. We can use simulations to compare the size and angular momentum of simulated galaxies to real observations.

Finally there is the so-called missing satellite problem, which is directly relevant to this thesis. This problem has made substantial progress over the years. Examination of the Milky Way halo continues to yield new structures. Finding and determining the properties of those structures remains a major topic of interest in astronomy. In this thesis we observed more spectra of candidate Sgr dwarf and stream stars than any other work to date. We developed a new selection method for finding stars which differ from model predictions of the smooth Milky Way halo population. We applied our method on the Sgr dwarf and stream with promising initial results, detecting overdensities corresponding to the Sgr stream, the Sextans dwarf (R15) and a potential detection of the Orphan Stream. The Sgr dwarf still holds some mysteries for us to unravel, as does the Milky Way halo itself hold many new substructures in its grasp, just waiting for us to find them.

A

Appendices

A.1 Table of high probability P1 Sagittarius stream stars

Num	$\mathbf{RA_{J2000}}$	$\mathbf{DEC_{J2000}}$	$\mathbf{\Lambda}$ (degrees)	**B** (degrees)	**log(g)**	$\mathbf{T_{eff}}$ (K)	**[m/H]** (dex)	**Rcoeff**
1	01:58:05.38	-01:45:11.2	102.62	-0.58	1.31	4249.0	-0.92	21.21
2	01:58:37.34	-01:44:19.0	102.75	-0.52	1.18	4182.0	-0.49	28.49
3	01:58:37.34	-01:44:19.0	102.75	-0.52	1.09	4209.0	-0.65	31.0
4	01:58:45.53	-01:43:24.2	102.78	-0.52	1.48	4220.0	-0.4	23.83
5	01:58:45.53	-01:43:24.2	102.78	-0.52	1.34	4148.0	-0.62	22.76
6	01:59:10.97	-02:19:21.7	102.57	0.05	1.66	4571.0	-0.55	36.68

Continued on next page

Table A.1 – *Continued from previous page*

Num	RA_{J2000}	DEC_{J2000}	Λ	B	log(g)	T_{eff}	[m/H]	Rcoeff
7	01:59:50.95	-02:08:49.6	102.8	-0.02	1.08	4098.0	-0.12	20.4
8	02:00:07.30	-02:23:16.8	102.74	0.23	1.36	4206.0	-0.44	31.64
9	02:00:10.75	-01:39:51.5	103.12	-0.39	1.29	4470.0	-0.71	30.25
10	02:00:10.75	-01:39:51.5	103.12	-0.39	1.66	4511.0	-0.9	36.04
11	02:00:33.24	-01:36:46.4	103.23	-0.39	1.75	4368.0	-0.81	21.76
12	02:00:33.24	-01:36:46.4	103.23	-0.39	1.95	4330.0	-0.89	23.38
13	02:00:36.79	-02:05:40.9	102.99	0.03	1.16	4378.0	-0.65	39.38
14	02:00:36.79	-02:05:40.9	102.99	0.03	0.91	4352.0	-0.91	29.51
15	02:01:00.19	-01:48:00.0	103.23	-0.17	2.2	4674.0	-0.67	24.61
16	02:01:00.19	-01:48:00.0	103.23	-0.17	1.94	4891.0	-0.82	25.6
17	02:01:03.12	-02:02:04.2	103.12	0.04	0.27	3926.0	-0.95	41.44
18	02:01:03.12	-02:02:04.2	103.12	0.04	1.67	4304.0	-0.55	34.22
19	02:01:16.68	-01:34:20.6	103.4	-0.33	1.78	4279.0	-0.47	21.67
20	02:02:33.29	-01:38:29.4	103.64	-0.11	2.22	4505.0	-0.49	29.09
21	03:00:12.67	+05:50:44.5	119.85	0.69	1.62	3836.0	-0.65	39.23
22	03:00:20.59	+06:02:06.7	119.97	0.54	2.15	4404.0	-0.13	15.83
23	03:00:40.32	+06:34:28.6	120.31	0.11	1.84	4679.0	-0.25	27.24
24	03:02:50.71	+06:53:02.0	120.93	0.11	0.82	4116.0	-0.99	34.77
25	03:58:20.57	+13:42:56.9	136.18	0.64	1.11	4559.0	-1.5	39.35
26	03:58:45.77	+13:58:35.4	136.39	0.46	0.54	3791.0	-1.17	43.81
27	03:59:42.72	+14:07:32.5	136.66	0.43	1.33	4020.0	-0.59	19.55
28	04:00:24.00	+14:40:31.1	137.06	0.01	1.51	4482.0	-0.77	37.33
29	04:00:58.70	+13:52:26.4	136.82	0.79	0.68	3910.0	-1.02	36.89
30	04:00:58.73	+13:52:26.8	136.82	0.79	0.63	3932.0	-0.93	35.94
31	04:03:19.70	+14:56:39.1	137.81	0.09	0.26	3934.0	-1.08	27.64
32	04:59:05.93	+21:28:01.6	152.56	-0.28	1.25	4263.0	-0.62	18.15
33	04:59:06.00	+20:30:37.1	152.2	0.6	1.52	4426.0	-0.74	23.61
34	05:00:29.88	+21:20:42.4	152.82	-0.05	0.35	3923.0	-1.22	35.07
35	05:00:29.88	+21:20:42.4	152.82	-0.05	0.73	3977.0	-1.01	33.35

Continued on next page

Table A.1 – *Continued from previous page*

Num	RA_{J2000}	DEC_{J2000}	Λ	B	log(g)	T_{eff}	[m/H]	Rcoeff
36	05:02:03.98	+21:04:52.0	153.05	0.34	1.29	4547.0	0.5	20.47
37	06:59:45.96	+21:46:16.7	179.6	7.27	2.28	4353.0	-0.52	25.18
38	07:00:27.79	+21:46:32.5	179.76	7.29	0.81	4421.0	-1.23	28.01
39	07:00:27.79	+21:46:32.5	179.76	7.29	1.86	4836.0	-0.86	45.42
40	07:03:33.91	+21:34:03.7	180.44	7.61	1.86	4797.0	-1.28	49.39
41	07:59:42.55	+32:51:33.5	193.94	-2.43	1.37	4702.0	-1.65	24.28
42	10:00:04.22	+18:18:12.2	222.36	9.25	2.11	4527.0	0.28	36.88
43	10:00:04.22	+18:18:12.2	222.36	9.25	2.25	4571.0	0.24	34.09
44	10:11:48.29	-01:37:32.5	230.65	27.81	2.1	3894.0	0.5	16.61
45	10:11:52.85	-01:44:28.3	230.71	27.92	0.84	3942.0	0.39	22.06
46	10:11:52.85	-01:44:28.3	230.71	27.92	2.17	3997.0	0.5	21.46
47	10:12:26.21	-01:38:30.1	230.83	27.78	1.86	4117.0	-1.07	17.5
48	10:12:41.59	-01:32:51.7	230.87	27.68	1.14	3974.0	-1.72	23.26
49	10:12:41.59	-01:32:51.7	230.87	27.68	1.98	4262.0	-0.89	23.36
50	10:12:41.83	-01:45:27.4	230.93	27.88	1.87	4720.0	-1.11	37.92
51	10:13:20.74	-01:31:59.2	231.04	27.62	2.09	3509.0	-0.61	19.4
52	10:13:22.94	-01:22:27.1	231.0	27.46	1.64	4035.0	-1.18	20.94
53	10:13:34.68	-01:01:59.2	230.94	27.12	1.94	4175.0	-0.65	21.71
54	10:13:35.30	-01:17:54.6	231.03	27.37	1.43	4497.0	-1.11	24.19
55	10:13:55.10	-01:17:03.8	231.11	27.34	1.04	4250.0	-1.34	26.38
56	10:13:55.10	-01:17:03.8	231.11	27.34	2.21	4685.0	-1.24	19.92
57	10:14:04.30	-01:13:22.4	231.14	27.27	1.58	4080.0	-1.38	18.51
58	10:14:04.68	-01:23:46.7	231.19	27.43	1.77	4179.0	-0.87	18.15
59	10:14:39.86	-01:10:52.7	231.28	27.18	1.05	4321.0	-1.0	19.66
60	10:15:52.08	-01:33:31.0	231.73	27.46	1.18	4113.0	-1.29	24.13
61	10:58:20.90	+15:34:44.8	236.66	7.91	1.18	4243.0	-0.7	29.94
62	10:58:20.90	+15:34:44.8	236.66	7.91	1.91	4470.0	-0.61	37.86
63	11:01:45.26	+16:00:08.3	237.29	7.23	1.32	4604.0	-1.11	33.88
64	11:02:19.32	+15:31:30.0	237.58	7.64	1.27	3918.0	-0.53	40.89

Continued on next page

Table A.1 – *Continued from previous page*

Num	RA_{J2000}	DEC_{J2000}	Λ	B	log(g)	T_{eff}	[m/H]	Rcoeff
65	11:02:19.34	+15:31:30.4	237.58	7.64	1.34	3959.0	-0.51	32.07
66	11:02:27.36	+15:35:13.6	237.59	7.57	1.66	4833.0	-1.48	43.44
67	12:25:28.20	+24:20:53.2	251.97	-8.25	1.66	3677.0	0.01	15.43
68	12:25:35.88	+23:18:00.0	252.48	-7.33	2.14	3559.0	0.39	26.38
69	12:26:20.54	+24:31:34.3	252.07	-8.5	1.64	4756.0	-0.85	16.98
70	12:27:24.17	+23:16:01.9	252.87	-7.49	1.63	4082.0	-0.48	19.86
71	12:29:41.66	+24:04:06.6	252.97	-8.44	1.09	4347.0	-1.27	26.03
72	12:29:41.66	+24:04:06.6	252.97	-8.44	0.96	4311.0	-1.49	27.65
73	14:12:45.12	-00:46:50.5	287.07	0.91	2.1	3893.0	0.5	19.36
74	14:14:29.23	-00:31:49.4	287.31	0.47	1.57	4299.0	0.03	25.72
75	14:16:22.44	-01:04:48.0	288.0	0.7	0.42	3987.0	-1.38	39.15
76	14:16:34.99	-00:21:00.4	287.68	0.05	1.98	3640.0	0.43	24.9
77	14:16:36.60	-00:10:30.4	287.59	-0.11	2.03	4592.0	-0.01	20.38
78	14:59:10.44	-06:47:11.4	300.09	0.26	2.17	3688.0	0.38	35.51
79	14:59:58.13	-07:10:29.3	300.46	0.5	2.21	4801.0	-0.3	24.55
80	15:18:34.13	+00:17:22.9	300.8	-8.29	0.95	3857.0	-0.72	33.39
81	15:59:00.53	-14:46:18.8	316.8	0.23	1.37	4225.0	-0.62	22.78
82	15:59:31.73	-14:18:20.5	316.7	-0.25	0.98	3791.0	-0.69	28.23
83	16:00:05.66	-14:39:53.3	316.99	0.01	0.97	4060.0	-0.9	27.88
84	16:00:46.25	-10:08:09.2	315.08	-4.1	1.99	4315.0	0.07	16.32
85	16:01:23.09	-14:28:50.5	317.18	-0.3	1.92	4214.0	-0.23	30.47
86	17:00:54.10	-19:57:31.3	332.38	-1.27	1.56	4211.0	-0.7	32.8
87	19:57:50.11	-33:16:26.0	13.56	2.86	1.32	4319.0	-0.66	23.72
88	19:58:16.32	-32:46:55.6	13.64	2.37	1.8	4499.0	-0.2	25.2
89	19:58:17.09	-33:16:32.5	13.66	2.86	2.07	4177.0	-0.33	15.33
90	19:58:39.50	-32:59:30.1	13.72	2.57	1.84	4362.0	-0.67	17.45
91	19:58:50.18	-33:05:16.1	13.77	2.67	1.39	4225.0	-1.23	16.2
92	19:59:02.09	-33:25:51.6	13.82	3.01	1.95	4646.0	-0.98	52.36
93	19:59:48.53	-33:20:13.6	13.98	2.91	1.67	4008.0	-0.31	23.75

Continued on next page

Table A.1 – *Continued from previous page*

Num	RA_{J2000}	DEC_{J2000}	Λ	B	log(g)	T_{eff}	[m/H]	Rcoeff
94	20:00:08.81	-32:42:50.8	14.03	2.28	1.8	4370.0	-0.68	33.01
95	20:00:34.25	-32:56:00.2	14.12	2.5	1.95	4753.0	-0.63	29.79
96	20:00:48.65	-33:19:37.2	14.19	2.89	2.25	4723.0	-1.03	30.25
97	20:01:06.31	-32:41:03.8	14.23	2.25	1.89	4264.0	-0.6	27.7
98	20:01:08.74	-32:39:25.6	14.24	2.22	1.61	4241.0	-0.45	20.47
99	20:01:12.02	-32:50:30.8	14.25	2.41	2.16	4248.0	0.02	16.54
100	20:01:20.64	-32:36:18.7	14.28	2.17	2.18	4363.0	-0.5	31.93
101	20:01:20.81	-33:20:58.9	14.3	2.91	1.89	4586.0	-0.82	28.07
102	20:02:09.79	-33:13:50.9	14.47	2.79	1.1	4368.0	-1.13	38.56
103	22:00:16.66	-30:08:30.5	39.72	2.29	0.81	4300.0	-1.25	40.51
104	22:00:16.66	-30:08:30.5	39.72	2.29	1.08	4299.0	-1.15	52.7
105	22:00:22.90	-30:07:50.9	39.74	2.28	1.1	4513.0	-1.47	38.94
106	22:00:22.90	-30:07:50.9	39.74	2.28	1.03	4295.0	-1.47	44.52

Table A.1: The selected 106 likely Sagittarius stream members with modified RAVE pipeline metallicity, surface gravity and effective temperature values.

A.2 Spectral lines and reduction

The full wavelength range and reduction for a typical stellar spectrum of a member of the Sagittarius dwarf galaxy, as discussed in Chapter 2.

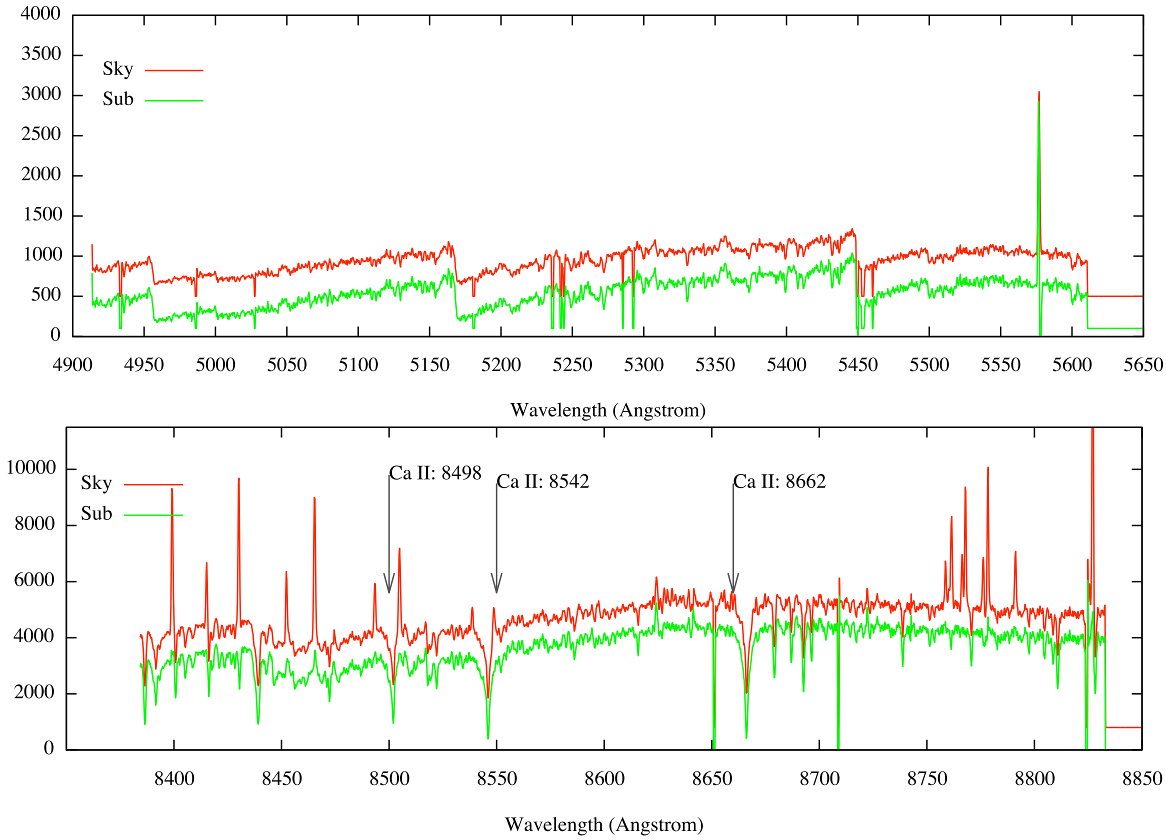

FIGURE A.1: The non-sky-subtracted (red) and the sky-subtracted (green) results from the red (bottom) and blue (top) arms for fibre 395 in pointing F4. Note the count scaling is offset to better display the difference in the two reductions. The titanium oxide bands are present in the blue as well as the expected magnesium and calcium triplets. The calcium triplet we use for our analysis is labeled in the red arm (these are the lines we measure for velocity and metallicity estimates of the star).

A.3 Probability determiniation program source code

Code to produce the probability plots, probabilities, and histograms as discussed in Chapters 4 and 5: **gauss5.py**

```
#!/usr/bin/env python
#gauss5.py
#import
#code runs as: python gauss5.py data1.dat Besanson1.resu Law1.dat 1gprob.dat
#for each region 1--30
#plots produced in code, probability information saved in output 1gprob.dat...30gprob.dat files
#---------------------------------------------------------------
import os, sys
import numpy as np
import matplotlib.pyplot as plt
import asciitable
from scipy import stats
import astropysics
import astropysics.obstools
import astropysics.coords
import math
import pylab as P
import random
from random import randint
from pylab import *
from astropysics.coords import ICRSCoordinates,GalacticCoordinates
from scipy.optimize import curve_fit

#input files for regions 1--30
#---------------------------------------------------------------
f=open(sys.argv[1])
#g1.dat -- g30.dat
y= asciitable.read(f,Reader=asciitable.CommentedHeader,delimiter=' ')
f.close()
#Read in relevant values from data files
#---------------------------------------------------------------
vhc = y['Vhelavg']
vhcgood= (vhc != -99.9) & (vhc >= -400) & (vhc <= 400)
vhcg=vhc[vhcgood]
verr = y['Verravg']
Radeg=y['Radeg']
Decdeg=y['Decdeg']

#Convert to VGSR velocity
#---------------------------------------------------------------
l=[]
b=[]
Radg=Radeg[vhcgood]
Decdg=Decdeg[vhcgood]
for i in xrange(len(Radg)):
    gcoords=ICRSCoordinates(Radg[i],Decdg[i]).convert(GalacticCoordinates)
    l.append(gcoords.l.radians)
    b.append(gcoords.b.radians)

VLSR=vhcg + 9*np.cos(l)*np.cos(b) + 12*np.sin(l)*np.cos(b) + 7*np.sin(b)
VGSR=VLSR + 220*np.sin(l)*np.cos(b)
xb=arange(-400,400,step=8)

#Create a range of velocity and define bins
#---------------------------------------------------------------
```

```
ranged=(VGSR >= -400) & (VGSR <= 400)
numbins = 100
vmin = -400
vmax = 400
binsize = (vmax-vmin)/numbins
VGSRr=VGSR[ranged]
numGiants = float(len(VGSRr))

#Make a sum of gaussians for each velocity point in the data
#---------------------------------------------------------------
prob=[]
for j in range(0,numbins):
    prob.append(0)
for i in xrange(len(VGSRr)):
    sigma = 7.275 # maximum standard deviation between any 2 observations of our data as measured
    mu = VGSRr[i]
    #mu = vhc[i] #For alternative heliocentric velocity scaling
    for j in range(0,numbins):
        prob[j] += (1/(sigma * np.sqrt(2 * np.pi)) * np.exp( - (xb[j] - mu)**2 / (2 * sigma**2) ))
for j in range(0,numbins):
    prob[j]/=len(VGSRr)
#this is the summed gaussian probabilities for data in VGSR

#---------------------------------------------------------------
# Besancon model files corresponding to regions 1--30
f2=open(sys.argv[2])
#Bes_zone01.resu -- Bes_zone30.resu
yb= asciitable.read(f2,Reader=asciitable.CommentedHeader,delimiter=' ')
f2.close()
#Read in relevant values from Besancon files
#---------------------------------------------------------------
vhcb = yb['Vr']
lb=yb['l']*np.pi/180.
bb=yb['b']*np.pi/180.
VLSRb=vhcb + 9*np.cos(lb)*np.cos(bb) + 12*np.sin(lb)*np.cos(bb) + 7*np.sin(bb)
VGSRb=VLSRb + 220*np.sin(lb)*np.cos(bb)
rangeb=(VGSRb >= -400) & (VGSRb <= 400)
verrb = 7.275 #The same sigma as data is used for sampling
probbhi=[]
probblo=[]
rnum=int(len(VGSRb)-1)
iterats=int(1000) #number of iterations for confidence interval
pb=[]
vals=[]

#Draw the Besancon model several times to create a smooth distribution
#---------------------------------------------------------------
xb=arange(-400,400,step=8)
pb=np.zeros(100)
#take random sample of numGiants from Besancon many times VGSRr=numGiants
for k in xrange(iterats):
    for i in xrange(len(VGSRr)):
        sigmab = 7.275           #The same sigma as data is used for sampling
        indexr=randint(0,rnum)#random number
        mu = VGSRb[indexr]
        for j in range(0,numbins):
            pb[j] += (1/(sigmab * np.sqrt(2 * np.pi)) * np.exp( - (xb[j] - mu)**2 / (2 * sigmab**2) ))
    pb=np.array(pb)/len(VGSRr)
#     plot(xb,pb) #to create plots showing the sampling over many iterations
    if k == 0:
        probb=pb
```

```
    else:
        probb=np.vstack((probb,pb))
means=np.mean(probb,axis=0)

#alternative to calculate 2 sigma/ confidence interval
#--------------------------------------------------------------
#argle=int(iterats - (4.6*iterats/100)) #max - 4.6% gives 2 sigma level
argle=int(iterats - (0.4*iterats/100)) #max - 0.4% gives 3 sigma level
blins=[]
sorts=[]
sigs=[]
stdev=[]
for j in range(0,numbins):
    blins=probb[:,j] #make a vector 1 bin long
    blins.sort()
    sorts=sorted(blins)   #sort vector from min to max
    sigs=sorts[argle]     #get element argle of vector
    stdev.append(sigs)    #this is then 2 sigma for each bin
probb2=[]

#Make a sum of gaussians for each velocity point in the Besancon model
#--------------------------------------------------------------
for j in range(0,numbins):
    probb2.append(0)
    probblo.append(0)
    probbhi.append(0)
for i in xrange(len(VGSRb)):
    sigma = 7.275
    mu = VGSRb[i]
    for j in range(0,numbins):
        probb2[j] += (1/(sigma * np.sqrt(2 * np.pi)) * np.exp( - (xb[j] - mu)**2 / (2 * sigma**2) ))
for j in range(0,numbins):
    probb2[j]/=len(VGSRb)
    probbhi[j]=stdev[j]

#Input Law model divided into regions 1--30
#--------------------------------------------------------------
f3=open(sys.argv[3])
yl= asciitable.read(f3,Reader=asciitable.CommentedHeader,delimiter=' ')
f3.close()
#Read in relevant values from Law Model
#--------------------------------------------------------------
vgsrl = yl['vgsr']
ll=yl['l'] #in degrees no need to convert
bl=yl['b']
rangel=(vgsrl >= -400) & (vgsrl <= 400)
verrl = 3.0
probl=[]

#Make a sum of gaussians for each velocity point in the Law model
#--------------------------------------------------------------
for j in range(0,numbins):
    probl.append(0)
for i in xrange(len(vgsrl)):
    sigma = verrl
    mu = vgsrl[i]
    for j in range(0,numbins):
        probl[j] += (1/(sigma * np.sqrt(2 * np.pi)) * np.exp( - (xb[j] - mu)**2 / (2 * sigma**2) ))
for j in range(0,numbins):
    probl[j]/=len(vgsrl)
```

```
# now calc the probability of not halo
#---------------------------------------------------------------
#---------------------------------------------------------------
pNotHalo = []
phalf=[]
for j in range(0,numbins):
    pNotHalo.append(0.0)
    phalf.append(0.0)
for i in range(0,numbins):
    if (prob[i]<=(probb2[i])):
        pNotHalo[i]=0.0
    if (prob[i]>(probb2[i])):
        if (prob[i]<=(stdev[i])):
            pNotHalo[i]=((prob[i]/probb2[i]) - 1)/(stdev[i]/probb2[i])
        if (prob[i]>(stdev[i])):
            pNotHalo[i]=1.0
    phalf[i]=0.05*pNotHalo[i]

#Produce probability and histogram plots
#---------------------------------------------------------------
fig2=plt.figure(1)
ax=fig2.add_subplot(111)
ax.plot(xb,phalf,'c',label='0.05prob')
ax.plot(xb,prob,'r',label='data')
ax.plot(xb,probl,'k',label='law')
ax.plot(xb,probb2,'b',label='bes')
ax.plot(xb,(probbhi),'--b')
#ax.plot(xb,(probblo),'--b')
ax.set_xlabel('VGSR (km/s)')
plt.title('SGR Field %s Num= %d' %(sys.argv[1],numGiants))
ax.legend(loc='upper left',numpoints=1)
plt.show()

n, bins, patches = plt.hist(VGSRr[ranged],50,normed=1, histtype='stepfilled',label=['data'])
P.setp(patches, 'facecolor', 'r', 'alpha', 0.75)
n, bins, patches = plt.hist(VGSRb[rangeb],50,normed=1, histtype='stepfilled',label=['bes'])
P.setp(patches, 'facecolor', 'b', 'alpha', 0.75)
n, bins, patches = plt.hist(vgsrl[rangel],50,normed=1, histtype='stepfilled',label=['law'])
P.setp(patches, 'facecolor', 'g', 'alpha', 0.75)
P.legend()
plt.xlabel('VGSR (km/s)')
plt.title('SGR Field %s' %(sys.argv[1]))
plt.show()

#Print input file plus probability information and save
#---------------------------------------------------------------
f4=open(sys.argv[4],'w')
gg=y[vhcgood]
for i in xrange(len(VGSRr)):
    index = int((VGSRr[i]-vmin)/binsize)
    f4.write("   ".join([str(k) for k in list(gg[i])])+"  "+str(pNotHalo[index])+'\n')
f4.close()
```

List of Symbols

The following list includes the most prominent symbols and abbreviations used in this work. It is neither exhaustive nor exclusive.

$2dfdr$ **Data reduction program of the AAO (Heald 2007)**

$2MASS$ **Two Micron All Sky Survey catalog (Skrutskie et al. 2006)**

Å **Angstroms**

$[\alpha/\mathrm{Fe}]$ **Alpha abundance from RAVE**

AAT **Anglo-Australian Telescope**

AAO **Australian Astronomical Observatory**

$AAOmega$ **Multi-object spectrograph on the AAT (Sharp et al. 2006; Spolaor 2010)**

AGB **Asymptotic giant branch**

$A_v,\ A_J,\ A_H,\ A_K$ **Extinction corrected** V, J, H, K **(Equations 2.3, 2.4, and 2.5)**

$c_{o,1,2,3}$ **Coefficients for calibration of** $[\mathrm{M/H}]$ **(Equation 2.17 and 2.18)**

$\mathrm{C_{bes}}$ **The confidence level cut-off for the Besançon Galaxy model (Robin et al. 2003)**

CDM **Cold dark matter**

$CFHT$ **Canada France Hawaii Telescope**

CMB **Cosmic microwave background**

ΛCDM **Λ (vacuum energy) cold dark matter formulation, a description of the Big Bang model**

CMD **Colour-magnitude diagram**

$Core1$**:** $F1, F2, F4, F5, F6, F8$ **The first six Core 1 pointings (Chapters 2 and 3)**

$\mathrm{D_{pop}}$ **Generalised gaussian histograms (from Equation 4.1)**

$\mathrm{D_{reg}}, \mathrm{D_B}$ **Calculated** $\mathrm{D_{pop}}$ **for Sgr stream regions, and for the Milky Way halo from the Besançon Galaxy model (Robin et al. 2003)**

$E(B-V)$ **Reddening**

EMP **Extremely metal poor**

[Fe/H] **Metallicity**

Gyr **Gigayears, y $\times$ 10^9**

$(H-K)_{bb}, (J-H)_{bb}, K_{bb}$ **Bessel-Brett colours (Equations 2.6, 2.7, and 2.6)**

$IRAF$ **Data reduction software package distributed by the National Optical Astronomy Observatories**

$J,\ H,\ K$ **Magnitude colours from 2MASS**

K_{bbe} **Extinction corrected Bessel Brett K magnitude**

$K-S\ test$ **Kolmogorov-Smirnov test (Massey 1951)**

$l,\ b$ **Galactocentric coordinate system**

log(g) **Log of the surface gravity from RAVE**

λ **Wavelength in Å**

Λ, B **Sgr coordinate system (Majewski et al. 2003)**

$M54$ **Globular cluster Messier 54 (also known as NGC 6715)**

MDF **Metallicity distribution function**

$(m - M)$ **Distance modulus (Equation 2.10)**

[m/H] **RAVE metallicity (Siebert et al. 2011; Zwitter et al. 2008; Steinmetz et al. 2006)**

[M/H] **Calibrated RAVE metallicity (Equation 2.16)**

M_k **Absolute K magnitude**

σ **Standard deviation**

Sgr **The Sagittarius dwarf galaxy**

$Pal5$ **Palomar 5 globular cluster (Harris 1996)**

$\mathrm{P}_{\mathrm{NotHalo}}$ **Probability of a star not being part of the Milky Way halo (Equation 4.2)**

$P1$ **Populations with** $\mathbf{P}_{\mathbf{NotHalo}} = 1$

RA, DEC **J2000 right ascension and declination coordinates**

$R01$ **Broader core region including 23 pointings around the centre of the Sgr dwarf (Core 1 plus all follow-up observations, see Chapter 3 and 4)**

$RAVE$ **Radial Velocity Experiment pipeline (Siebert et al. 2011; Zwitter et al. 2008; Steinmetz et al. 2006)**

$\mathrm{R_{coeff}}$ **RAVE correlation coefficient**

RGB **Red giant branch**

$Sgr\ stream : R01 - R30$ **Covering the full set of Sgr observations for this thesis, includes 15,000 additional spectra outside of R01**

$SDSS$ **The Sloan Digital Sky Survey (York et al. 2000)**

$\mathrm{T_{eff}}$ **The effective temperature from RAVE**

$TRGB$ **Tip of the red giant branch**

V **Visual magnitude (from 2MASS, Equation 2.1)**

$V_h,\ V_{GSR}$ **heliocentric and Galactocentric velocities**

VOD **The Virgo overdensity (Keller 2010)**

References

Armandroff, T. E., & Da Costa, G. S. 1991, AJ, 101, 1329

Armandroff, T. E., & Zinn, R. 1988, AJ, 96, 92

Barden, S. C., Jones, D. J., Barnes, S. I., et al. 2010, in Society of Photo-Optical Instrumentation Engineers (SPIE) Conference Series, Vol. 7735, Society of Photo-Optical Instrumentation Engineers (SPIE) Conference Series

Battaglia, G., Irwin, M., Tolstoy, E., et al. 2008, MNRAS, 383, 183

Beers, T. C., Rossi, S., Norris, J. E., Ryan, S. G., & Shefler, T. 1999, AJ, 117, 981

Bellazzini, M., Correnti, M., Ferraro, F. R., Monaco, L., & Montegriffo, P. 2006a, A&A, 446, L1

Bellazzini, M., Ferraro, F. R., & Buonanno, R. 1999a, MNRAS, 304, 633

—. 1999b, MNRAS, 307, 619

Bellazzini, M., Ferraro, F. R., & Buonanno, R. 1999c, in IAU Symposium, Vol. 192, The Stellar Content of Local Group Galaxies, ed. P. Whitelock & R. Cannon, 121

Bellazzini, M., Newberg, H. J., Correnti, M., Ferraro, F. R., & Monaco, L. 2006b, A&A, 457, L21

Bellazzini, M., Ibata, R. A., Chapman, S. C., et al. 2008, AJ, 136, 1147

Belokurov, V. 2013, ArXiv e-prints

Belokurov, V., Evans, N. W., Irwin, M. J., Hewett, P. C., & Wilkinson, M. I. 2006a, ApJ, 637, L29

Belokurov, V., Zucker, D. B., Evans, N. W., et al. 2006b, ApJ, 642, L137

Belokurov, V., Evans, N. W., Irwin, M. J., et al. 2007a, ApJ, 658, 337

Belokurov, V., Zucker, D. B., Evans, N. W., et al. 2007b, ApJ, 654, 897

Bessell, M. S., & Brett, J. M. 1988, PASP, 100, 1134

Bica, E., & Alloin, D. 1987, A&A, 186, 49

Blaña, M., Fellhauer, M., & Smith, R. 2012, A&A, 542, A61

Bonifacio, P., Hill, V., Molaro, P., et al. 2000, A&A, 359, 663

Bonifacio, P., Sbordone, L., Marconi, G., Pasquini, L., & Hill, V. 2004, A&A, 414, 503

Braun, R., & Burton, W. B. 1999, A&A, 341, 437

Cacciari, C., Bellazzini, M., & Colucci, S. 2002, in IAU Symposium, Vol. 207, Extragalactic Star Clusters, ed. D. P. Geisler, E. K. Grebel, & D. Minniti, 168

Cardelli, J. A., Clayton, G. C., & Mathis, J. S. 1989, ApJ, 345, 245

Carlberg, R. G. 2009, ApJ, 705, L223

Carlin, J. L. 2012, in Astronomical Society of the Pacific Conference Series, Vol. 458, Galactic Archaeology: Near-Field Cosmology and the Formation of the Milky Way, ed. W. Aoki, M. Ishigaki, T. Suda, T. Tsujimoto, & N. Arimoto, 207

Carlin, J. L., Majewski, S. R., Casetti-Dinescu, D. I., et al. 2012, ApJ, 744, 25

Carrera, R., Gallart, C., Pancino, E., & Zinn, R. 2007, AJ, 134, 1298

Carretta, E., Bragaglia, A., Gratton, R. G., et al. 2010, A&A, 520, A95

Casey, A. R., Da Costa, G., Keller, S. C., & Maunder, E. 2013, ApJ, 764, 39

Casey, A. R., Keller, S. C., & Da Costa, G. 2012a, AJ, 143, 88

Casey, A. R., Keller, S. C., Ness, M. K., Aegis Collaboration, & Skymapper Team. 2012b, in Astronomical Society of the Pacific Conference Series, Vol. 458, Galactic Archaeology: Near-Field Cosmology and the Formation of the Milky Way, ed. W. Aoki, M. Ishigaki, T. Suda, T. Tsujimoto, & N. Arimoto, 413

Chou, M.-Y., Majewski, S. R., Cunha, K., et al. 2007, ApJ, 670, 346

Cole, A. A. 2001, ApJ, 559, L17

Cole, A. A., Smecker-Hane, T. A., & Gallagher, III, J. S. 2000, AJ, 120, 1808

Da Costa, G. S., Hatzidimitriou, D., Irwin, M. J., & McMahon, R. G. 1991, MNRAS, 249, 473

Dalcanton, J. J., & Hogan, C. J. 2001, ApJ, 561, 35

de Jong, J. T. A., Martin, N. F., Rix, H.-W., et al. 2010, ApJ, 710, 1664

Diaz, A. I., Terlevich, E., & Terlevich, R. 1989, MNRAS, 239, 325

Dinescu, D. I., Girard, T. M., van Altena, W. F., & López, C. E. 2005, ApJ, 618, L25

Dotter, A., Chaboyer, B., Jevremović, D., et al. 2008, ApJS, 178, 89

Drake, A. J., Catelan, M., Djorgovski, S. G., et al. 2012, ArXiv e-prints

Fahlman, G. G., Mandushev, G., Richer, H. B., Thompson, I. B., & Sivaramakrishnan, A. 1996, ApJ, 459, L65

Fellhauer, M., Belokurov, V., Evans, N. W., et al. 2006, ApJ, 651, 167

Ferguson, A. M. N., Johnson, R. A., Faria, D. C., et al. 2005, ApJ, 622, L109

Fillmore, J. A., & Goldreich, P. 1984, ApJ, 281, 1

Frebel, A., Lunnan, R., Casey, A. R., et al. 2013, ApJ, 771, 39

Freeman, K., & Bland-Hawthorn, J. 2002, ARA&A, 40, 487

Friel, E. D., & Janes, K. A. 1993, A&A, 267, 75

Frinchaboy, P. M., Majewski, S. R., Muñoz, R. R., et al. 2012, ApJ, 756, 74

Geha, M., Willman, B., Simon, J. D., et al. 2009, ApJ, 692, 1464

Gilmore, G., Koposov, S., Norris, J. E., et al. 2013, The Messenger, 151, 25

Gott, III, J. R. 1975, ApJ, 201, 296

Grillmair, C. J., & Dionatos, O. 2006, ApJ, 643, L17

Gunn, J. E. 1977, ApJ, 218, 592

Gunn, J. E., & Gott, III, J. R. 1972, ApJ, 176, 1

Harbeck, D., Grebel, E. K., Holtzman, J., et al. 2001, AJ, 122, 3092

Harris, W. E. 1996, AJ, 112, 1487

Heald, R. 2007, AAO 2dfdr Cookbook, www2.aao.gov.au/twiki/bin/view/Main/CookBook2dfdr

Helmi, A., Irwin, M. J., Tolstoy, E., et al. 2006, ApJ, 651, L121

Hernquist, L. 1990, ApJ, 356, 359

Hoffman, Y., & Shaham, J. 1985, ApJ, 297, 16

Hyde, E. A., Zucker, D. B., Irwin, M., Peñarrubia, J., & Koch, A. 2012, in Astronomical Society of the Pacific Conference Series, Vol. 458, Galactic Archaeology: Near-Field Cosmology and the Formation of the Milky Way, ed. W. Aoki, M. Ishigaki, T. Suda, T. Tsujimoto, & N. Arimoto, 325

Hyde, E. A., Zucker, D. B., Penarrubia, J., et al. 2011, in Bulletin of the American Astronomical Society, Vol. 43, American Astronomical Society Meeting Abstracts #217, 152.28

Hyde, E. A., Zucker, D. B., Keller, S., et al. 2013, in American Astronomical Society Meeting Abstracts, Vol. 221, American Astronomical Society Meeting Abstracts, 425.03

Ibata, R., Lewis, G. F., Irwin, M., Totten, E., & Quinn, T. 2001, ApJ, 551, 294

Ibata, R., Martin, N. F., Irwin, M., et al. 2007, ApJ, 671, 1591

Ibata, R. A., Gilmore, G., & Irwin, M. J. 1994, Nature, 370, 194

—. 1995, MNRAS, 277, 781

Ibata, R. A., Lewis, G. F., Irwin, M. J., & Cambrésy, L. 2002a, MNRAS, 332, 921

Ibata, R. A., Lewis, G. F., Irwin, M. J., & Quinn, T. 2002b, MNRAS, 332, 915

Ibata, R. A., Wyse, R. F. G., Gilmore, G., Irwin, M. J., & Suntzeff, N. B. 1997, AJ, 113, 634

Irwin, M., & Hatzidimitriou, D. 1995, MNRAS, 277, 1354

Irwin, M. J., Bunclark, P. S., Bridgeland, M. T., & McMahon, R. G. 1990, MNRAS, 244, 16P

Jin, S., Martin, N., de Jong, J., et al. 2012, in Astronomical Society of the Pacific Conference Series, Vol. 458, Galactic Archaeology: Near-Field Cosmology and the Formation of the Milky Way, ed. W. Aoki, M. Ishigaki, T. Suda, T. Tsujimoto, & N. Arimoto, 153

Johnston, K. V., Law, D. R., & Majewski, S. R. 2005, ApJ, 619, 800

Jones, J. E., Alloin, D. M., & Jones, B. J. T. 1984, ApJ, 283, 457

Jorgensen, U. G., Carlsson, M., & Johnson, H. R. 1992, A&A, 254, 258

Jurić, M., Ivezić, Ž., Brooks, A., et al. 2008, ApJ, 673, 864

Keller, S. C. 2010, PASA, 27, 45

Keller, S. C., Yong, D., & Da Costa, G. S. 2010, ApJ, 720, 940

Kerr, F. J., & Lynden-Bell, D. 1986, MNRAS, 221, 1023

King, I. 1962, AJ, 67, 471

King, I. R. 1966, AJ, 71, 64

Kirby, E. N., Guhathakurta, P., & Sneden, C. 2008a, ApJ, 682, 1217

Kirby, E. N., Simon, J. D., Geha, M., Guhathakurta, P., & Frebel, A. 2008b, ApJ, 685, L43

Klypin, A., Kravtsov, A. V., Valenzuela, O., & Prada, F. 1999, ApJ, 522, 82

Klypin, A., Zhao, H., & Somerville, R. S. 2002, ApJ, 573, 597

Koch, A., Grebel, E. K., Gilmore, G. F., et al. 2008a, AJ, 135, 1580

Koch, A., Grebel, E. K., Wyse, R. F. G., et al. 2006, AJ, 131, 895

Koch, A., & McWilliam, A. 2010, AJ, 139, 2289

Koch, A., Rich, R. M., Reitzel, D. B., et al. 2008b, ApJ, 689, 958

Koposov, S. E., Belokurov, V., Evans, N. W., et al. 2012, ApJ, 750, 80

Kravtsov, A. 2010, Advances in Astronomy, 2010

Law, D. 2012, Tidal Debris of the Sagittarius Dwarf Spheroidal, http://www.astro.virginia.edu/~srm4n/Sgr/

Law, D. R., Johnston, K. V., & Majewski, S. R. 2005, ApJ, 619, 807

Law, D. R., & Majewski, S. R. 2010, ApJ, 714, 229

Layden, A. C., & Sarajedini, A. 1997, ApJ, 486, L107

—. 2000, AJ, 119, 1760

Majewski, S. R., Skrutskie, M. F., Weinberg, M. D., & Ostheimer, J. C. 2003, ApJ, 599, 1082

Majewski, S. R., Kunkel, W. E., Law, D. R., et al. 2004, AJ, 128, 245

Marigo, P., Girardi, L., Bressan, A., et al. 2008, A&A, 482, 883

Martin, N. F., Ibata, R. A., Bellazzini, M., et al. 2004, MNRAS, 348, 12

Martin, N. F., Ibata, R. A., Rich, R. M., et al. 2014, ApJ, 787, 19

Martínez-Delgado, D., Aparicio, A., Gómez-Flechoso, M. Á., & Carrera, R. 2001, ApJ, 549, L199

Martínez-Delgado, D., Gómez-Flechoso, M. Á., Aparicio, A., & Carrera, R. 2004, ApJ, 601, 242

Massey, F. J. 1951, Journal of the American Statistical Association, 46, 68

Mateo, M., Mirabal, N., Udalski, A., et al. 1996, ApJ, 458, L13

Mateo, M., Udalski, A., Szymanski, M., et al. 1995, AJ, 109, 588

Mateo, M. L. 1998, ARA&A, 36, 435

McConnachie, A. W. 2012, AJ, 144, 4

McConnachie, A. W., Irwin, M. J., Ferguson, A. M. N., et al. 2005, MNRAS, 356, 979

McDonald, I., Zijlstra, A. A., Sloan, G. C., et al. 2013, MNRAS, 436, 413

Mellinger, A. 2009, PASP, 121, 1180

Mihalas, D., & Binney, J. 1981, Science, 214, 829

Miyamoto, M., & Nagai, R. 1975, PASJ, 27, 533

Monaco, L., Bellazzini, M., Bonifacio, P., et al. 2007, A&A, 464, 201

—. 2005, A&A, 441, 141

Monaco, L., Bellazzini, M., Ferraro, F. R., & Pancino, E. 2003, ApJ, 597, L25

—. 2004, MNRAS, 353, 874

Moore, B., Diemand, J., Madau, P., Zemp, M., & Stadel, J. 2006, MNRAS, 368, 563

Moore, B., Ghigna, S., Governato, F., et al. 1999, ApJ, 524, L19

Murphy, S., Keller, S., Schmidt, B., et al. 2009, in Astronomical Society of the Pacific Conference Series, Vol. 404, Astronomical Society of the Pacific Conference Series, ed. B. Soonthornthum, S. Komonjinda, K. S. Cheng, & K. C. Leung, 356–+

Navarro, J. F., & Benz, W. 1991, ApJ, 380, 320

Navarro, J. F., Frenk, C. S., & White, S. D. M. 1995, MNRAS, 275, 56

—. 1996, ApJ, 462, 563

—. 1997, ApJ, 490, 493

Navarro, J. F., & White, S. D. M. 1994, MNRAS, 267, 401

Newberg, H. J., Willett, B. A., Yanny, B., & Xu, Y. 2010, ApJ, 711, 32

Newberg, H. J., Yanny, B., Cole, N., et al. 2007, ApJ, 668, 221

Newberg, H. J., Yanny, B., & Willett, B. A. 2009, ApJ, 700, L61

Newberg, H. J., Yanny, B., Rockosi, C., et al. 2002, ApJ, 569, 245

Niederste-Ostholt, M., Belokurov, V., Evans, N. W., et al. 2009, MNRAS, 398, 1771

Niederste-Ostholt, M., Belokurov, V., Evans, N. W., & Peñarrubia, J. 2010, ApJ, 712, 516

Norris, J. E., Gilmore, G., Wyse, R. F. G., et al. 2008, ApJ, 689, L113

Norris, J. E., Wyse, R. F. G., Gilmore, G., et al. 2010a, ArXiv e-prints

—. 2010b, ApJ, 723, 1632

Odenkirchen, M., Grebel, E. K., Dehnen, W., Rix, H.-W., & Cudworth, K. M. 2002, AJ, 124, 1497

Odenkirchen, M., Grebel, E. K., Rockosi, C. M., et al. 2001, ApJ, 548, L165

Odenkirchen, M., Grebel, E. K., Dehnen, W., et al. 2003, AJ, 126, 2385

Olszewski, E. W., Schommer, R. A., Suntzeff, N. B., & Harris, H. C. 1991, AJ, 101, 515

Paturel, G., Andernach, H., Bottinelli, L., et al. 1997, A&AS, 124, 109

Peñarrubia, J., Belokurov, V., Evans, N. W., et al. 2010, MNRAS, 408, L26

Peñarrubia, J., McConnachie, A. W., & Navarro, J. F. 2008, ApJ, 672, 904

Peñarrubia, J., Martínez-Delgado, D., Rix, H. W., et al. 2005, ApJ, 626, 128

Peñarrubia, J., Zucker, D. B., Irwin, M. J., et al. 2011, ApJ, 727, L2

Pont, F., Zinn, R., Gallart, C., Hardy, E., & Winnick, R. 2004, AJ, 127, 840

Robin, A. C., Reylé, C., Derrière, S., & Picaud, S. 2003, A&A, 409, 523

Roeser, S., Demleitner, M., & Schilbach, E. 2010, AJ, 139, 2440

Rutledge, G. A., Hesser, J. E., & Stetson, P. B. 1997a, PASP, 109, 907

Rutledge, G. A., Hesser, J. E., Stetson, P. B., et al. 1997b, PASP, 109, 883

Sales, L. V., Helmi, A., Starkenburg, E., et al. 2008, MNRAS, 389, 1391

Sarajedini, A., & Layden, A. C. 1995, AJ, 109, 1086

Sbordone, L., Bonifacio, P., Buonanno, R., et al. 2007, A&A, 465, 815

Schlegel, D. J., Finkbeiner, D. P., & Davis, M. 1998, ApJ, 500, 525

Searle, L., & Zinn, R. 1978, ApJ, 225, 357

Sharp, R., Saunders, W., Smith, G., et al. 2006, in Society of Photo-Optical Instrumentation Engineers (SPIE) Conference Series, Vol. 6269, Society of Photo-Optical Instrumentation Engineers (SPIE) Conference Series

Siebert, A., Williams, M. E. K., Siviero, A., et al. 2011, AJ, 141, 187

Siegel, M. H., Dotter, A., Majewski, S. R., et al. 2007, ApJ, 667, L57

Simon, J. D., Frebel, A., McWilliam, A., Kirby, E. N., & Thompson, I. B. 2010, ApJ, 716, 446

Simon, J. D., Geha, M., Minor, Q. E., et al. 2011, ApJ, 733, 46

Skrutskie, M. F., Cutri, R. M., Stiening, R., et al. 2006, AJ, 131, 1163

Slater, C. T., Bell, E. F., Schlafly, E. F., et al. 2012, ArXiv e-prints

Spolaor, M. 2010, AAOmega Instrument, `http://www.aao.gov.au/AAO/2df/aaomega/aaomega.html`

Starkenburg, E., Hill, V., Tolstoy, E., et al. 2010, A&A, 513, A34

Starkenburg, E., Hill, V., Tolstoy, E., et al. 2011, in EAS Publications Series, Vol. 48, EAS Publications Series, ed. M. Koleva, P. Prugniel, & I. Vauglin, 13–18

—. 2013, A&A, 549, A88

Steinmetz, M., Zwitter, T., Siebert, A., et al. 2006, AJ, 132, 1645

Suntzeff, N. B., Mateo, M., Terndrup, D. M., et al. 1993, ApJ, 418, 208

Suntzeff, N. B., Schommer, R. A., Olszewski, E. W., & Walker, A. R. 1992, AJ, 104, 1743

Tafelmeyer, M., Jablonka, P., Hill, V., et al. 2010, A&A, 524, A58

Tonry, J., & Davis, M. 1979, AJ, 84, 1511

Ural, U., Wilkinson, M. I., Koch, A., et al. 2010, MNRAS, 402, 1357

Valenti, E., Ferraro, F. R., & Origlia, L. 2004, MNRAS, 354, 815

Walker, M. G., Mateo, M., Olszewski, E. W., et al. 2009, ApJ, 704, 1274

Walker, M. G., McGaugh, S. S., Mateo, M., Olszewski, E. W., & Kuzio de Naray, R. 2010, ApJ, 717, L87

Westfall, K. B., Majewski, S. R., Ostheimer, J. C., et al. 2006, AJ, 131, 375

Whitelock, P. A., Irwin, M., & Catchpole, R. M. 1996, NEWA, 1, 57

Williams, L. L. R., Babul, A., & Dalcanton, J. J. 2004, ApJ, 604, 18

Yanny, B., Newberg, H. J., Johnson, J. A., et al. 2009, ApJ, 700, 1282

Yoon, J. H., Johnston, K. V., & Hogg, D. W. 2011, ApJ, 731, 58

York, D. G., Adelman, J., Anderson, Jr., J. E., et al. 2000, AJ, 120, 1579

Zwitter, T., Siebert, A., Munari, U., et al. 2008, AJ, 136, 421